D I S S E R T A T I O N

submitted to the
Combined Faculties for the Natural Sciences and for Mathematics
of the Ruperto-Carola University of Heidelberg, Germany
for the degree of
Doctor of Natural Sciences

presented by
Diplom-Chemiker Lars Kastrup
born in Hannover

Oral examination: October 22, 2004

Erklärung gemäß § 7(3) b) und c) der Promotionsordnung:

a) Ich erkläre hiermit, dass ich die vorgelegte Dissertation selbst verfasst und mich dabei keiner anderen als der von mir ausdrücklich bezeichneten Quellen bedient habe.

b) Ich erkläre hiermit, dass ich an keiner anderen Stelle ein Prüfungsverfahren beantragt bzw. die Dissertation in dieser oder anderer Form bereits anderweitig als Prüfungsarbeit verwendet oder einer anderen Fakultät als Dissertation vorgelegt habe.

_____

(Lars Kastrup)

Fluorescence Depletion by Stimulated Emission in Single-Molecule Spectroscopy

Referees:

Prof. Dr. Jürgen Wolfrum

Prof. Dr. Stefan W. Hell

Abstract

This thesis presents the first application of the stimulated emission depletion (STED) technique to the field of single-molecule fluorescence spectroscopy. It is demonstrated that fluorescence quenching induced by STED is reversible and can be repeated a large number of cycles on a single molecule. Being ideal point-like probes, single molecules can therefore be used to characterize the resolution of STED microscopes.

In a spectroscopic study, two simplifed models of the photophysical processes involved in STED are analyzed and applied to the experimental determination of the stimulated emission cross sections on a single-molecule level.

In addition, the STED concept as applied in subdiffraction-resolution microscopy is transferred to fluorescence fluctuation spectroscopy. A successful implementation promises to expand the possibilities particularly of fluorescence correlation spectroscopy (FCS) which is already the most widely used fluctuation technique today but is restricted to concentrations on the nanomolar scale. Reducing the detection volume beyond the diffraction limit could render the micromolar range accessible and could thus open up new applications in the life sciences.

Zusammenfassung

Diese Arbeit stellt die erste Anwendung der Fluoreszenzlöschung durch stimulierte Emission (*stimulated emission depletion*, STED) auf das Gebiet der Einzelmolekül-Fluoreszenzspektroskopie dar. Es wird gezeigt, dass STED an einem einzelnen Molekül reversibel ist und eine Vielzahl von Zyklen wiederholt werden kann. Als ideale punktförmige Strahler können einzelne Moleküle daher eingesetzt werden, um das Auflösungsvermögen von STED-Mikroskopen zu charakterisieren.

In einer spektroskopischen Studie werden zwei vereinfachte Modelle der an STED beteiligten photophysikalischen Prozesse analysiert and zur experimentellen Bestimmung der Wirkungsquerschnitte für stimulierte Emission auf Einzelmolekülbasis herangezogen.

Außerdem wird das STED-Konzept aus der optischen Mikroskopie zur Durchbrechung der Beugungsrenze auf die Fluoreszenzfluktuationsspektroskopie übertragen. Eine erfolgreiche Umsetzung verspricht vor allem, die Möglichkeiten der Fluoreszenzkorrelationsspektroskopie (FCS) zu erweitern, die bereits heute die meistgenutzte Fluktuationsmethode darstellt, jedoch bislang auf nanomolare Konzentrationen beschränkt ist. Die Verkleinerung des Detektionsvolumens auf Größen unterhalb der optischen Beugungsgrenze könnte den mikromolaren Konzentrationsbereich und damit neue Anwendungen im Bereich der *Life Sciences* erschließen.

List of Publications

Parts of this work have been/ will be pusblished as the following journal contributions:

1. L. Kastrup, H. Blom, C. Eggeling, S. W. Hell. Fluorescence Correlation Spectroscopy in Focal Volumes Reduced by Stimulated Emission Depletion. In preparation.

2. L. Kastrup, S. W. Hell. Stimulated Emission Depletion Efficiency as a Single-Molecule Criterion. In preparation.

3. L. Kastrup, S. W. Hell. Absolute Optical Cross Sections of Individual Fluorescent Molecules. Submitted to *Angew. Chem. Intl. Ed.*

4. S. W. Hell, S. Jakobs, L. Kastrup. Imaging and writing at the nanoscale with focused visible light through saturable optical transitions. *Appl. Phys. A* **77**, 859–860 (2003).

5. V. Westphal, C. M. Blanca, M. Dyba, L. Kastrup, S. W. Hell. Laser-diode-stimulated emission depletion microscopy. *Appl. Phys. Lett.* **82** (18), 3125–3127 (2003).

6. V. Westphal, L. Kastrup, S. W. Hell. Lateral resolution of 28 nm (λ/25) in far-field fluorescence microscopy. *Appl. Phys. B* **77** (4), 377–380 (2003).

Contents

Abbreviations

1D, 2D, 3D	One-/Two-/Three-Dimensional
AFM	Atomic Force Microscopy
AOI	Angle of Incidence
APD	Avalanche Photodiode
BP	Bandpass (Filter)
cw	Continuous Wave
DC	Dichroic Beamsplitter
det	Detection
DFT	Density Functional Theory
eff	Effective
exc	Excitation
FCS	Fluorescence Correlation Spectroscopy
FFS	Fluorescence Fluctuation Spectroscopy
FIDA	Fluorescence Intensity Distribution Analysis
FIFO	First In, First Out
FILDA	Fluorescence Intensity and Lifetime Distribution Analysis
FIMDA	Fluorescence Intensity Multiple Distribution Analysis
fl	Fluorescence
FWHM	Full-Width at Half-Maximum
GFP	Green Fluorescent Protein
GVD	Group Velocity Dispersion
HTS	High-Throughput Screening
IC	Internal Conversion
ISC	Inter-System Crossing
IVR	Intramolecular Vibrational Redistribution
KTP	Potassium Titanyl Phosphate ($KTiOPO_4$)
LCAO	Linear Combination of Atomic Orbitals
LPC	Laser Power Controller
MCP	Multichannel Plate
NA	Numerical Aperture

NSOM	Nearfield Scanning Optical Microscopy
ODE	Ordinary Differential Equation
OPO	Optical Parametric Oscillator
OTF	Optical Transfer Function
PBS	Polarizing Beamsplitter
PCH	Photon Counting Histogram (Analysis)
PSF	Point-Spread Function
PVA	Poly(vinyl alcohol)
RET	Resonance Energy Transfer
RPM	Revolutions per Minute
RTP	Rubidium Titanyl Phosphate ($RbTiOPO_4$)
S/N	Signal-to-Noise
SEP	Stimulated Emission Pumping
SERS	Surface-Enhanced Raman Scattering
SHG	Second Harmonic Generation
SLM	Spatial Light Modulator
SMD	Single-Molecule Detection
SNOM	Scanning Near-Field Optical Microscopy
STED	Stimulated Emission Depletion
TCSPC	Time-Correlated Single-Photon Counting
Ti:Sa	Titanium-Sapphire Laser (modelocked)
TIR / TIRF	Total Internal Reflection (Fluorescence)

"Je me suis demandé si quelque phénomène permettrait de rendre visibles, sinon les molécules individuellement, du moins les fluctuations de concentration qui doivent exister à chaque instant, par suite de l'agitation moléculaire, au sein d'une solution étendue."[1]

M. Jean Perrin, *La Fluorescence* (1918).

[1] "I was wondering if it was possible to visualize if not individual molecules but at least the continuous concentration fluctuations in a bulk solution which occur upon molecular excitation."

Chapter 1

Introduction

1.1 Single-Molecule Fluorescence Spectroscopy: History and Motivation

Almost a century ago, in a fundamental article on fluorescence [1], *Jean Perrin* already speculated on whether the observation of individual molecules would eventually become feasible. However, it took more than half a century until, in 1976, *Hirschfeld* published the first successful detection of single γ-globulin molecules [2] which still required heavy labeling with up to 100 markers per molecule. Interestingly, the first observation of a truly single molecule succeeded in absorption rather than in fluorescence mode [3] despite its substantially lower sensitivity. Not surprisingly, though, single fluorescent emitters were detected soon thereafter [4]. The main driving force for the development of these ultimately sensitive detection schemes was an application which was anticipated to have a strong impact on molecular biology: the rapid sequencing of DNA [5, 6]. The idea was to subsequently cleave the individually labeled nucleotides off a fixed DNA strand and to detect the nucleotides one after another in a microfluidic channel. With this goal in mind, the quasi-natural experimental setup employed was a flow-cell instead of a confocal arrangement which entailed major background contributions in the signals. Despite attempts to overcome these complications by e.g. gated fluorescence detection or lock-in technqiues the background issue has remained the major reason which is why this approach to DNA sequencing has still not experienced a major breakthrough. Nevertheless, a lot of know-how has been gained along the way and, in fact, single-molecule fluorescence detection has meanwhile become a rather mature technique.

The main motivation that renders single-molecule experiments appealing is the fact that all kinds of ensemble averaging are eliminated. As a result, individual properties of each molecule can be examined that are otherwise hidden in a large population. These include static inhomogeneities which may be due to variations in the molecule's local

environment or its conformation which is particularly important in the case of macromolecules like proteins. While it is possible to determine individual molecular properties, single molecules can on the other hand be used as nearly point-like reporters of their nanoenvironment. Likewise, temporal fluctuations can be studied devoid of ensemble averaging which, in fact, has lead to a number of effects to be observed which were impossible to study before. In this respect, single-molecule detection has opened up a qualitatively new field of research.

As was recognized early on, the successful observation of single molecules primarily required efficient background suppression strategies and, secondly, necessitated highly sensitive detection schemes. The main approach was to reduce the detection volumes as far as possible by using confocal microsopy, scannning near-field optical microscopy (SNOM) or total internal reflection illumination (TIR). Thus, on the one hand, the rapid development of single-molecule techniques owns its success to a better part to the widespread availability of confocal and optical near-field microscopes and, on the other hand, an increasing number of spectroscopic features is integrated into commercially available microscopes today. Further advances in the photonics technology have stimulated the progress of single-molecule fluorescence techniqes. In particular, with the availability of high-performance optical filters, the background contributions due to Rayleigh and Raman scattering can now be efficiently suppressed. Highly sensitive avalanche photodiodes with quantum efficiencies reaching 80% have displaced photomultipliers and have quadrupled the detection efficiency. And with the advent of highly sensitive CCD cameras, even the widefield imaging of single fluorophores has become feasible as was impressively demonstrated by *Noji* et al. who imaged the rotation of the γ-subunit of the F_1 ATPase in a widefield setup in almost real-time [7, 8].

Having only a single or, at most, a few molecules present in the detection volume at a time, the *fluctuations* of the fluorescence emission can be observed which are otherwise hidden in a large ensemble, but which carry valuable information on the photophysical dynamics of the fluorophore. Fluorescence correlation spectroscopy (FCS) as the first concept to analyze these fluctuations dates back to the early 1970s [9] but has found widespread application [10, 11, 12] only after the technological advances described above. FCS provides a way to analyze photophysical processes and diffusion behavior of fluorescent molecules in solution. More recently, the correlation approach pursued in FCS has been complemented with techniques based on the analysis of the photon counting histogram (fluorescence intensity distribution analysis, FIDA [13] and photon counting histogram analysis, PCH [14]). Because the instrumentation in these methods is relatively easy to handle, data analysis can be largely automated and the measurement times are short, fluorescence fluctuation methods are now routinely employed for high-throughput screening (HTS) [15, 16, 17, 18, 19].

From the spectroscopic viewpoint, the relatively simple setups employed in the early

work have evolved into complex experiments as more and more spectral parameters (wavelength, lifetime, polarization) [20, 21, 22], more complex objects of investigation (dendrimeric systems, ion channels) [23, 24] and more demanding physiological environments [25, 26] are being studied using single-molecule techniques. With the discovery that the Raman cross sections of a molecule can be enhanced by up to 14 orders of magnitude when it is adsorbed on a metal nanoparticle (surface-enhanced Raman scattering, SERS) even the Raman detection and imaging mode became feasible [27] which was unconceivable before.

The fact that single-molecule detection has become a mature technique manifests itself in the huge number of applications it has found in very diverse fields. Due to their unique properties single molecules are proposed as sources for single photons in quantum cryptography and quantum computation [28], as point-like probes in optical microscopy [29] and as local reporters of conformation, position [30] and even magnetization[31, 32]. For further reading on the development, spectroscopical aspects and applications of single-molecule research it is referred to the large number of available monographs [33, 34, 35, 36] and review articles [37, 38, 39, 40, 41].

To understand the photophysical features and peculiarities of single molecules one has to dwell on the molecular photophysics of organic fluorophores whose underlying principles are briefly reviewed in the following.

1.2 Molecular Photophysics

The interaction of light with matter in a system consisting of two distinct energetical states (two-level system) is described by Einstein's model of absorption, spontaneous emission and stimulated emission [42]. While the transitions in a two-level system are relatively easy to describe, the situation is considerably more complex in an organic molecule consisting of a few tens of atoms. A common approach to simplify this quantum-mechanical problem is the Born-Oppenheimer approximation [43] which states that electronic transitions occur on a much faster timescale than nuclear motions and can thus be separated from nuclear vibrations and rotations:

$$\Psi(\boldsymbol{r}, \boldsymbol{R}) = \varphi(\boldsymbol{r}; \boldsymbol{R})\, \Phi(\boldsymbol{R})\, \theta(\boldsymbol{R}). \tag{1.1}$$

Here, $\boldsymbol{r}$ and $\boldsymbol{R}$ are the electronic and nuclear coordinates, $\varphi(\boldsymbol{r}; \boldsymbol{R})$ is the purely electronic wavefunction (in the static field of the nuclei), $\Phi(\boldsymbol{R})$ and $\theta(\boldsymbol{R})$ are, respectively, the vibrational and rotational wavefunctions of the nuclei and $\Psi(\boldsymbol{r}, \boldsymbol{R})$ is the total wavefunction of the molecule. The simplest model to describe the molecular vibrations is the harmonic oscillator model which may optionally be extended by an anharmonic contribution (e.g. the Morse potential) to account for effects like dissociation. Likewise, rotational motion can be described in terms of the rigid rotator model, optionally enhanced

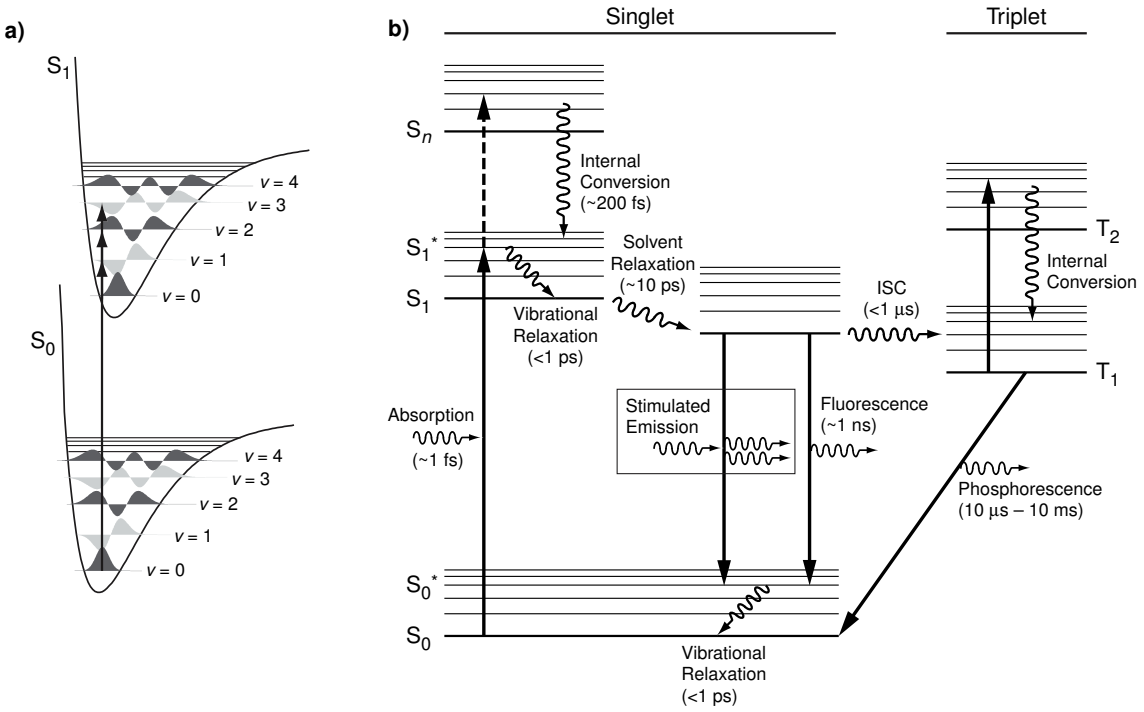

Fig. 1.1: Visualization of the Franck-Condon principle (a) and Jablonski diagram (b). The electronic states of an organic fluorophore and transitions between these states are shown along with their characteristic times. Wiggled lines indicate radiationless transitions, ISC denotes intersystem crossing from the singlet to the triplet system. Timescales are approximate and may vary according to the fluorophore and the solvent.

by higher-order terms. Due to their low energetic contributions, however, rotations are commonly neglected in the pictorial models of polyatomic molecules. The main features of the electronic states can be qualitatively derived from the simplistic LCAO model (linear combination of atomic orbitals) which shows that the electrons in the ground state are paired in most molecules such that no net spin results. Hence, with only few exceptions, the ground state of an organic molecule is a singlet state denoted as S_0.

While the potential energy of a diatomic molecule can easily be plotted as a function of the nuclear distance this is impossible for the energy hypersurface of an N-atomic molecule which has $(3N-6)$ degrees of freedom. For a qualitative discussion of the processes that may occur in a molecule [44] it is instructive, however, to select a single normal mode of vibration and to depict the energy as a function of the respective normal coordinate. A generic potential energy curve including the vibrational levels and wavefunctions is depicted in Fig. 1.1a for both the electronic ground state S_0 and the first excited state S_1. The minima of the two curves are slightly offset which is due to a more or less pronounced rearrangement of the nuclei in the excited state. Because these rearrangements are slow compared to electronic transitions the latter occur as vertical transitions in the energy dia-

gram (Franck-Condon principle [43]). The vibrational structure of an electronic transition can be derived from the probability of a vibronic transition between an initial level 'i' and a final level 'f' which is proportional to the square of the transition dipole moment $\mathbf{M}_{\mathrm{if}}$ [44]:

$$|\mathbf{M}_{\mathrm{if}}|^2 = |\langle\Psi_{\mathrm{i}}|\hat{\mu}|\Psi_{\mathrm{f}}\rangle|^2 = |\langle\varphi_{\mathrm{i}}|\hat{\mu}_{\mathrm{el}}|\varphi_{\mathrm{f}}\rangle|^2 \, |\langle\Phi_{\mathrm{i}}|\Phi_{\mathrm{f}}\rangle|^2 \tag{1.2}$$

where $\hat{\mu}$ is the (electronic and nuclear) dipole moment operator, $\hat{\mu}_{\mathrm{el}}$ is the purely electronic dipole moment operator and the rotational contribution has been neglected. Pictorially, the Franck-Condon factor $S_{\mathrm{if}} = |\langle\Phi_{\mathrm{i}}|\Phi_{\mathrm{f}}\rangle|^2$ is given by the (square of the) overlap between the initial and final wavefunctions. Its significance is that it determines to what extent the particular transition $|\mathrm{i}\rangle \rightarrow |\mathrm{f}\rangle$ contributes to the electronic band.

The photophysical processes succeeding excitation can be best described in terms of the Jablonski diagram shown in Fig. 1.1b which gives a simplified picture of the energy levels and the transitions among them. The processes immediately following excitation are partly intrinsic to the molecule (vibrational relaxation) and partly depend on the solvation environment (vibrational cooling, solvent relaxation). The fastest relaxation processes involve an adiabatic redistribution of the vibrational energy in the S_1 manifold (intramolecular vibrational redistribution, IVR) which occurs on a (sub)picosecond timescale [45] and results in a high-temperature thermal equilibrium. Within the subsequent 5–50 ps the vibrationally hot molecule cools by dissipation of energy to the surrounding solvent molecules via collisional interactions [46]. The collosional cooling is accompanied by a reorientation of the surrounding solvent molecules in response to the changes in the molecule's dipole moment upon excitation (solvent relaxation [47]) which causes an additional lowering of the S_1 energy level.

The fact that all these relaxation processes are orders of magitude faster than the radiative lifetime of the vibrationally relaxed S_1 state ($\tau_{\mathrm{fl}} \approx 1$ ns) accounts for the finding that — with few exceptions — fluorescence generally occurs from the S_1 state (Kasha's rule [48]). This even holds if, initially, higher electronic states S_n are populated because these undergo fast (~ 200 fs) internal conversion (IC) to high lying vibrational levels S_1^*. Due to the fast relaxation processes, the fluorescence spectrum is not only red-shifted with respect to the absorption spectrum (Stokes' shift [44, 47]) but is also independent of the excitation wavelength.

While the molecule is in its S_1 state, an electronic transition to the ground state may not only occur due to spontaneous fluorescence emission, but it can be stimulated by an incident photon which triggers the emission of a second coherent photon from the molecule. Depending on the energy of the incident photon, the molecule may be left in a vibrationally excited level S_0^* which, again, is subject to vibrational relaxation [49]. Once the molecule is back in its vibronic ground state, it is ready for a new excitation-emission cycle.

Further processes may occur from the excited singlet state most of which are, however, less frequent in a good fluorophore. These include intersystem-crossing (ISC) to the triplet state T_1, which is spin-forbidden but can be promoted by the enhanced spin-orbit coupling in the prescence of atoms with higher atomic numbers (heavy atom effect [44]). Collisional quenching, excitated state reactions (proton loss/ gain/ tautomerization, excimer or exciplex formation) and resonance energy transfer (RET) [47] are further examples of photophysical and photochemical processes which are (apart from their involvement in photobleaching) less important for the studies presented in this work.

1.2.1 Photophysical Peculiarities of Single Molecules

One of the first effects that were reported when single fluorophores were studied was that fluorescence is emitted in bursts rather than continuously [50, 51]. This blinking is almost invariably observed [52] in all kinds of fluorophores including fluorescent proteins [53] and under diverse environmental conditions and has therefore become one of the hallmarks of single-molecule observation. The blinking is attributed to temporal transitions of the molecule to nonfluorescent dark states and has been analyzed in terms of the on- and off-time histograms as well as by correlation analysis of the fluorescence emission. These studies have shown that transitions to and from dark states occur on a large range of timescales, i.e. from microseconds up to minutes [53]. As to the nature of these nonfluorescent states, several mechanisms have been proposed and have been supported with experimental evidence. One of the most obvious dark states is the triplet state T_1 which is populated through intersystem crossing (ISC). Several studies based on correlation analysis of the fluorescence signal both in solution [54] and in dye-doped nanocrystals [55, 56] have consistently revealed ISC rates on the order of $\sim$1 μs. As was proposed recently, the triplet state may also serve as a transient state for the formation of another dark state, arguably a radical anion as a result of photoinduced intermolecular electron transfer [57]. Dim states with off-times of more than 100 ms may hardly be explained in terms of triplet formation (which would be incompatible with its lifetime) but are postulated to be due to intermolecular energy transfer or to photochemical changes like photoinduced isomerization [58], conformational changes or reversible oxidation [59] to name just a few. These processes may also be responsible for spectral diffusion [60] and spectral jumps [61] that are frequently observed in single-molecule fluorescence experiments.

Further investigations of the photon statistics [62] of single-molecule fluorescence emission on short timescales revealed the interesting phenomenon of photon antibunching [63, 64, 65] which manifests itself as a dip in the histogram of interphoton arrival times (or, likewise, in the autocorrelation curve) as the interphoton time approaches zero. The effect is easily explained by the fact that after a molecule has emitted a photon, it must be excited again before the next photon can be emitted. As a result, photons are generated

one by one which renders single molecules an interesting single-photon source for use in e.g. quantum cryptography [28].

Eventually, photobleaching leads to an abrupt and irreversible cessation of the fluorescence emission from a single molecule. However, the decision on when the cessation of fluorescence is irreversible is difficult if not impossible to make because dark states may persist for extended periods of time and may yet be transient. Therefore, the duration of an experiment is commonly taken as the time limit after which a nonemitting molecule is considered bleached. Photobleaching inevitably restricts the number of photons that can be detected from a single molecule and therefore limits the attainable signal-to-noise ratio in an experiment. While, at low temperatures, $> 10^{10}$ photons may be detected [59] the number of emitted photons drops to 10^5–10^6 at room temperature [38]. Most commonly, it is assumed that photobleaching is due to photooxidation by highly reactive singlet ($^1\Delta_g$) oxygen [66]. In fact, for single terrylene molecules in a *p*-terphenyl host crystal, a self-sensitized photooxidation scheme has been supported by the identification of an exoperoxide intermediate [59]. However, further pathways must exist which account for the finding that, to a lesser extent, even in oxygen-free environments photobleaching occurs. A recently proposed bleaching mechanism postulates a radical anion formed from the triplet by electron transfer as an intermediate [57, 67].

1.2.2 Stimulated Emission Depletion

The significance of stimulated emission is not only based on the coherent emission of a photon (which constitutes the basis for laser action) but also on the quenching of fluorescence which can be used to probe the population of the excited state S_1 with high temporal and spectral resolution. Therefore, stimulated emission depletion (STED, also termed stimulated emission pumping, SEP) is equally useful for time-resolved spectroscopic applications [68, 69, 70, 71].

Commonly, the processes involved in a STED experiment are modeled by using the four-level system [72, 73, 74] shown in Fig. 1.2 which constitutes a simplification of the Jablonski diagram (Fig. 1.1b). The model includes the electronic ground state S_0, the initially populated Franck-Condon level S_1^*, the relaxed electronic state S_1 and the vibrationally excited ground level S_0^*. Denoting the populations of the these states by the respective italicized letters, the temporal evolution of the populations of these four levels is uniquely determined by the following set of coupled differential equations:

$$\frac{\mathrm{d}S_0(t)}{\mathrm{d}t} = k_{\mathrm{exc}}(t)\,[S_1^*(t) - S_0(t)] + k_{\mathrm{vib},0}S_0^*(t) \tag{1.3a}$$

$$\frac{\mathrm{d}S_0^*(t)}{\mathrm{d}t} = k_{\mathrm{fl}}S_1(t) + k_{\mathrm{STED}}(t)\,[S_1(t) - S_0^*(t)] - k_{\mathrm{vib},0}S_0^*(t) \tag{1.3b}$$

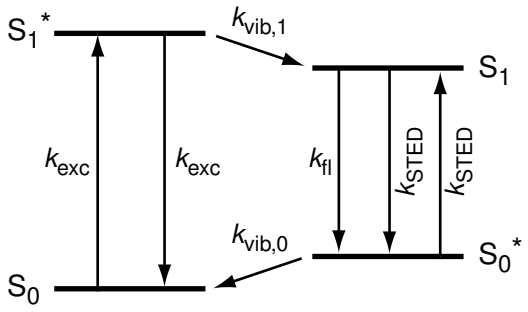

Fig. 1.2: Simplified four-level system to describe the excitation and STED processes.

$$\frac{\mathrm{d}S_1(t)}{\mathrm{d}t} = -k_{\mathrm{fl}} S_1(t) + k_{\mathrm{STED}}(t)\,[S_0^*(t) - S_1(t)] + k_{\mathrm{vib},1} S_1^*(t) \tag{1.3c}$$

$$\frac{\mathrm{d}S_1^*(t)}{\mathrm{d}t} = k_{\mathrm{exc}}(t)\,[S_0(t) - S_1^*(t)] - k_{\mathrm{vib},1} S_1^*(t) \tag{1.3d}$$

The rate constants of fluorescence (k_{fl}) and of vibrational relaxation ($k_{\mathrm{vib},0}$, $k_{\mathrm{vib},1}$) are mostly intrinsic to the fluorophore under investigation, but they also depend to some extend on the solvation environment, in particular, on its polarity. On the contrary, the rate constants of excitation (k_{exc}) and stimulated emission (k_{STED}) are given as a product of a wavelength-dependent cross section and a laser intensity:

$$k_{\mathrm{exc}}(t) = \sigma_{\mathrm{abs}}\, h_{\mathrm{exc}}(t) \tag{1.4a}$$

$$k_{\mathrm{STED}}(t) = \sigma_{\mathrm{STED}}\, h_{\mathrm{STED}}(t). \tag{1.4b}$$

where $h_{\mathrm{exc}}(t)$, $h_{\mathrm{STED}}(t)$ are the excitation and the STED laser intensities measured in [photons/ (s$\times$cm^2)] and σ_{abs}, σ_{STED} are the absorption and stimulated emission cross sections, respectively. Because the cross sections have units of [cm^2], they are often interpreted as the molecule's photon caption area.

The four-level model is flexible enough to address many of the questions related to the dynamics of stimulated emission and its application to pump-probe spectroscopy. Likewise, it is applicable to analyze and to optimize the conditions for STED microscopy. In particular, the fluorescence depletion efficiency as a function of STED intensity can be studied and, for pulsed operation, the pulse duration, its temporal shape and the pulse timing can be optimized.

As an example, Fig. 1.3 shows the numerical simulation of an experiment with pulsed excitation and stimulated emission where the fluorescence signal $F = \int k_{\mathrm{fl}} S_1(t)\mathrm{d}t$ is calculated for increasing delays of the STED pulse with respect to the excitation pulse. The delay ranges up to 10 ns with a resolution of 10 fs and thus covers both the vibrational relaxation (${k_{\mathrm{vib}}}^{-1} = 500$ fs) and the fluorescence decay (${k_{\mathrm{fl}}}^{-1} = 2$ ns) of the dye. This example demonstrates the wide dynamic range and the high time resolution which is solely limited by the duration of the excitation and STED laser pulses (which were assumed

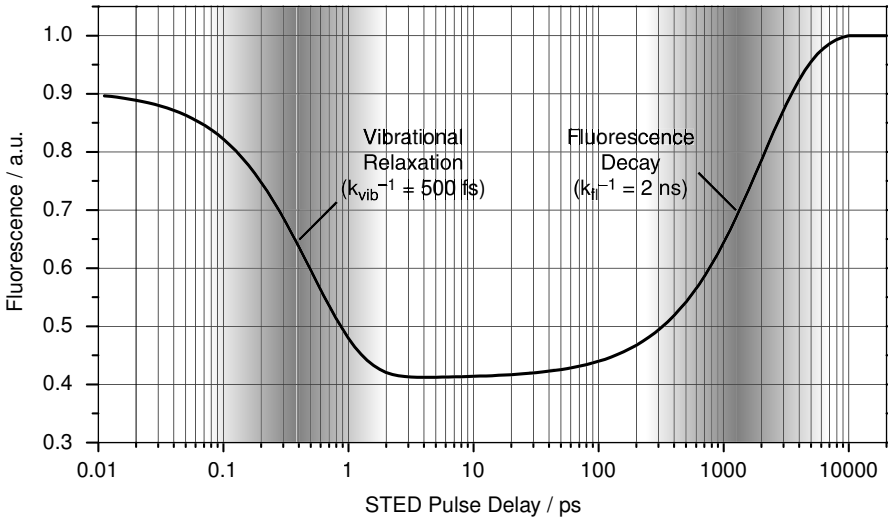

Fig. 1.3: Numerical simulation of the molecular dynamics probed by stimulated emission depletion at increasing STED pulse delays. The gray shaded regions highlight the ultrafast vibrational relaxation processes between 0.1 and 1 ps and the fluorescence decay in the nanosecond range. (Pulse lengths: 100 fs; peak intensities: 1 GW cm^{-2} (excitation), 273 GW cm^{-2} (STED); absorption and stimulated emission cross sections: 10^{-16} cm^2).

to be 100 fs here). In fact, this kind of experiment was used to unravel the vibrational relaxation dynamics of Rhodamine 700 and Oxazine 750 [75, 46]. While the four-level model is rather comprehensive and thus provides high flexibility it may prove beneficial to simplify the model to cover only particular aspects of the STED dynamics. Along these lines, two simplified models will be analyzed in Chap. 3 and will be used to extract the stimulated emission cross sections from STED saturation data.

Besides its potential for time-resolved spectroscopy, STED has proven useful in fluorescence microsopy where it has been established to reduce the effective detection volume and thereby to push the spatial resolution beyond the diffraction limit (see Sects. 1.3 and 2.5). Meanwhile, resolutions of down to 25–30 nm have been achieved in an optical STED microscope [76, 29]. However, the reduction of the effective volume is not only useful for fluorescence imaging with super-resolution, but it may also contribute to the progress of fluorescence fluctuation spectroscopy by allowing to perform experiments at higher solute concentrations. The results of a respective study is presented in Chap. 4 of this thesis.

1.3 Microscopy at and Beyond the Diffraction Limit

As was pointed out in the introductory sections, the key challenge in single-molecule fluorescence is background suppression rather than instrumental sensitivity. Today, one

of the most common approaches is to use confocal microscopy in order to reduce the detection volume as much as possible. As has been proven in the past years, the STED microscope allows to reduce the detection volume beyond the diffraction limit which is why its adoption for single-molecule detection is highly desirable. As the operating principles of both types of microscope play an important role in Chaps. 2 and 4 the theory underlying their operation is briefly reviewed here. For more in-depth information see [77, 78] and [72, 79].

Already in 1873, *Ernst Abbe* recognized that the resolution of an optical microscope cannot be arbitrarily improved but is subject to a fundamental limit, the so-called diffraction limit [80]. The reason is that if a point-like light source is imaged using a lens, the image of the source is not point-like but has a finite extension. The intensity distribution in the focal plane $h(\boldsymbol{r})$ (called the point-spread function, PSF) is given by the square of the field amplitude $E(\boldsymbol{r})$ which according to scalar diffraction theory [81] is given by:

$$h(\boldsymbol{r}) = |E(\boldsymbol{r})|^2 = E_0 \int_0^{\alpha} \sqrt{\cos\theta}\sin\theta J_0\left(k\sqrt{x^2+y^2}\sin\theta\right)\exp\left(ikz\cos\theta\right)\mathrm{d}\theta \tag{1.5}$$

where $\boldsymbol{r} = (x, y, z)$ are the spatial coordinates, E_0 is a constant which scales with the incident optical power, α is half the aperture angle of the lens, θ is the integration variable, $J_0()$ is the zero-order Bessel function of the first kind, n is the refractive index of the medium and $k = 2\pi n/\lambda_0$ and λ_0 are, respectively, the the wavenumber and the vacuum wavelength of the focused light.

According to the Rayleigh criterion, the resolution of a microscope is given by half the diameter of the Airy disk which is defined as the lateral distance between the minima of $h(\boldsymbol{r})$ that enclose the main maximum. For the epifluorescence microscope the diameter of the Airy disk is given by:

$$\Delta x = 1.22\frac{\lambda_0}{\mathrm{NA}}. \tag{1.6}$$

where $\mathrm{NA} = n\sin\alpha$ is the numerical aperture of the lens. The same criterion can be used to define the axial resolution. In this case, the minima are separated by

$$\Delta z = 4.00\frac{n\,\lambda_0}{\mathrm{NA}^2}. \tag{1.7}$$

Instead of the Rayleigh criterion, the full-width at half-maximum (FWHM) of the PSF is also sometimes used to characterize the optical resolution of a microscope.

Alternatively, the performance of a microscope can be specified in the frequency domain. The counterpart of the point-spread function is the optical transfer function (OTF)

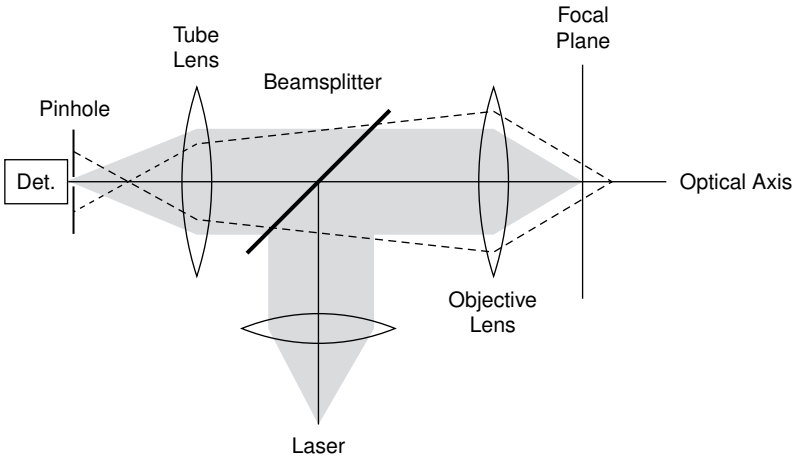

Fig. 1.4: Main components and operating principle of a confocal microscope.

which is related to the PSF by a simple Fourier transform. It describes the optical resolution in terms of the instrument's transmittance as a functon of the spatial frequency. In order to image small features high frequencies are required. Thus, enhancing the resolution of a microscope is equivalent to widening the support of the OTF. For a detailed introduction into Fourier optics and the OTF of the confocal microscope, see [81, 82].

1.3.1 The Confocal Microscope

The main feature of a confocal compared to a widefield microscope is its optical sectioning capability. The origin of this depth discrimination can be explained from the drawing of a confocal microscope as depicted in Fig. 1.4. A point-like light source, e.g. a laser beam focused through a micrometer-sized pinhole or emitted from the end of a single-mode optical fiber, is collimated and is focused into the sample by the objective lens. The signal emitted from the sample is usually collected by the same objective lens (epifluorescence), is separated from the excitation light by a dichroic beamsplitter and is focused through a pinhole in the detection path onto the detector. As is illustrated by the optical path drawn in dotted lines, any fluorescence that originates outside the focal plane is not focused through the pinhole and is therefore suppressed. That is, the pinhole in front of the detector is responsible for the depth discrimination.

For a quantitative description of the image formation in a confocal microscope, the detection process is interpreted as imaging the detection pinhole into the sample space (which is permissible because the light paths are reversible). Hence, the effective PSF of the confocal microscope is given by the product of the excitation PSF $h_{\mathrm{exc}}(\boldsymbol{r})$ and the detection PSF $h_{\mathrm{det}}(\boldsymbol{r})$. It must be considered, though, that the detection pinhole in a real setup is not point-like but has a finite diameter. The detection PSF must therefore be

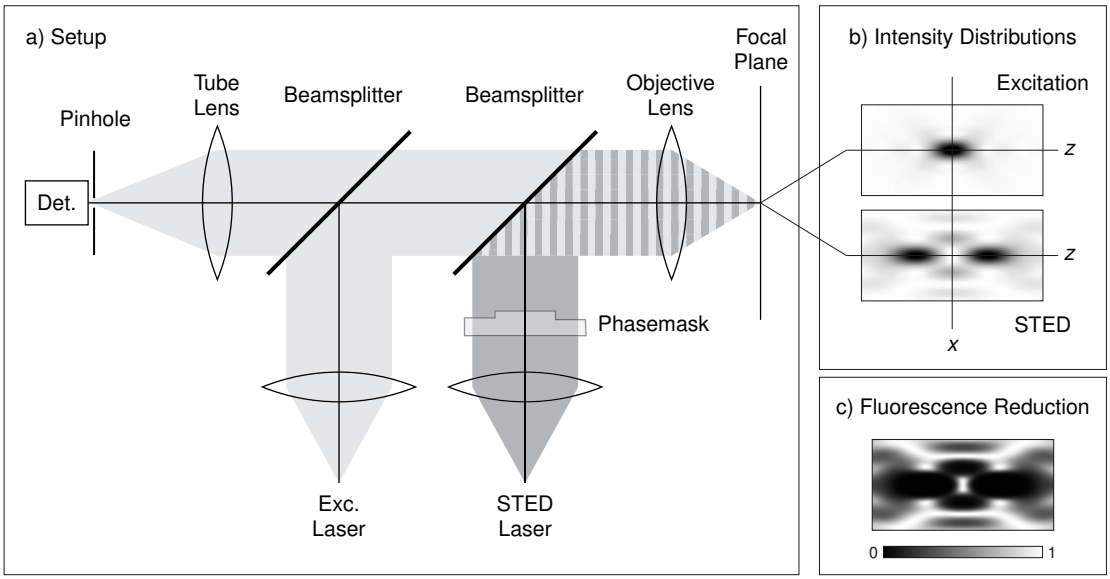

Fig. 1.5: a) Main components and operating principle of a STED microscope, b) intensity distributions of the excitation and STED foci (when a circular phase retardation filter is used), c) map of the local STED efficiencies which indicates where fluorescence is suppressed (dark regions) and where it remains unaffected (bright regions).

convolved with a pinhole function

$$o(\boldsymbol{r}) = \begin{cases} 1 & \text{if } \sqrt{x^2+y^2} < d/(2M) \\ 0 & \text{else} \end{cases} \tag{1.8}$$

which is the detection pinhole (with diameter d) projected into focal space. Here, d is the diameter of the detection pinhole and M is the magnification of the microscope. Accordingly, the confocal PSF is given by

$$h_{\text{conf}}(\boldsymbol{r}) = h_{\text{exc}}(\boldsymbol{r})\,[h_{\text{det}}(\boldsymbol{r}) \otimes o(\boldsymbol{r})]\,. \tag{1.9}$$

1.3.2 The STED Microscope

In a STED microscope, the ability to suppress fluorescence emission in a controlled way by stimulated emission is exploited to enhance the optical resolution beyond that of a confocal microscope and even far beyond the diffraction limit. From an instrumental point of view, the design of a STED microscope is similar to that of a confocal one, but it is extended by an additional (STED) laser beam which is coupled into the objective lens colinearly to the excitation beam (Fig. 1.5a). Both beams are aligned such that their foci coincide in space. However, in order to achieve a resolution enhancement, the STED focus has be to engineered to provide a zero-intensity minimum in the geometrical center

and high intensities in the focal periphery. Thus, only molecules in the very center of both the excitation and the STED PSFs contribute to the fluorescence signal, while molecules in the outer regions of the excitation PSF get quenchend by the STED light.

Several techniques are conceivable to design a STED focus shaped according to these requirements. A technically simple implementation, shown in the figure, is to position a properly designed phase retardation filter into the expanded STED beam which spatially modulates the phase front of the STED beam. As an example, by placing a circular phasefilter into the beam which introduces a phase shift of π on half of the area of the back aperture of the objective lens, the focal intensity distribution shown in Fig. 1.5b is obtained, which features two axially offset main maxima along with smaller laterally offset side maxima. Due to the axial main maxima, the effective PSF of the microscope is mainly confined along the optical axis. The effect is more pronounced than one would expect from the STED PSF in Fig. 1.5b because the STED efficiency depends nonlinearly on the intensity. To a good approximation, the factor $\eta(\boldsymbol{r})$ by which the fluorescence is reduced is given by an exponentially saturating function of the STED intensity (see Chap 3). Therefore, given the STED-PSF shown in Fig. 1.5b, the fluorescence is effectively quenched as is visualized in Fig. 1.5c where dark tones indicate fluorescence quenching. Quantitatively, for a given $\eta(\boldsymbol{r})$, the effective PSF of the STED microscope is easily derived from Eq. (1.9) for the confocal microsope by simple multiplication with $\eta(\boldsymbol{r})$:

$$h_{\text{eff}}(\boldsymbol{r}) = \eta(\boldsymbol{r}) h_{\text{exc}}(\boldsymbol{r}) \left[h_{\text{det}}(\boldsymbol{r}) \otimes o(\boldsymbol{r})\right] \tag{1.10}$$

More advanced but conceptionally equivalent techniques for wavefront engineering make use of adaptive optical elements such as spatial light modulators (SLM) which, in addition, allow to correct for imperfections in the wavefront and are more flexible. A slightly different approach is to use a 4Pi microscope where the central minimum is achieved by destructive interference of two counterpropagating beams which are coherently focused onto a common focal spot using two opposing objective lenses [76].

In order to derive the effective PSF of a STED microscope according to Eq. (1.10) it is necessary to calculate the excitation and STED-PSFs previously. This can be done in terms of vectorial diffraction theory [81, 83] which states that:

$$\begin{aligned} h_{\text{STED}}(\boldsymbol{r}) &= \frac{\lambda_0\, n\, \varepsilon_0}{2h} \left|\boldsymbol{E}(\boldsymbol{r})\right|^2 \\ &= \frac{n^3\, \varepsilon_0}{2h\lambda_0} \left| \int_0^{\alpha} \int_0^{2\pi} E_0(\theta) \sqrt{\cos\theta} \sin\theta \exp\left\{i\left[\Psi(\theta,\phi') + k(s-f)\right]\right\} \right. \\ &\quad \left. \times \begin{pmatrix} \cos^2(\phi'-\phi)\cos\theta + \sin^2(\phi'-\phi) \\ \sin(\phi'-\phi)\cos(\phi'-\phi)(\cos\theta - 1) \\ -\cos(\phi'-\phi)\sin\theta \end{pmatrix} \mathrm{d}\phi' \mathrm{d}\theta \right|^2 . \end{aligned} \tag{1.11}$$

Here, $h_{\mathrm{STED}}(\boldsymbol{r})$ is given in photons per unit area and time, $\varepsilon_0 = 8.8542 \times 10^{-12}$ C^2 N^{-1} m^{-2} is the permittivity of free space, f is the focal length and s is the distance from the point (f, θ, ϕ') on the converging wavefront to $\boldsymbol{r} = (r, z, \phi)$ which is given in cylindrical coordinates. Finally, the phasefilter is described by the phase function $\Psi(\theta, \phi')$ which e.g. is zero for a plane wavefront.

These equations can be used to evaluate the suitability of different phasefilters with respect to optical imaging or to spectroscopic applications. Details on various phasefilters for use in fluctuation spectroscopy are discussed in Chap. 4.

Chapter 2

STED on Single Molecules

2.1 Materials and Methods

2.1.1 Experimental Setup

The initial challenge of this thesis was to design and build a table-top confocal microscope which, unlike commercially available instruments, was optimized for two-color operation in combination with a high detection efficiency, as is required for STED experiments on single molecules. The main components of the setup are outlined in Fig. 2.1, but for the particular requirements of each experiment, the setup was modified and complemented as is described in the respective chapters.

The two wavelengths required to perform STED experiments were derived from a passively mode-locked Ti:Sapphire laser (Ti:Sa, Model Mira-900F, Coherent, Santa Clara, CA, USA) operating at a repetition rate of $\sim$76 MHz and at wavelengths between 720 and 900 nm. The output of this laser was partly used to pump an intracavity frequency-doubled optical parametric oscillator (OPO Advanced, APE, Berlin, Germany) which generated a synchronized pulse train in the visible between 550 and 620 nm. While the OPO was used to excite fluorescence, the remainder of the Ti:Sapphire light that left the OPO was initially used to effect stimulated emission, but it was later found more favourable to couple out the STED beam in front of the OPO using a variable beamsplitter. The operating wavelengths were measured using fiber-coupled spectrometers (USB2000, OceanOptics B.V., Duiven, Netherlands and PMA-11, Hamamatsu Deutschland, Herrsching am Ammersee, Germany) and were adjusted to match the employed fluorophores. Both laser beams were power-controlled and stabilized with two liquid-crystal based laser power controllers (LPC-VIS/ LPC-NIR, Cambridge Research & Instrumentation, Woburn, MA, USA, now manufactured by Brockton Electro-Optics Corp., Brockton, MA, USA).

The 150–200 fs pulses delivered by the Ti:Sapphire laser and the OPO were stetched

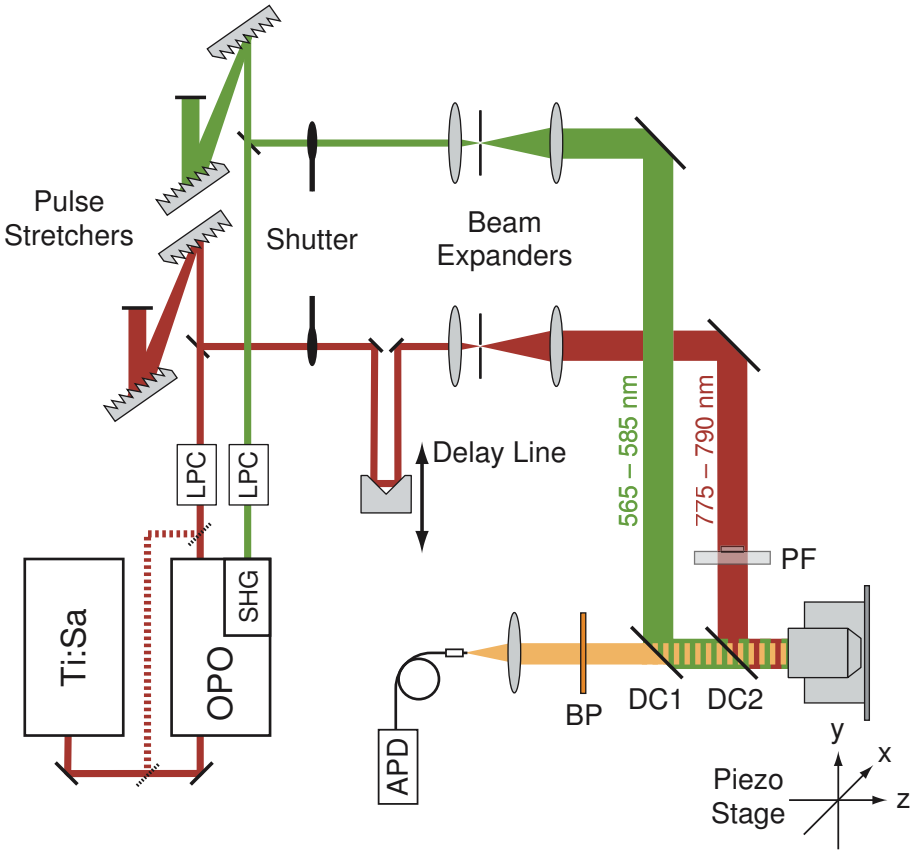

Fig. 2.1: Experimental Setup. See text for explanations.

using two grating based pulse stretchers which provided pulse lengths up to ∼15 ps. Pulse lengths in the range of 100 fs to 15 ps were measured by optical autocorrelation (PulseScope/ Autocorrelator Mini, APE, Berlin, Germany), and pulses >50 ps were characterized by direct measurement of the temporal pulse profile using a fast MCP detector (MCP-PMT R3809U-50, Hamamatsu) in conjunction with time-correlated single-photon counting (TCSPC) electronics (SPC-730/ SPC-830, Becker & Hickl, Berlin, Germany). The measured pulse lengths were deconvolved to correct for the response time of the TCSPC system which was measured to be ∼45 ps. The timing between the OPO and the Ti:Sapphire pulses was adjusted via an optical delay line (LIMES 170, Controller DC-500, Owis GmbH, Staufen, Germany) which allowed a temporal adjustment of the STED pulses on a range of 4 ns.

Both laser beams were expanded using two telescopes which were equipped with pinholes (50–60 μm) for spatial filtration. The expanded and collimated beams were coupled into the microscope using two custom-tailored dichroic beamsplitters DC1 (628dclpxr, Chroma Technology, Rockingham, VT, USA) and DC2 (720drspxr, Chroma Technology). A phase retardation filter (PF) was placed into the expanded STED beam as needed by

the respective experiments. Unless otherwise noted, the beams were focused using a 1.4 NA/ 100x oil immersion lens (PL APO 100×/1.40 – 0.7 OIL, Leica, Wetzlar, Germany). The (epi)fluorescence was collected by the same lens, passed the two dichroic filters, was separated from the laser light by a bandpass filter BP (D680/60, Chroma Technology) and was focused into a multimode fiber ($d = 62.5\ \mu\mathrm{m}$, M31L01, Thorlabs GmbH, Karlsfeld, Germany) which served as the confocal pinhole. The signal was detected using a fiber-coupled single-photon counting module based on an avalanche photodiode (APD, SPCM-AQR-13-FC, PerkinElmer OptoElectronics Europe, Wiesbaden, Germany), and the photocounts were acquired and processed using the same TCSPC electronics which was used for the laser pulse characterization (SPC-730/ SPC-830, Becker & Hickl).

Object scanning was implemented by mounting the samples on a 3D piezo scanning stage with closed-loop control (TRITOR-102CAP, Piezosystem Jena, Jena, Germany) which provided a scanrange of 80 μm in all three directions. The overlap of the two laser foci was aligned by alternately scanning immobilized gold nanoparticles in reflectance mode with the excitation and the STED laser. The procedure was repeated for all three spatial directions. For this adjustment procedure, the bandpass filter in the detection path was replaced by a neutral density filter matched to the brightness of the gold nanobeads.

The detection efficiency of the setup can be estimated on the basis of the following collection efficiencies and transmission values: solid angle of detection ($q = 0.31$), transmission of the objective lens at the fluorescence wavelength ($T = 0.80$), reflectivity of the silver mirrors ($R = 0.97$), transmission of the dichroic beamsplitters and bandpass filters (720drsxpr[1]: $T = 0.86$, 628dcltxr[1]: $T = 0.93$, D680/60[1]: $T = 0.45$), transmission of the tube lens ($T = 0.95$), coupling efficiency into the multimode fiber ($q = 0.80$), pinhole discrimination (1.05 Airy disks, $q = 0.95$), quantum efficiency of the detector ($q = 0.72$). The net detection efficiency is obtained by multiplication of these factors and yields a value of 4.2%.

2.1.2 Dyes and Sample Preparation

The fluorescent dyes used in this work were primarily selected based on their spectral properties. In particular, as stimulated emission was carried out in the long-wavelength part of the fluorescence spectrum, the emission range had to be matched to the tuning range of the Ti:Sapphire laser. In addition, because the wavelength of the exitation laser (OPO) was coupled to that of the STED laser, appreciable absorption at the accompanying excitation wavelength had to be guaranteed. Given a satisfactory choice of commercially available dyes which fulfill these spectroscopic requirements, the photostability became the essential selection criterion. Typically, at room temperature, only 10^5–10^6 photons are

[1]Determined from the fluorescence emission spectrum of JA 26 weighted by the transmission values measured at an AOI of $45°$.

emitted by an organic fluorophore before photobleaching occurs [38] so, in order to be able to perform quantitative measurements at reasonable signal-to-noise ratios, care had to be taken to ensure adequate photostability.

Initial comparative experiments revealed an extremely broad range of photostabilities with e.g. the BODIPY 650/665-X dye residing at the low end and various xanthene and oxazine dyes at the high end. These results were in accordance with previous findings which had classified Rhodamine 700 among the most photostable laser dyes with high absorbance [$\varepsilon(643\ \mathrm{nm}) = 9.25 \times 10^4\ \mathrm{M}^{-1}\ \mathrm{cm}^{-1}$] [84]. Finally, the two dyes JA 26 and MR 121 were chosen for the single-molecule experiments to be performed. Figure 2.2 summarizes some of the photophyiscal properties of these dyes and indicates the wavelengths employed in the STED experiments. Both dyes were obtained from Prof. Drexhage (University of Siegen, Germany) and were used without further purification. While the former dye has proven most photostable in the selection process, it has the tendency to decompose in solution. This decomposition is particularly pronounced in aqueous solution but can be reduced when the solution is acidified. Therefore, in the sample preparation, JA 26 was dissolved in water that was adjusted to $\mathrm{pH} \approx 3$ by addition of 1 M hydrochloric acid. Unlike JA 26, the oxazine MR 121 is chemically stable in solution but is slightly less photostable while featuring similar absorption and fluorescence spectra. Therefore, JA 26 was used to prepare samples whith single molecules embedded in a polymer matrix while MR 121 was used for the FCS experiments in solution.

To prepare samples with single molecules immersed in a polymer matrix, standard glass cover slides were cleaned using a commercial laboratory glass cleaner (Mucasol, 3%, Merz, Frankfurt, Germany) and thouroughly rinsed with ultrapure water. Poly(vinyl alcohol) (PVA, $M_\mathrm{W} \approx 25000$, #02975, Polysciences, Inc., Warrington, PA, USA) was dissolved in ultrapure water at a concentration of 50 mg/mL and was purified by dialysis (ZelluTrans, MWCO: 12,000–14,000, 10mm, #E672.1, Roth GmbH, Karlsruhe, Germany). The dye solution was diluted to $\sim$1 nM, and 20μL/mL PVA solution was added. About 100–200 μL of this solution were spin coated onto a cleaned coverslip (4000 RPM, 30 s). The samples were kept dark and dry in a desiccator and were purged with argon gas during the measurements. The alignment sample was prepared similarly by spincoating an aqueous solution of PVA with suspended gold nanoparticles (80–150 nm, British Biocell International Ltd., Cardiff, UK) onto a cleaned coverslip.

2.2 Switching Off Single Molecules

The first experiment performed in the context of this thesis was a proof-of-concept experiment which served both to demonstrate the suitability of the setup for single-molecule spectroscopy in terms of sensitivity and background and to prove the feasibility of the STED concept when applied to single molecules.

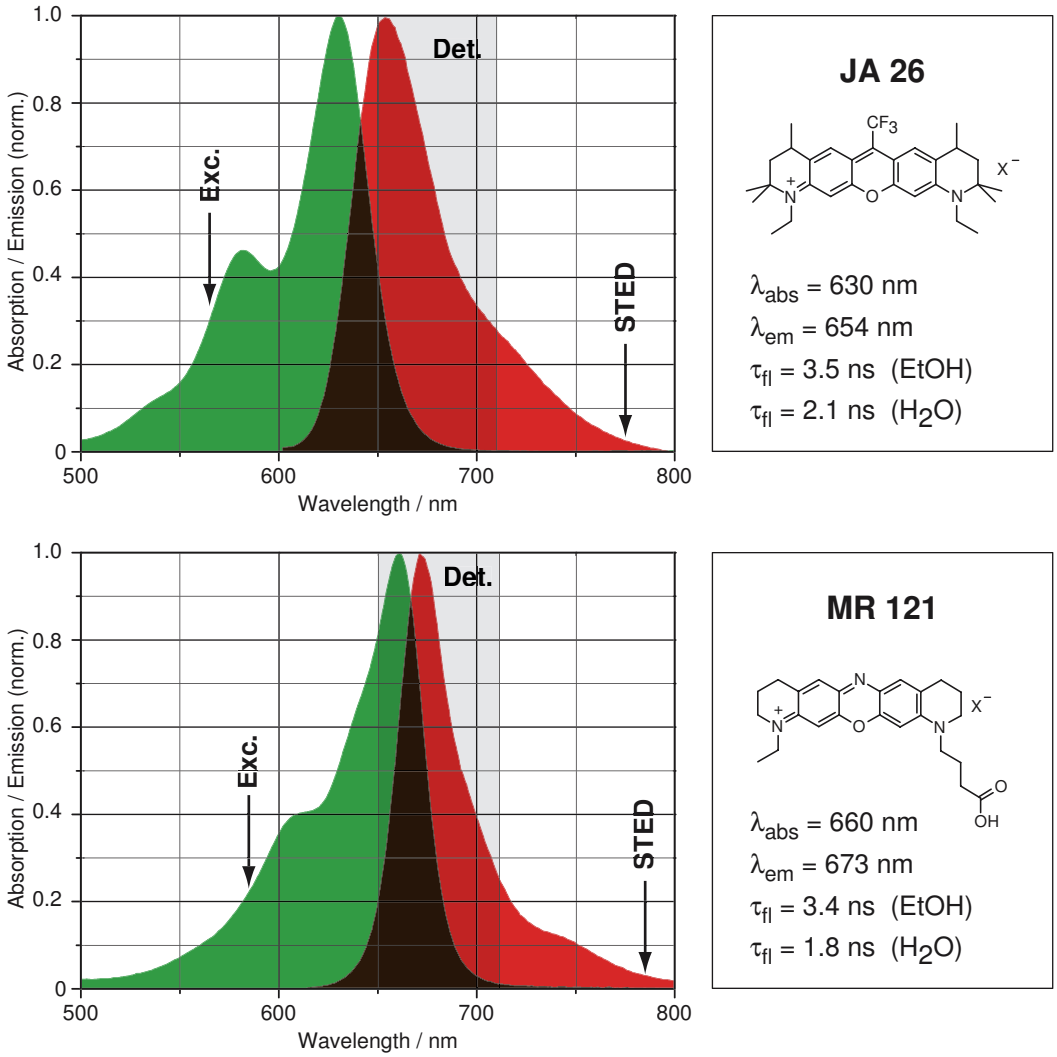

Fig. 2.2: Absorption and emission spectra (in ethanol) as well as selected photophysical properties of the fluorescent dyes JA 26 and MR 121 used in this thesis. The gray shaded wavelength region represents the detection range. In addition, the excitation and STED wavelengths are indicated.

Unlike described in the general outline of the setup, no phase retardation filter was used in this experiment, but an additional chopper wheel was inserted into the STED beam to interrupt the laser at a rate of 250 Hz. The Ti:Sapphire laser was tuned to 778 nm which yielded an excitation wavelength of 565 nm provided by the OPO. The experiment was carried out by laterally scanning a 5×5 μm^2 area of JA 26 molecules embedded in PVA. The pixel dwell time was 125 μs. The start of the fast scan axis (x) was synchronized to the phase of the chopper wheel to ensure that open and closed intervals of the STED beam coincided in all scanlines. Figure 2.3 shows an acquired image along with two bars arranged above the image which indicate the presence or absence of the excita-

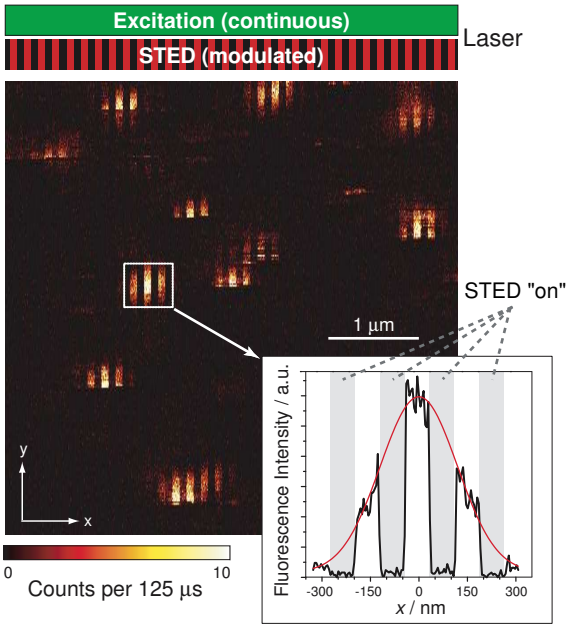

Fig. 2.3: Stimulated emission on single JA 26 molecules dispersed in a PVA matrix. While laterally scanning a $5 \times 5\ \mu\mathrm{m}^2$ area the STED beam was interrupted by a chopper wheel. The bars above the image indicate when the excitation and STED beams were open (green, red) and closed (black), respectively. The inset shows the vertically integrated fluorescence from a single molecule and demonstrates that virtually complete fluorescence suppression can be achieved on a single molecule. The Gaussian shaped envelope of the trace represents the lateral FWHM of the PSF (281 nm).

tion and the STED laser light, respectively. The image shows bright spots due to the single fluorophores disrupted by dark stripes where the fluorescence drops to almost background level. As can be confirmed by comparison with the indicator above, these dark regions correspond to intervals when the STED beam was *open*. This impressively demonstrates that stimulated emission depletion can in fact entirely suppress the fluorescence even on single fluorescent molecules in a reversible manner. Apart from the fluorescence suppression induced by STED, the spots also show spontaneous blinking and instantaneous bleaching as hallmarks of single emitters. The envelopes of the spots feature a FWHM of 281 nm which is exclusively determined by the lateral width of the PSF. As for the suitability of the setup with regard to single-molecule experiments, a satisfactory signal-to-background ratio of 100–150 is derived from Fig. 2.3.

2.3 STED Efficiency as a Single-Molecule Criterion

Commonly, the aforementioned characteristics of blinking and binary photobleaching are taken as sufficient evidence for the presence of single isolated molecules. However, because the presence of a single molecule is crucial for some applications [85], further indication is desirable. As is shown in this section, the STED efficiency may provide such information if appropriate polarization conditions are used.

To outline the underlying idea, it is advantageous to quantify the STED effect in terms of the fluorescence reduction factor η.[2] Formally, the fluorescence reduction factor is

[2]The more intuitive STED efficiency $\varepsilon = 1 - \eta$ is often used in qualitative discussions but unnecessarily

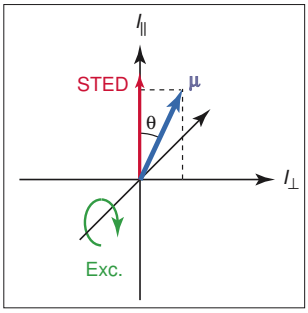

Fig. 2.4: Polarization conditions for discrimination between single and multiple molecules.

defined as the ratio of the fluorescence intensities in the presence (F_{STED}) and absence (F_0) of the STED light:

$$\eta = \frac{F_{\mathrm{STED}}}{F_0}. \tag{2.1}$$

Given a circularly polarized excitation laser, the probability of exciting a molecule is independent of its orientation within the focal plane. The STED laser is assumed to be linearly polarized, and the fluorescence light is detected polarization resolved using two separate detectors for the s- and p-polarization (Fig. 2.4). Further, it is assumed that the transition dipoles of fluorescence and stimulated emission are colinear. Now, a molecule whose projection of the transition dipole $\boldsymbol{\mu}$ into the focal plane encloses an angle of θ with the polarization of the STED light contributes to the intensities in the detection channels according to

$$F_{||} = F_0 \cos^2\theta \quad \text{and} \quad F_{\perp} = F_0 \sin^2\theta \tag{2.2}$$

where $F_{||}$ and $F_{\perp}$ are the intensities in the detection channels parallel and perpendicular to the STED polarization, respectively. Likewise, the signal reduction in both channels due to STED is subject to a cosine-squared dependence, $\eta = \eta_0 \cos^2\theta$ where η_0 is the fluorescence reduction for a molecule whose dipole projection into the focal plane is oriented parallel to the STED polarization. The detected intensities in the presence of STED then become

$$F_{||,\mathrm{STED}} = \eta F_{||} = F_0 \eta_0 \cos^4\theta, \tag{2.3a}$$

$$F_{\perp,\mathrm{STED}} = \eta F_{\perp} = F_0 \eta_0 \sin^2\theta \cos^2\theta. \tag{2.3b}$$

Now, if several (say, N) molecules contribute to the total fluorescence signal their contributions have to be added up and the fluorescence reduction in the two channels is

complicates the equations here.

given by:

$$\eta_{||} = \frac{\sum_i^N F_{||,\mathrm{STED},i}}{\sum_i^N F_{||,i}} = \eta_0 \frac{\sum_i^N \cos^4\theta_i}{\sum_i^N \cos^2\theta_i}, \tag{2.4a}$$

$$\eta_{\perp} = \frac{\sum_i^N F_{\perp,\mathrm{STED},i}}{\sum_i^N F_{\perp,i}} = \eta_0 \frac{\sum_i^N \sin^2\theta_i \, \cos^2\theta_i}{\sum_i^N \sin^2\theta_i} \tag{2.4b}$$

where the summations extend over all contributing molecules. These equations show that $\eta_{||} = \eta_{\perp} = \eta_0 \cos^2\theta$ only if $N = 1$ or if the molecules are identically oriented by coincidence.

The prediction based on this derivation was verified in an experiment similar to the one described in Sect. 2.2. The setup was slightly modified to match the prerequisites of the analysis: Before the excitation beam was expanded, an achromatic quarterwave retardation plate (460–680 nm, B. Halle Nachfl. GmbH, Berlin, Germany) was inserted into the beam to produce circularly polarized light. In the detection path, the fluorescence was split with a polarizing beamsplitter cube and was focused into two multimode fibes ($d = 62.5$ μm, Thorlabs) coupled to two APDs (SPCM-AQR-13-FC, PerkinElmer Optoelectronics). As before, a 5×5 μm^2 area of single JA 26 molecules dispersed in PVA was scanned while the STED beam was intercepted by a chopper wheel. In order to be able to differentiate fluorescent spots originating from single as opposed to multiple molecules on the basis of their STED efficiencies, stimulated emission depletion was only performed well below the saturation level. Therefore, the peak STED intensity was reduced about 6fold ($I_{\mathrm{STED}} \approx 200$ MW cm^{-2}) to ensure STED efficiencies $< 70\%$. Figure 2.5 shows two exemplary scans (top, bottom) where the images collected by the two detectors are displayed separately (left, middle). The horizontal profile of the framed spots (shown as a 1D plot on the right of the figure) clearly reflect the two situations. While in example 1 the dips in the Gaussian shaped envelope are equally deep, in example 2 the intensity profile of channel 2 is significantly stronger modulated than that of channel 1. This clearly indicates the presence of more than one molecule in example 2. As a result, if the respective experimental circumstances permit the polarization conditions introduced here, the STED efficiencies provide further information for the occurence of single molecules without an additional measurement and without sacrificing part of the fluorescence signal. The only effort one has to take is to analyze the STED efficiencies.

[3] Throughout this thesis, laser intensities are reported as pulse peak intensities.

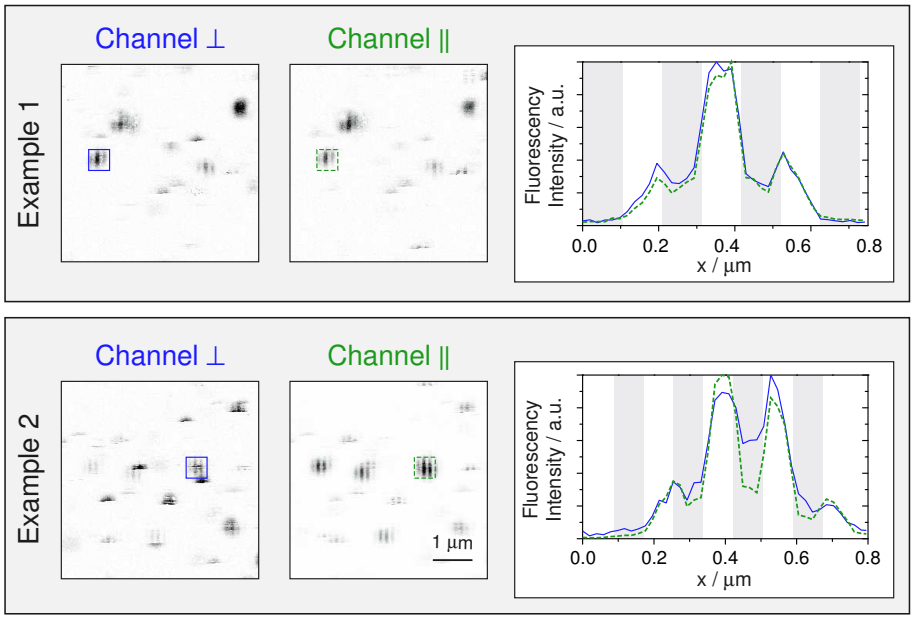

Fig. 2.5: Example of discrimination between fluorescent spots originating from a single and multiple molecules based on the analysis of the STED efficiencies. The top and bottom rows show two $5 \times 5\ \mu\mathrm{m}^2$ scans with polarization-resolved detection (left, middle). The trace on the right displays the vertically integrated intensity from the framed spots in the images aside where the solid line represents channel $\perp$ and the dotted line represents channel $||$. The unequally pronounced modulation in example 2 indicates the presence of more than one molecule. (Pixel dwell time: 2.5 ms, peak STED intensity[3] $\sim$200 MW cm^{-2})

2.4 Fluorescence Recovery after STED

As was pointed out in the introductory sections on molecular photophysics (Sect. 1.2), the number of different processes which may occur in organic fluorophores is manifold. While stimulated emission is a well-established process, the application of highly intense laser-light in the near-infrared may also induce transitions to states other than the ground state and may open up additional photobleaching pathways. While the ultimate proof of STED would be to directly detect the stimulated photons instead of the fluorescence reduction, this is impossible on a single-molecule basis because the gain in signal (one photon per pulse) is negligible compared to the shot noise of the laser. However, one should at least ascertain that the fluorescence depletion is reversible and occurs instantaneously. It is nontrivial to unambigously prove the immediate fluorescence recovery in bulk solution because, due to diffusion, fluorescence recovers within microseconds even if the dye in the focus has been bleached. In this respect, a STED experiment on a single immobilized molecule provides the maximal insight as it allows to track the fate of a single emitter over time.

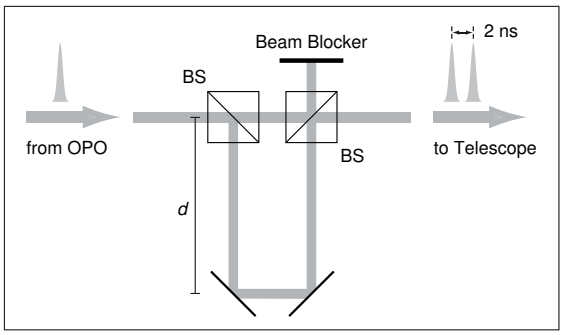

Fig. 2.6: Setup modification for the three-pulse experiment. The spacing d is chosen to be 30 cm which translates to a pulse delay of 2 ns.

First evidence for instantaneous fluorescence recovery and a proof of reversibility was already presented in the initial experiment depicted in Fig. 2.3. The image shows that many (>50) open-closed cycles of the STED beam can be applied with the molecules resuming their fluorescence each time. A closer look at the data reveals that the recovery occurs within one scan pixel and is therefore faster than the pixel dwell time of 125 μs. For a further analysis, the high time resolution of the time-correlated single-photon counting technique (TCSPC) was exploited along with a modified pulse sequence which adds an additional excitation pulse shortly after the STED pulse to probe whether the molecule can be excited after it had been depleted a few nanoseconds before.

This pulse sequence was experimentally realized by a modification of the setup which is depicted in Fig. 2.6. Before the STED beam was expanded in the telescope it was split into two equally intense beams using a 50:50 beamsplitter cube. One of the sub-beams was guided along an additional path of approx. 60 cm which translates into a delay of $\sim$2 ns. The beams were recombined with a second beamsplitter, were expanded and coupled into the microscope as outlined in Fig. 2.1. The delay of the STED pulses was adjusted such that the first of the two excitation pulses was followed by a STED pulse resulting in a sequence with

Exc. pulse — STED pulse — 2 ns delay — exc. pulse — 11 ns delay

as the repetition unit. The experiment was performed by acquiring lateral sections (10×10 μm^2) of single JA 26 molecules dispersed in a PVA film in TCSPC mode. In order to analyze the effect of the STED pulse in comparison to the excitation-only case, two images were acquired simultaneously by repeating each scanline with alternating (open/ closed) STED shutter positions. From these images, the TCSPC traces were extracted by integrating the signal from one fluorescent spot at a time.

Two examples of TCSPC traces obtained at different excitation intensities are shown in Fig. 2.7. In both graphs, the excitation-only trace is shown as a dotted line while the excitation–STED–excitation measurement (on the same molecule) is shown as a solid line. In the example a), the initial excitation due to the first excitation pulse is seen at $t = 8.5$ ns which is followed by the beginning of a monoexponential fluorescence decay.

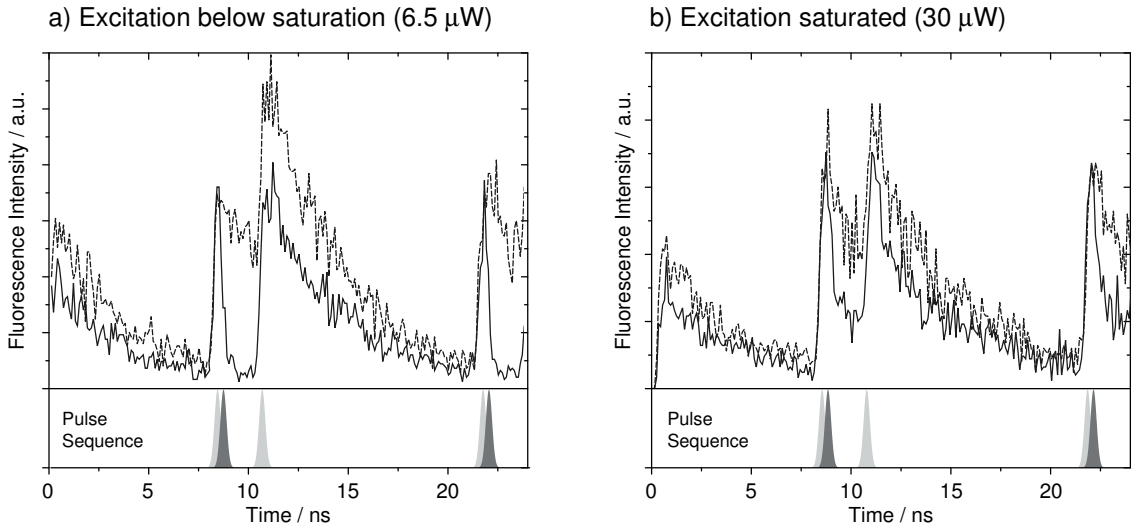

Fig. 2.7: Results of the three-pulse experiment. TCSPC traces of a single JA 26 molecules embedded in a PVA film in the presence (dotted lines) and absence (solid lines) of the STED pulse. a) Excitation power $6.5\ \mu$W, b) excitation power $30\ \mu$W. The average STED power was 3.0 mW in both experiments, excitation pulse length: 12 ps, STED pulse length: 15 ps (FWHM).

At $t = 10.5$ ns, the second excitation pulse induces a further rise with an amplitude equal to the first pulse. This indicates that the excitation intensity is well below the saturation level. In the respective TCSPC histogram with the STED pulse present, the initial rise due to the first excitation pulse is followed by a STED-induced drop of the intensity to almost the background level shortly after. The second excitation pulse, however, gives rise to the same amplitude as is in the case without STED. While these curves suggest at first glance that indeed a molecule is ready for excitation within 2 ns from the precedent STED pulse it must be pointed out that this direct interpretation is not valid. The reason is that the TCSPC trace does not reflect the true chronological order of events because it is built up as a histogram by averaging over a large number of excitation-emission cyles. (In this regard, the TCSPC technique is suboptimal.) Instead, the analysis has to be based on the rise in amplitudes due to the first and the second excitation pulse. By examining the TCSPC histograms in Fig. 2.7a), one finds that the same rise in amplitude of the fluorescence decay curve is caused by each excitation pulse, independent of whether the STED pulse is present or not. This indicates that no dark states with a lifetime of multiple cycles (i.e. $\gg$15 ns) can be populated by the STED pulse because, in this case, a reduced amplitude of the fluorescence decay would be expected if the STED pulse is present.

Further, example b) shows the same experiment repeated with the excitation saturated as is apparent from the identical fluorescence decay amplitudes reached after the first and the second excitation pulse. However, these equal amplitudes also indicate that no substantial builtup of a dark state with a lifetime of a few nanoseconds takes places which

would inevitably entail a reduced amplitude after the second pulse compared to the first.

In summary, while the three-pulse measurement presented here is probably not sensitive enough to disclose transitions to dark states with low transition probabilities, it excludes the formation of nanosecond-lived dark states as the major source of fluorescence depletion. Therefore, it is to be assumed that stimulated emission is the main process upon irradiation of electronically excited JA 26 molecules with near-infrared light.

2.5 PSF Characterization with Single Molecules

As the resolutions of STED microscopes have been dramatically improved recently [76], the need for ever smaller point-like objects has emerged to be able to characterize the instruments' performance. While, in conventional optical microscopes, the scattering of nanometer-sized gold particles (which are readily available) can be used to sample the point-spread function, this is not possible in STED microscopes as STED relies on the intrinsic photophysical properties of organic fluorophores, namely the ability to undergo stimulated emission. Therefore, fluorophore-labeled polystyrene beads have been commonly used which, however, become difficult to handle at sizes below $\sim$40 nm because of aggregation. Of course, imaging single fluorescent molecules would be the ideal point-like probe to assess the performance of a STED microscope. In a project closely related to this thesis, single molecules were first used to sample the effective PSF and thereby to characterize the resolution of a STED microscope [29].

The setup used was similar to the one depicted in Fig. 2.1 with the notable difference that pulsed diode lasers instead of a Ti:Sapphire and an OPO were used for excitation and stimulated emission depletion. While excitation was performed with a picosecond diode laser (LDH-635, PicoQuant GmbH, Berlin, Germany) emitting pulses of 68 ps duration at 635 nm, stimulated emission was effected by a second picosecond-pulsed laser diode (LDH-780, PicoQuant GmbH) generating 303 ps pulses at 781 nm. To provide sufficient intensity for stimulated emission depletion, the STED laser diode was amplified about 8fold by using a tapered amplifier (picoTA, Toptica Photonics GmbH, München, Germany) before it was coupled into the confocal microscope. As the diameter of the detection pinhole was 1.5 times the Airy disk, the lateral resolution of the microscope did not exceed that of a conventional microscope.

To achieve a lateral resolution enhancement, a semicircular phase retardation filter was placed into the collimated STED beam to introduce a phaseshift of π into one half of the beam. As a result, the focal intensity distribution of the STED beam (depicted in Fig. 2.8, right) features two laterally (x) displaced intensity maxima which are separated by a vertically extended zero-intensity node of 272 nm width (FWHM). (For a more detailed discussion on phase retardation filters see Chap. 4 and [86]). The excitation beam was focused to a diffraction-limited spot (depicted in Fig. 2.8, left) and was centered

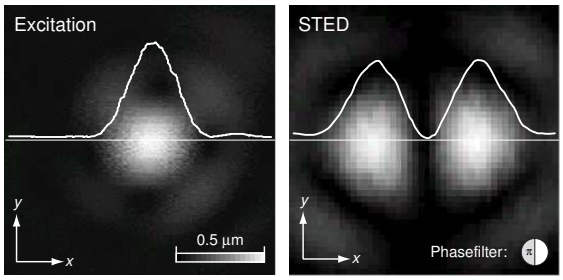

Fig. 2.8: Focal intensity distributions of the excitation and the STED focus, respectively. The shape of the STED PSF was attained by placing a semicircular phasefilter into the collimated STED beam which introduced a π-phaseshift into half of the beam. The intensity distributions were sampled with 150 nm gold beads in reflectance mode.

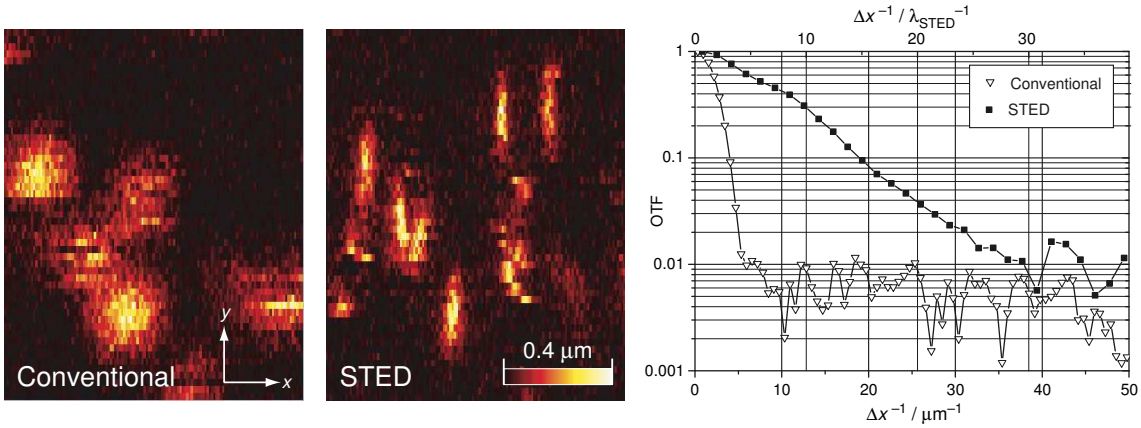

Fig. 2.9: Single molecules as point-like probes for PSF characterization [29]. Compared to the conventional image the fluorescence spots in the STED image are squeezed about 5fold in the x direction due to fluorescence depletion. Fourier transformation of the fluorescence spots yields the optical transfer function (OTF) which reveals a 6fold gain in spatial bandwidth. STED peak intensity: 450 MW cm^{-2}. *(Data by courtesy of Dr. Volker Westphal, Göttingen.)*

between the STED intensity maxima (Fig. 2.8, right).

To characterize the resolution of the STED microscope, lateral (xy) scans of single JA 26 molecules embedded in a PVA matrix were acquired with the STED laser switched on and off, respectively. In the conventional image (Fig. 2.9, left), the molecules show up as circular spots which reflect the lateral extension of the diffraction-limited excitation focus. On the contrary, in the STED image (taken at the same sample position), the spots are narrowed about 5-fold in the x direction which is due to pronounced fluorescence depletion in the outer focal regions. The increase in resolution is also reflected in the optical transfer function (OTF, see Sect. 1.3) which was computed by 2D Fourier transformation of the effective PSF which, in turn, was obtained by averaging the fluorescence signature of four individual molcules. Based on the individual noise levels, the resulting OTFs in the x direction for both the conventional and the STED microscope reveal a 6-fold increase in bandwidth (Fig. 2.9, right). Knowledge of the OTF can be used to perform linear deconvolution which further narrows the PSF down to 28$\pm$2 nm [29].

Even though the effective PSF is essentially homogenous across the scanned area, the STED image shows a nonuniform distribution of the spot widths in the x direction. The reason is that the fluorescent molecules are electric dipoles which are subject to photoselection as has been shown in Sect. 2.3. Therefore, the STED efficiency attained on an isolated molecule does not only depend on the local intensity but also on the orientation of its dipole with respect to the polarization of the STED light. As a result, each individual molecule shown in Fig. 2.9 experiences a different extent of STED saturation which translates into different degrees of resolution enhancement. This example teaches that the derivation of the effective PSF for the STED microscope as shown in Sect. 1.3.2 is only valid if a sufficient number of randomly oriented molecules is present in the focus such that photoselection effects cancel out. As the effective PSF is scaled down and, concurrently, the number of fluorescent molecules in the focus decreases, the photoselection effect becomes increasingly important and must be taken into account.

Finally, it should be noted that, in a similar experiment, a (less pronounced) resolution enhancement by a factor of $\sim$2 was achieved in both lateral directions and was characterized using single molecules [87].

Chapter 3

Single-Molecule Cross Section Measurements

3.1 Introduction

The strength of interaction between a photon and a molecule — whether absorption, stimulated emission or scattering — is described in terms of the respective optical cross section σ which can be intuively interpreted as the molecule's photon caption area. Being a fundamental parameter in the spectroscopic characterization of (fluorescent) dyes, optical cross sections are of interest from a viewpoint of basic research, but their quantitative knowledge is needed in applied fields such as laser design as well.

To calculate optical cross sections from first principles, a link between the observable cross section and the quantum mechanical description of a light induced transition can be established in terms of the Einstein coefficient of absorption or stimulated emission. For a given (single) vibronic transition $|\mathrm{i}\rangle \rightarrow |\mathrm{f}\rangle$, the Einstein coefficient is related to the cross section $\sigma(\nu)$ by [44]

$$B_{\mathrm{if}} = \frac{c_0}{hn} \int \frac{\sigma(\nu)}{\nu} \, \mathrm{d}\nu, \tag{3.1}$$

where c_0 is the vacuum speed of light, h is Planck's constant, n is the refractive index, $\nu = c_0/\lambda_0$ is the optical frequency and the integration extends over the full vibronic band. Given the validity of the Born-Oppenheimer approximation, the Einstein coefficient can also be expressed in terms of the wavefunctions of the involved states [44]:

$$B_{\mathrm{if}} = \frac{8\pi^2}{3h^2} \left|\langle\varphi_{\mathrm{i}}|\hat{\mu}_{\mathrm{el}}|\varphi_{\mathrm{f}}\rangle\right|^2 \left|\langle\Phi_{\mathrm{i}}|\Phi_{\mathrm{f}}\rangle\right|^2 . \tag{3.2}$$

Here, $|\varphi_{\mathrm{i}}\rangle$, $|\varphi_{\mathrm{f}}\rangle$, $|\Phi_{\mathrm{i}}\rangle$ and $|\Phi_{\mathrm{f}}\rangle$ denote the electronic and vibrational wavefunctions of the initial (i) and final (f) states, respectively, and $\hat{\mu}_{\mathrm{el}}$ is the electronic dipole moment operator. $\left|\langle\Phi_{\mathrm{i}}|\Phi_{\mathrm{f}}\rangle\right|^2$ is the Franck-Condon factor of the particular vibronic transition. These

equations may be expanded to describe the complete electronic transition (including the full vibronic substructure) by extending the integration in Eq. (3.1) over all vibrational bands and by summing over all vibronic transitions in Eq. (3.2). While *ab initio* calculations are principally feasible, they are impracticable for many quantitative studies due to the exceedingly complicated potential energy hypersurfaces involved. For this reason, calculations of cross sections [88] have not attained the required accuracy, despite recent progress in theoretical methods, particularly in density functional theory (DFT). Hence, for the time being, cross sections have to be determined experimentally.

Traditionally, stimulated emission cross sections are measured indirectly from absorption spectra (reciprocity method [89]) or from spontaneous emission spectra and the radiative lifetime (Strickler-Berg/ Füchtbauer-Ladenburg method [90, 91, 92]) where unit fluorescence quantum yield is commonly assumed. These methods have been extensively applied to laser media based on rare earth ions [93, 94], but the deviations in the reported cross sections are as large as a factor of three [95]. Cross section measurements based on the decrease (absorption) or increase (stimulated emission) of intensity [96, 97, 98] are reliable to within 10–20% but are not transferable to the single-molecule level because the signal loss or gain is negligible compared to the shot noise of the laser light.

The most straightforward way to determine the absorpion cross section on a single molecule is to derive the excitation rate at a given intensity from the fluorescence emission rate. However, this approach inevitably requires the knowledge of the fluorescence quantum yield of the particular molecule as well as the detection efficiency of the setup. From the absorption cross section, the stimulated emission cross section can be inferred by use of the reciprocity principle which exploits the mirror symmetry of the absorption and emission spectra.

However, stimulated emission cross sections of single fluorescent molecules can be determined even if the fluorescence quantum yield and the detection efficiency are unknown, as is shown in this chapter. In its simplest implementation, the method only requires a fluorescence intensity measurement at a single STED laser intensity in addition to a reference measurement in the absence of stimulated emission. However, to achieve better statistical accuracy, the residual fluorescence is measured as the molecule is exposed to increasing intensities of the STED laser beam. As these curves show a nearly exponential decrease in fluorescence (eventually reaching the background level), they are interchangeably referred to as *fluorescence depletion curves* or *STED saturation curves*. These curves are analyzed using the photokinetic models discussed next.

3.2 Photokinetic Models

The photokinetic models discussed in this chapter and used for the analysis of the measured STED saturation curves contain some simplifications which are to be discussed at

the beginning. First, all models imply that the molecule has been excited and is in its fluorescent state initially, i.e. the modelling only describes the processes after excitation has already taken place. In doing so, it should be realized that any effects that are sensitive to the temporal shape and overlap of the pulses cannot be adequately described. It is further assumed that both the excitation and the STED foci are aligned on top of each other and that the lateral part of the focal intensity distributions can be adequately described by a Gaussian function:

$$I(r,t) = I(0,t)\,\exp\left(-2r^2/w^2\right) \tag{3.3}$$

where w is the Gaussian width at which the intensity has dropped to e^{-2} of the peak value. It is related to the full-width at half-maximum according to $\mathrm{FWHM} = \sqrt{2\ln 2}\,w$. As the intensity is not directly measurable, it has to be expressed in terms of the time-averaged laser power, $\bar{P}$. To do so, the intensity $I(r,t)$ is expressed as a function of the instantaneous power $P(t)$ which is readily derived from the fact that, at each instant t, $P(t)$ is given by the integral of the intensity over the focal plane, $P(t) = 2\pi \int I(r,t)\,r\,\mathrm{d}r$. Carrying out the integration with Eq. (3.3) inserted for $I(r,t)$ one finds that $I(0,t) = 2P(t)/\pi w^2$ and, as a result,

$$I(r,t) = \frac{2}{\pi w^2} P(t)\,\exp\left(-2r^2/w^2\right). \tag{3.4}$$

In the derivations of the photokinetic models below, the temporal shape of the pulses is assumed to be either Gaussian or rectangular. For the latter case, $P(t)$ is simply given by dividing the pulse energy E_{Pulse} by the pulse length τ where the pulse energy in turn is given by the average power $\bar{P}$ divided by the repetition frequency f of the laser:

$$P(t) = \frac{E_{\mathrm{Pulse}}}{\tau} = \frac{\bar{P}}{\tau\, f}, \qquad 0 < t < \tau. \tag{3.5}$$

Taking into account that the average power is measured at the entrance of the objective lens which has a limited (and wavelength-dependent) transmission of $T(\lambda)$, one arrives at:

$$I_{\mathrm{Rect}}(r,t) = \left(\frac{2}{\pi}\right) \frac{T(\lambda)\,\bar{P}}{w^2\,\tau\,f}\,\exp\left(-2r^2/w^2\right) \tag{3.6}$$

The corresponding formula for pulses with a Gaussian temporal shape is obtained by temporal integration over the instantaneous power $P(t) = P_0 \exp\left(-2t^2/\tau^2\right)$ of a single pulse which equals the pulse energy $E_{\mathrm{pulse}} = \int P(t)\,\mathrm{d}t$. Carrying out the integration and inserting the result into Eq. (3.4) yields:

$$I_{\mathrm{Gauss}}(r,t) = \left(\frac{2}{\pi}\right)^{3/2} \frac{T(\lambda)\,\bar{P}}{w^2\,\tau\,f} \exp\left(-2t^2/\tau^2\right) \exp\left(-2r^2/w^2\right) \tag{3.7}$$

where, again, $E_{\mathrm{Pulse}} = \bar{P}/f$ has been used and the objective lens transmission $T(\lambda)$ has been introduced. Finally, for use in the photokinetic models described below, it is convenient to express the intensities in units of [photons / (s $\times$ m^2)] rather than in [W / (s $\times$ m^2)] which is done by dividing Eqs. (3.6) and (3.7) by the photon energy hc/λ. By denoting the focal photon fluxes with $h(r,t)$, one arrives at the following expressions for rectangular and Gaussian shaped pulses:

$$h_{\mathrm{rect}}(r,t) = \left(\frac{2}{\pi}\right) \frac{\lambda\, T(\lambda)\, \bar{P}}{h\, c\, w^2\, \tau\, f}\, \exp\left(-2r^2/w^2\right) \tag{3.8a}$$

and

$$h_{\mathrm{Gauss}}(r,t) = \left(\frac{2}{\pi}\right)^{3/2} \frac{\lambda\, T(\lambda)\, \bar{P}}{h\, c\, w^2\, \tau\, f}\, \exp\left(-2t^2/\tau^2\right)\, \exp\left(-2r^2/w^2\right). \tag{3.8b}$$

3.2.1 Two-Level Model

In the introductory chapter, a four-level model to describe the processes involved in a STED experiment has already been introduced [see Fig. 1.2 and Eqs. (1.3)]. While that model offers a lot of flexibility, it also entails quite involved solutions of the rate equations. For the purpose of determining stimulated emission cross sections, though, the four-level model can be significantly simplified. To begin with, the dynamics of the excitation process are mostly irrelevant to stimulated emission, so it is assumed that the fluorescent molecule is in its excited state S_1 initially (expressed as $P_1(t=0) = 1$ where $P_1(t)$ denotes the probability of finding the molecule in the S_1 state at time t). Furthermore, the rates of vibrational relaxation k_{vib} are on the order of 2×10^{12} s^{-1} whereas the rate of stimulated emission is typically only in the range of 10^{10}–10^{11} s^{-1}, unless ultrashort (i.e. femtosecond) pulses are used. Under these circumstances, hardly any population is built up in the transient state S_0^*, which can therefore be disregarded along with the reexcitation ($S_1 \leftarrow S_0^*$) and vibrational decay ($S_0^* \rightarrow S_0$) transitions. As a result, only the two levels S_1 and S_0 remain which are interconnected by fluorescence (with rate constant k_{fl}) and by stimulated emission (with rate constant k_{STED}). These simplifications leading to the two-level model are also depicted in Fig. 3.1. Quantitatively, the dynamics of the excited state in this model are governed by the following rate equation:

$$\frac{\mathrm{d}P_1(t)}{\mathrm{d}t} = -\left(k_{\mathrm{fl}} + k_{\mathrm{STED}}\right) P_1(t) \tag{3.9}$$

where $k_{\mathrm{STED}} = \sigma_{\mathrm{STED}} h_{\mathrm{STED}}$ is the intensity-dependent STED rate with h_{STED} denoting the photon flux in the STED focus measured in [photons / (s $\times$ m^2)]. If one assumes (as a further simplification) that the STED pulses can be modelled as rectangular in time, i.e. the STED rate being constant during the STED pulse, the rate equation is easily solved

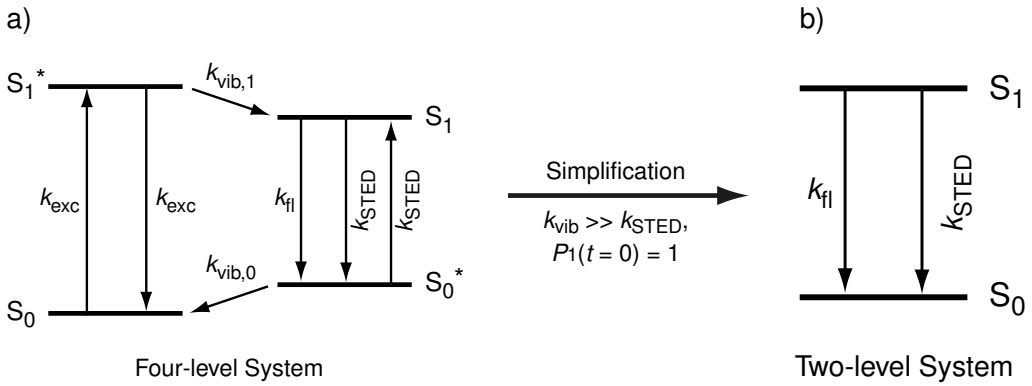

Fig. 3.1: Simplification of the four-level model (a) to a two-level model (b) by neglecting the excitation processes and assuming that $k_{\mathrm{vib}} \gg k_{\mathrm{STED}}$. As a result, only the fluorescence and stimulated emission transitions are considered.

by piecewise integration:

$$P_1(t) \;=\; \begin{cases} P_1(0)\exp\left[-(k_{\mathrm{fl}}+k_{\mathrm{STED}})t\right] & \text{for} \quad 0 \le t \le \tau \\ \\ P_1(\tau)\exp\left[-k_{\mathrm{fl}}(t-\tau)\right] & \text{for} \quad t > \tau \end{cases} \tag{3.10}$$

where τ is the STED pulse duration. Under consideration of the fluorescence quantum yield q_{fl}, the detection efficiency q_{det}, the sampling time Δt and the repetition rate f of the laser, the detected fluorescence is given by temporal integration:

$$\begin{aligned} F(h_{\mathrm{STED}}) \;&=\; q_{\mathrm{fl}}\, q_{\mathrm{det}}\, \Delta t\, f k_{\mathrm{fl}} \left[P_1(0) \int_0^{\tau} \exp\left[-(k_{\mathrm{fl}}+k_{\mathrm{STED}})t\right] \mathrm{d}t \right. \\ &\qquad \left. + P_1(\tau) \int_0^{\infty} \exp\left(-k_{\mathrm{fl}}t\right) \mathrm{d}t \right] . \end{aligned} \tag{3.11}$$

After evaluation of the integrals and normalization to $F(0)$, this provides the following expression for the fluorescence reduction factor:

$$\begin{aligned} \eta(h_{\mathrm{STED}}) \;&=\; \frac{F(h_{\mathrm{STED}})}{F(0)} \\ &=\; \frac{k_{\mathrm{fl}}}{k_{\mathrm{fl}}+k_{\mathrm{STED}}} + \left(1 - \frac{k_{\mathrm{fl}}}{k_{\mathrm{fl}}+k_{\mathrm{STED}}}\right) \exp\left[-(k_{\mathrm{fl}}+k_{\mathrm{STED}})\tau\right] . \end{aligned} \tag{3.12}$$

This result may be further simplified by recognizing that the fluorescence lifetime of an organic fluorophore is on the order of a nanosecond, that is, $k_{\mathrm{fl}} \approx 10^9\ \mathrm{s}^{-1}$ which is significantly smaller than k_{STED}. Thus, using $k_{\mathrm{fl}} \ll k_{\mathrm{STED}}$, Eq. (3.12) gives:

$$\eta(h_{\mathrm{STED}}) \approx \exp\left(-k_{\mathrm{STED}}\tau\right) = \exp\left(-\sigma_{\mathrm{STED}} h_{\mathrm{STED}} \tau\right) . \tag{3.13}$$

By solving this simple equation for $\sigma_{\mathrm{STED}} = -(h_{\mathrm{STED}}\tau)^{-1}\ln[\eta(h_{\mathrm{STED}})]$, it is seen that, from the measurement of the fluorescence depletion at a single STED intensity h_{STED}, the cross section can already be determined, as was mentioned in the introduction. For higher statistical accurary, it is advisable, though, to measure $\eta(h_{\mathrm{STED}})$ at various STED intensities.

In fact, the monoexponential behavior predicted by Eq. (3.13) is observed under proper experimental conditions, i.e. if the duration of the STED pulses is at least on the order of picoseconds and the fluorescent lifetime is on the nanosecond scale. However, some applications require the use of ultrashort STED pulses (e.g. to achieve a high time resolution) or of dyes with subnanosecond lifetimes. In those cases, deviations from the purely exponential behavior are expected because the transient state S_0^* cannot be ignored any more. In the following section, the S_0^* state is reintroduced into the model, and it is shown that, despite being cumbersome, the model can still be analyzed in an analytic fashion.

3.2.2 Three-Level Model

By reintroducing the previously ignored transient state S_0^*, the three-level model shown in Fig. 3.2 is obtained which accounts for two important aspects of STED which were previously neglected. One effect is the already mentioned reexcitation[1] due to the STED

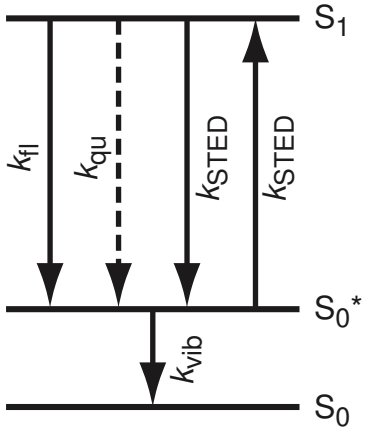

Fig. 3.2: Three-level model for stimulated emission. In addition to the two-level model of Fig. 3.1 reexcitation $S_1 \leftarrow S_0^*$ and vibrational relaxation $S_0^* \rightarrow S_0$ is considered.

pulse which, in fact, is inseparable from stimulated emission and is particularly relevant if the STED rate k_{STED} and the vibrational decay rate k_{vib} are on a similar scale. Unlike before, significant population is built up in the S_0^* state if $k_{\mathrm{STED}} \approx k_{\mathrm{vib}}$. Second, the

[1]The inclusion of reexcitation into a two-level model would lead to the erroneous prediction that no more than 50% of the excited molecules can be driven to the ground state because, at equal populations of the S_0 and S_1 states, stimulated emission and reexcitation balance out and no net change in population occurs.

three-level model takes into account that stimulated emission is carried out in the long-wavelength range of the fluorescence spectrum, such that the photon energy of the STED light only suffices to drive the molecules from the S_1 state into highly vibrationally excited levels of the ground state, which are collectively represented by S_0^*. These levels are depopulated by vibrational relaxation on a picosecond timescale which acts as an efficient drain of population for the $S_1 \leftrightarrow {S_0}^*$ system. As a result, (almost) complete fluorescence depletion can be achieved if the STED pulse is significantly longer than the time constant of vibrational relaxation.

In addition to the already discussed transitions of fluorescence, stimulated emission, reexcitation and vibrational decay, the model in Fig. 3.1 includes an additional quenching transition as a wild card for possible radiationless decay channels such as internal conversion, collisional quenching etc. However, without restricting the applicability of the model, the quenching rate k_{qu}, which collectively accounts for all these phenomena, can be implicitly included in k_{fl} and does not need to be accounted for explicitly in the rate equations. In fact, this approach accomodates the experimental implementation where, using time-correlated single-photon counting, the *excited state* lifetime $(k_{\mathrm{fl}} + k_{\mathrm{qu}})^{-1}$ instead of the *radiative* lifetime k_{fl} is measured. The rate equations of the three-level model now read:

$$\frac{\mathrm{d}P_0^*(t)}{\mathrm{d}t} = -\left(k_{\mathrm{STED}} + k_{\mathrm{vib}}\right) P_0^*(t) + \left(k_{\mathrm{fl}} + k_{\mathrm{STED}}\right) P_1(t) \tag{3.14a}$$

$$\frac{\mathrm{d}P_1(t)}{\mathrm{d}t} = k_{\mathrm{STED}} P_0^*(t) - \left(k_{\mathrm{fl}} + k_{\mathrm{STED}}\right) P_1(t) \tag{3.14b}$$

where $P_0^*(t)$ and $P_1(t)$ denote the probabilities of finding the molecule in the S_0^* and S_1 states, respectively. Again, it is assumed that the system is in its excited state S_1 initially. Under the assumption that the STED rate is constant (i.e. that the pulses are temporally rectangular in shape), this set of ODEs can be solved by diagonalization of the coefficient matrix. For $P_1(t)$ (which is of exclusive interest here) one obtains:

$$\begin{aligned} P_1(t) = P_1^\circ \Bigg(& \frac{k' + k_{\mathrm{fl}} - k_{\mathrm{vib}}}{2k'} \exp\left[-(2k_{\mathrm{STED}} + k_{\mathrm{fl}} + k_{\mathrm{vib}} + k')t/2\right] \\ & + \frac{k' - k_{\mathrm{fl}} + k_{\mathrm{vib}}}{2k'} \exp\left[-(2k_{\mathrm{STED}} + k_{\mathrm{fl}} + k_{\mathrm{vib}} - k')t/2\right] \Bigg) \end{aligned} \tag{3.15}$$

where the abbreviation

$$k' = \sqrt{(2k_{\mathrm{STED}} + k_{\mathrm{fl}})^2 + {k_{\mathrm{vib}}}^2 - 2k_{\mathrm{fl}}k_{\mathrm{vib}}} \tag{3.16}$$

has been introduced and P_1° denotes the probability of finding the molecule in the excited state initially (i.e. at the beginning of the integration interval, see below). As before, the total fluorescence is obtained by piecewise integration over $k_{\mathrm{fl}} P_1(t)$ during the two

intervals with STED ($0 \leq t \leq \tau$) and without STED ($t > \tau$). By normalizing the result to $F(0)$, the STED depletion factor is obtained as a function of the STED intensity (via $k_{\mathrm{STED}} = \sigma_{\mathrm{STED}} h_{\mathrm{STED}}$):

$$\begin{aligned}\eta(h_{\mathrm{STED}}) = & \\ & \frac{k_{\mathrm{STED}}\left(2k_{\mathrm{STED}} + 3k_{\mathrm{fl}} - k_{\mathrm{vib}} + k'\right)}{k'\left(2k_{\mathrm{STED}} + k_{\mathrm{fl}} + k_{\mathrm{vib}} + k'\right)} \exp\left[-\frac{\left(2k_{\mathrm{STED}} + k_{\mathrm{fl}} + k_{\mathrm{vib}} + k'\right)\tau}{2}\right] \\ - & \frac{k_{\mathrm{STED}}\left(2k_{\mathrm{STED}} + 3k_{\mathrm{fl}} - k_{\mathrm{vib}} - k'\right)}{k'\left(2k_{\mathrm{STED}} + k_{\mathrm{fl}} + k_{\mathrm{vib}} - k'\right)} \exp\left[-\frac{\left(2k_{\mathrm{STED}} + k_{\mathrm{fl}} + k_{\mathrm{vib}} - k'\right)\tau}{2}\right] \\ + & \frac{k_{\mathrm{fl}}\left(k_{\mathrm{STED}} + k_{\mathrm{vib}}\right)}{k_{\mathrm{vib}}\left(k_{\mathrm{STED}} + k_{\mathrm{fl}}\right)}\end{aligned} \tag{3.17}$$

While, at first glance, this result suggests a much more complex dependence of $\eta(h_{\mathrm{STED}})$ on the STED intensity, the same simple monoexponential decay behavior as in Eq. (3.13) can be derived when the previous assumptions are applied:

$$\eta(h_{\mathrm{STED}}) \approx \exp\left(-k_{\mathrm{STED}}\tau\right), \qquad \text{if} \quad k_{\mathrm{fl}} \ll k_{\mathrm{STED}} \ll k_{\mathrm{vib}}.$$

While it is reasonable that the two models converge to identical expressions under the same simplifying assumptions, it is important to assess the range of parameters for which they are valid. This is the subject of the following section.

3.2.3 Comparison and Evaluation of the Models

As has just been shown, the two photokinetic models converge to the same expression if the prerequisites $k_{\mathrm{fl}} \ll k_{\mathrm{STED}} \ll k_{\mathrm{vib}}$ are fulfilled. While the experimental conditions often justify these assumptions, under some circumstances they may be violated if e.g. dyes with short lifetimes ($\ll$1 ns) are used. In those cases, the models may provide deviating results as is demonstrated in Fig. 3.3. The graphs show a series of simulated fluorescence depletion curves $\eta(h_{\mathrm{STED}})$ obtained from Eqs. (3.12) and (3.17) for different pulse lengths (100 fs, left and 15 ps, right) and stimulated emission cross sections ($\sigma_{\mathrm{STED}} = 0.5 \times 10^{-16}$ cm^2, $\sigma_{\mathrm{STED}} = 2.0 \times 10^{-16}$ cm^2). The most striking failure of the two-level model occurs at short STED pulse lengths. While the three-level model predicts that the fluorescence asymptotically approaches a residual nonzero level as $k_{\mathrm{STED}} \to \infty$, according to the two-level model the fluorescence converges to zero. For longer pulses, the deviations between the models are less pronounced. The explanation for this discrepancy is the fact that reexcitation $\mathrm{S}_1 \leftarrow \mathrm{S}_0^*$ due to the STED pulse and vibrational relaxation in the ground state ($\mathrm{S}_0^* \to \mathrm{S}_0$) are competing processes. In fact, the vibrational relaxation

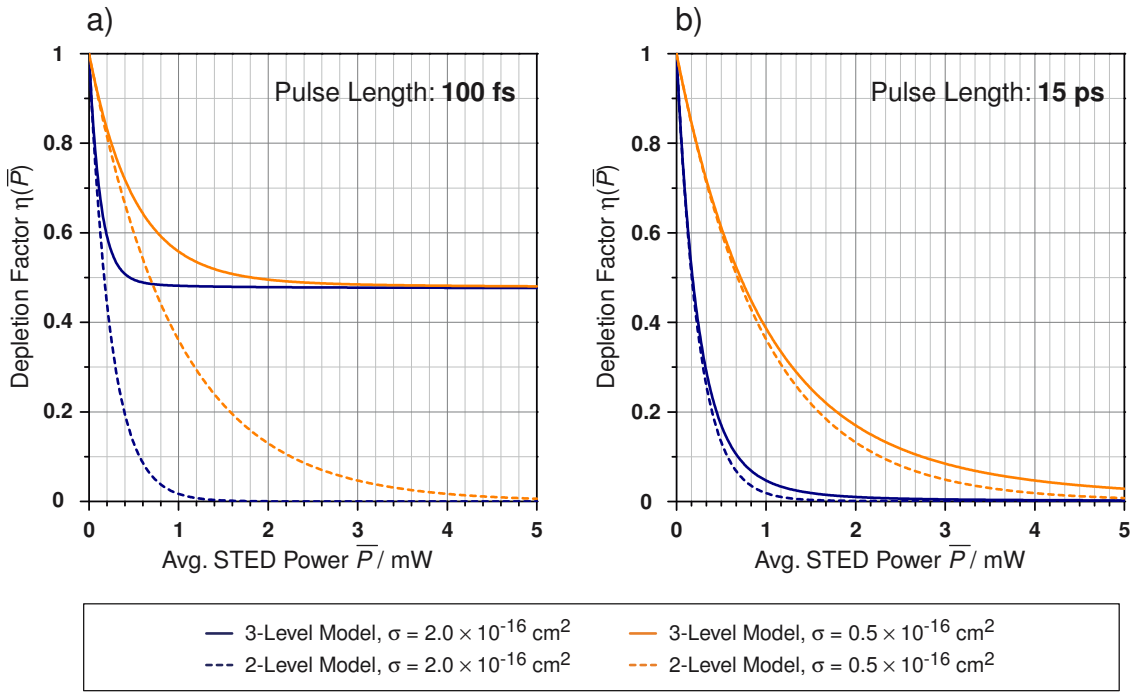

Fig. 3.3: Simulations of fluorescence depletion curves for two different pulse lengths ($\tau = 100$ fs, 10 ps) and stimulated emission cross sections ($\sigma_{\mathrm{STED}} = 0.5 \times 10^{-16}$ cm^2, 2.0×10^{-16} cm^2) according to the two-level (dotted lines) and three-level model (solid lines). Simulation parameters: $\lambda = 775$ nm, $\tau_{\mathrm{fl}} = 2$ ns, $\tau_{\mathrm{vib}} = 1$ ps, $w = 400$ nm, $f = 76$ MHz.

acts as a drain of population in the $\mathrm{S}_1 \leftrightarrow \mathrm{S}_0^*$ system while the STED pulses induces cycling between these states. If the STED pulse is long compared to ${k_{\mathrm{vib}}}^{-1}$, this drain may become complete and no fluorescence is emitted. However, if it is on a similar timescale as the vibrational decay, significant population is left in the $\mathrm{S}_1 \leftrightarrow \mathrm{S}_0^*$ system which gives rise to some (residual) fluorescence. As the two-level model only has channels that depopulate the fluorescent S_1 level, it cannot account for this phenomenon of competing processes. On the other hand, if the STED pulses are too long (e.g. on the order of the fluorescence lifetime), complete fluorescence depletion cannot be achieved because spontaneous emission starts to become an efficient competing process to stimulated emission. Fluorescence is emitted *during* the STED pulse thus lowering the STED efficiency.

In summary, the two-level model (and even its simplification to a monoexponential decay) provide mostly correct descriptions of the STED saturation curves for the regime where $k_{\mathrm{fl}} \ll k_{\mathrm{STED}} \ll k_{\mathrm{vib}}$. Thus, because of their simplicity, they are ideal for qualitative discussions and for a quick parameter estimation. For accurate quantitative measurements, though, the three-level model is more appropriate. Because its use as a model function for fitting purposes poses little additional computational burden, it is used exclusively to fit the measured depletion curves in Sect. 3.3.

Finally, it is instructive to calculate the level of residual fluorescence from Eq. (3.17) by taking the limit as $k_{\mathrm{STED}} \to \infty$:

$$\begin{aligned} \lim_{k_{\mathrm{STED}}\to\infty} \eta(\tau) &= \frac{k_{\mathrm{fl}}}{k_{\mathrm{vib}}}\left[1-\exp\left(-\frac{k_{\mathrm{vib}}\tau}{2}\right)\right]+\frac{1}{2}\exp\left(-\frac{k_{\mathrm{vib}}\tau}{2}\right) \\ &\approx \frac{1}{2}\exp\left(-\frac{k_{\mathrm{vib}}\tau}{2}\right) \end{aligned} \tag{3.18}$$

where $k_{\mathrm{vib}} \gg k_{\mathrm{fl}}$ has been used. From this equation, it is seen that the vibrational decay constant can in principle be determined by a simple measurement of the residual fluorescence at high STED intensities (provided short pulses are used). On a single molecule basis it may be difficult, though, to determine this relatively low saturation level with a sufficient signal-to-noise ratio in order to determine k_{vib} reliably.

3.3 Measurements

For the measurement of the single-molecule stimulated emission cross sections, the setup described in Sect. 2.1 was only slightly modified. To minimize photoselection effects, circularly polarized light was used for both excitation and STED which was generated by placing two achromatic quarterwave retardation plates (460–680 nm/ 500–900 nm, B. Halle Nachfl. GmbH, Berlin, Germany) into the laser beams. In addition, the size of the focal spots was increased by placing apertures with diameters of 3.6 mm and 4.7 mm into the expanded excitation and STED lasers, respectively. While this only marginally affected the lateral focal spot size, it provided significantly extended foci in the axial direction ($z_0 \approx 0.8\ \mu\mathrm{m}$ and $z_0 \approx 1.5\ \mu\mathrm{m}$ for excitation and STED, respectively) which reduced the sensitivity of the setup with respect to positioning the molecules into the focal plane and to drift in the z direction. Moreover, this measure rendered the longitudinally (z) polarized components of the focal field negligible. The excitation and STED wavelengths were 566 nm and 778 nm, respectively. The pulse lengths determined by autocorrelation were $\sim$13 ps for excitation and 14 ps for STED (FWHM). The laser power controllers were calibrated prior to the cross section measurements by recording the optical power at the entrance of the objective lens as a function of the LPC setting with a precision optical power meter (Model 1930 with detector 918-SL, Newport GmbH, Darmstadt, Germany).

As in the proof-of-concept experiments (Chap. 2), the cross section measurements were conducted using JA 26 molecules immobilized in a PVA matrix. For each recording, a single molecule was positioned in the laser focus by performing repeated linescans in the y direction while adjusting the x position until a fluorescence peak of maximal amplitude was encountered. Afterwards, consecutive line scans across the molecule were performed while the average STED power was ramped up line by line from zero to 3–10 mW (Fig. 3.4b). After each power ramp, the STED beam was interrupted to verify that

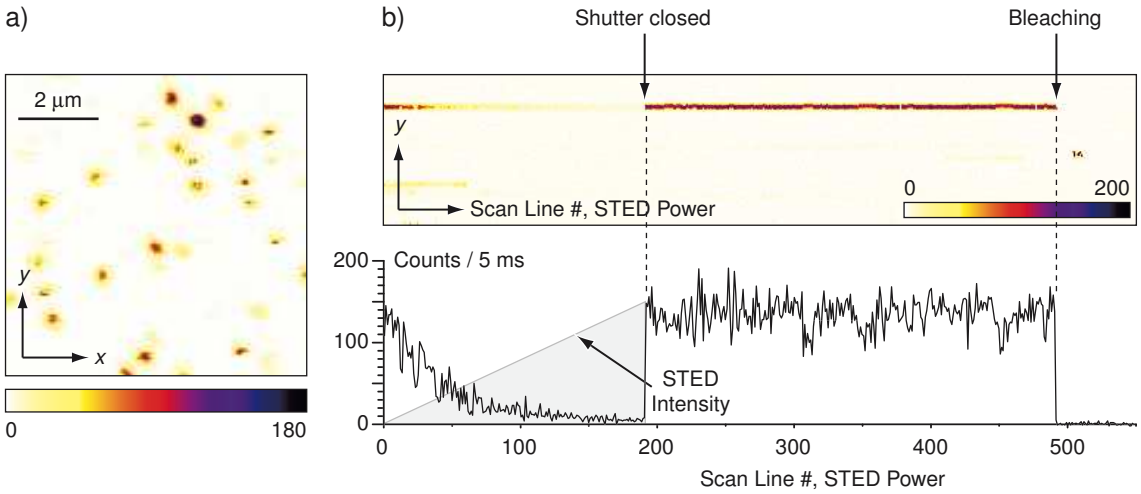

Fig. 3.4: a) Lateral section ($7.5 \times 7.5\ \mu\mathrm{m}^2$) of isolated JA 26 molecules dispersed in a PVA film. b) STED saturation trace of a single molecule. Top: Image of a single JA 26 molecule that is repeatedly scanned in the y direction (vertical axis) while the STED power is increased (horizontal axis). The fluorescence decreases until the shutter in the STED beam is closed. Then, the intensity recovers to its initial value until photobleaching occurs in a single step (indicative of a single molecule). Bottom: Fluorescence intensity trace of the center pixel of the molecule shown above. The gray shaded ramp indicates the applied STED intensity. Experimental parameters: $\bar{P}_{\mathrm{exc}} \approx 2\ \mu\mathrm{W}$, $\bar{P}_{\mathrm{STED}} = 0 \cdots \sim 8$ mW (the upper limit depends on the time of shutter closing), $\lambda_{\mathrm{exc}} = 566$ nm, $\lambda_{\mathrm{STED}} = 778$ nm.

the fluorescence recovered to its initial value. The scanning was continued until one-step photobleaching was observed.

To analyze the acquired fluorescence traces, it may be tempting to sum up the intensity of each fluorescent spot in the vertical (y) direction to achieve an optimal signal-to-noise ratio. However, such a procedure introduces a systematic error as it does not account for the fact that the STED intensity and thus the STED efficiency varies across the focal spot. If the STED depletion factor is determined from a trace added up in the y direction, an average of the following form results:

$$\eta(\bar{P}_{\mathrm{STED}}) = \frac{\int h_{\mathrm{exc}}(y)\, \eta\left[h_{\mathrm{STED}}(y)\right] \mathrm{d}y}{\int h_{\mathrm{exc}}(y) \mathrm{d}y} \tag{3.19}$$

where $h_{\mathrm{exc}}(y)$ and $h_{\mathrm{STED}}(y)$ denote the excitation and STED PSFs, respectively, $\bar{P}_{\mathrm{STED}}$ is the time-averaged STED power and the integration extends over the y axis in Fig. 3.4. Even in the simplest case when $\eta(h_{\mathrm{STED}})$ is a monoexponential decay function (see Sect. 3.2.1) and Gaussian shaped PSFs are assumed, the integrals cannot be solved analytically. The analysis of experimentally acquired $\eta(\bar{P}_{\mathrm{STED}})$ curves would therefore have to resort to an iterative approximation scheme.

This averaging in the analysis procedure can be avoided, though, if only the center pixel of each scan across the molecule is taken for evaluation. (In Fig. 3.4b, top, this corresponds to a horizontal line along the maximum intensity.) The STED PSF is assumed to be flat within this pixel such that no significant error is introduced. This scheme was adapted because the signal-to-noise ratio did not prove to be the limiting factor for accuracy.

The experimental fluorescence depletion curves were fitted using a C++ implementation of the Simplex algorithm [99] with Eq. (3.17) as the model function. In this equation, k_{STED} was replaced by $k_{\mathrm{STED}} = \sigma_{\mathrm{STED}}\, h_{\mathrm{STED}}$ where h_{STED} was calculated from the measured average power according to Eq. (3.8a). The following experimental parameters required for the fitting procedure were determined independently: STED wavelength $\lambda_{\mathrm{STED}} = 778$ nm, objective lens transmission $T(\lambda_{\mathrm{STED}}) = 0.71$, STED pulse length $\tau_{\mathrm{STED}} = 12$ ps, lateral width of the STED focus $w_{\mathrm{STED}} = 360$ nm, repetition rate $f = 75.26$ MHz and fluorescence lifetime $\tau_{\mathrm{fl}} = 3.96$ ns. The latter was determined by time-correlated single-photon counting. Finally, τ_{vib} only marginally affects the fitting result, and an estimated value of $\tau_{\mathrm{vib}} = 0.5$ ps was used which is typical for an organic fluorophore [45].

3.4 Results and Discussion

A total of 65 molecules were measured and fitted using this procedure. From the full dataset, eight representative curves were selected and are displayed Fig. 3.5 along with the respective cross sections determined by curve fitting. As can be seen from these examples, the variation in the cross sections is large with the majority of molecules yielding values between 0.5×10^{-16} cm^2 and 0.9×10^{-16} cm^2. In the full dataset, values between 0.3×10^{-16} cm^2 and 1.7×10^{-16} cm^2 were found, a histogram of which is shown in Fig. 3.6. These pronounced variations can be mainly attributed to photoselection which is effective for STED just as it is for excitation. This is illustrated in Fig. 3.7 which depicts a molecule whose transition dipole orientation is given by the azimuthal and polar angles ϕ and θ, respectively. Because the contribution of z polarized components in the microscope is negligible (as can be shown by diffraction theory), only the projection of the transition dipole into the focal plane is effective which is scaled by a factor of $\sin\theta$ compared to its absolute value. Unlike the ϕ dependence, which was experimentally excluded by the use of circular polarization, the $\sin\theta$ factor cannot be eliminated. To assess the absolute cross sectional values it would be desirable to determine the molecular orientations along with the fluorescence depletion curves. In fact, several schemes have been proposed to measure molecular orientations most of which are based on an analysis of the fluorescence pattern a molecule is emitting under special illuminations conditions [100] or when the molecule is slightly defocused [101]. However, these approaches are not

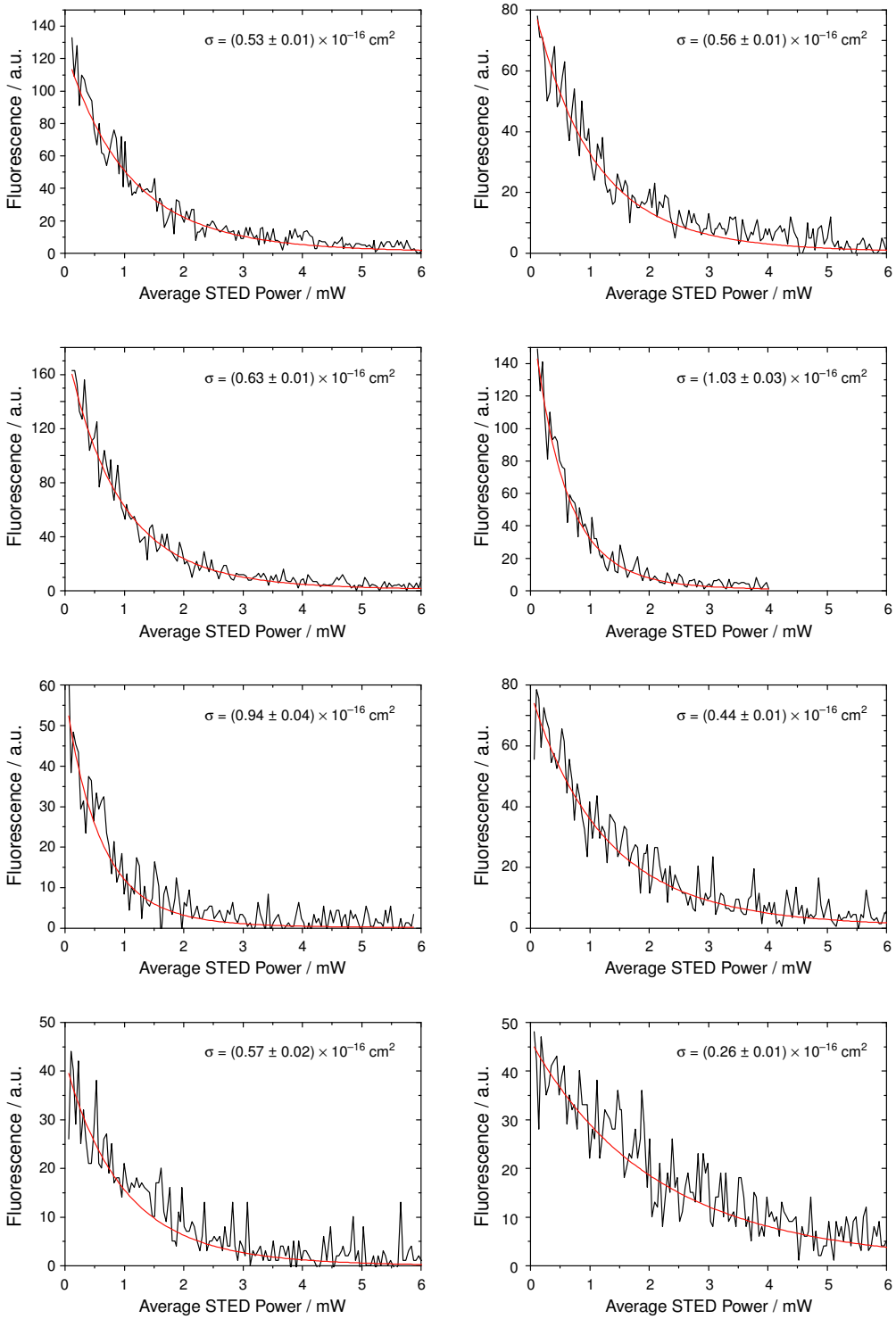

Fig. 3.5: Fluorescence depletion curves acquired on eight indivual molecules. The indicated stimulated emission cross section were determined by fitting the curves with the three-level model function, Eq. (3.17).

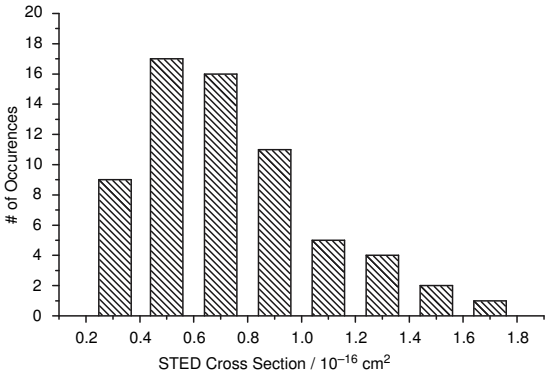

Fig. 3.6: Histogram of measured stimulated emission cross sections.

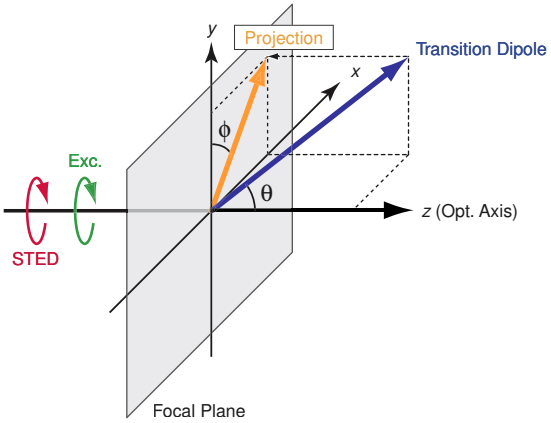

Fig. 3.7: Projection of a molecule's transition dipole into the focal plane. For circularly polarized excitation and STED light the effective transition dipole is scaled by $\sin\theta$.

feasible for the cross section determinations as they necessitate a separate measurement with a high signal-to-noise ratio demand. Thus, the available number of fluorescence photons, which is severely limited by photobleaching, would have to be shared among the two measurements which is unacceptable for the desired statistical accuracy. A more appropriate scheme based on a multidetector setup has been theoretically proposed [102] but is difficult to implement experimentally without loss of signal.

As a resort, to derive the absolute value of the stimulated emission cross section, it is conceivable to fit the histogram in Fig. 3.6 with a distribution function for the in-plane components which can be derived based on the assumption of randomly oriented molecules. While not even this assumption is necessarily realistic (because spin coating of the thin polymer film may introduce orientational bias), the manual selection and analysis of the single molecule traces strongly distorts the distribution. Furthermore, a global analysis disregards the possibility of individual variations in the stimulaed emission cross sections which may exist as a result of variations in the local environment. Therefore, a quantitative analysis of the histogram was omitted. Instead, the largest determined stimulated emission cross section of 1.7×10^{-16} cm^2 should be a good estimate of the average absolute value which is on the same order of magnitude as was found for a solution of fluorescein/ methanol (1.4×10^{-16} cm^2) in a cuvette-based experiment [49].

To verify the suitability of the model used for the cross section determination, the fluorescence depletion curves were also fitted using the mononexponential decay function [Eq. (3.13)] and by solving the rate equations of the three-level model [Eq. (3.14)] numerically using Gaussian pulses. Thus, the influence of the third level and of the pulse shaped can be evaluated. The fitting results for the eight curves shown in Fig. 3.5 are

shown in Table 3.1. From this data, it must be concluded that the two-level model is in fact an oversimplification if quantitative results are to be obtained. On average, the cross sections are underestimated by 15–20%. The comparison further shows that the neglect of the pulse shape introduces only a minor error ($\leq 5\%$) which is on the order of the statistical accuracy of the measurements. The latter was estimated to be within 10% by repeatedly fitting selected saturation curves with the parameters varied within their error ranges. These were taken from the manufacturer's specifications of the measurement equipment and/ or determined from multiple measurements of the quantity of interest.

It is worth noting that the presented method is not directly transferable to measure *absorption* cross sections in the same way. This can be demonstrated by setting up a two-level model for absorption in analogy to the one in Fig. 3.1. By solving the respective rate equation under the assumption of $k_{\mathrm{exc}} = \sigma_{\mathrm{abs}} h_{\mathrm{exc}} \gg k_{\mathrm{fl}}$, one can show that the detected fluorescence as a function of excitation intensity follows:

$$F(h_{\mathrm{exc}}) = q_{\mathrm{fl}}\, q_{\mathrm{det}}\, f\, \Delta t \left[1 - \exp\left(-\sigma_{\mathrm{abs}} h_{\mathrm{exc}} \tau\right)\right] \tag{3.20}$$

where σ_{abs} is the absorption cross section and h_{exc} is the excitation intensity in [photons/ (s$\times$m^2)]. The primary advantage in the determination of stimulated emission cross sections is that the preexponential factors cancel out as the fluorescence intensity is normalized to the reference value at zero STED intensity, $F(0)$. Therefore, accurate measurements are possible even though q_{fl} and q_{det} (which are difficult to measure on a single molecule) are unknown. If an equivalent normalization scheme is to be used to determine absorption cross sections, the fluorescence intensities have to be divided by the fluorescence saturation level [$F(h_{\mathrm{exc}} \rightarrow \infty)$] in order to cancel out q_{fl} and q_{det}. However, the determination of this saturation level, in particular on a single-molecule level, is severely challenged if not rendered impossible because of photobleaching. Even if the preexponential parameters in Eq. (3.20) are to be determined by curve fitting, the excitation intensity has to be increased until the onset of saturation is observed.

Although the absorption cross sections were not measured explicitly, it is worthwhile to derive their approximate values from Eq. (3.20) using estimates for the detection efficiency and the fluorescence quantum yield. As the excitation is subject to the same photoselection as is STED (provided the respective transition dipoles are colinear), a correlation between the absorption and stimulated emission cross sections is expected. Using $q_{\mathrm{det}} = 4.2\%$ (which was derived in Sect. 2.1) and $q_{\mathrm{fl}} = 1$ (as an assumption), the absorption cross sections shown in the right-most column of Table 3.1 are obtained. Despite the uncertainties in the calculation, the calculated values are surprisingly close to the measured stimulated emission cross sections. In most of the examples, both cross sections follow the same trend, but a few cases (e.g. #6 and #8 in Table 3.1) show striking differences. These may be explained in terms of local variations in the fluorescence quantum yield which do not influence the measurement of the stimulated emission cross sections

#	$\sigma_{\mathrm{STED}}/10^{-16}\ \mathrm{cm}^2$ (2-level model)	$\sigma_{\mathrm{STED}}/10^{-16}\ \mathrm{cm}^2$ (3-level, rect. pulses)	$\sigma_{\mathrm{STED}}/10^{-16}\ \mathrm{cm}^2$ (3-level, Gauss. pulses)	$\sigma_{\mathrm{abs}}/10^{-16}\ \mathrm{cm}^2$
1	0.44	0.53	0.50	0.81
2	0.46	0.56	0.53	0.59
3	0.52	0.63	0.60	0.88
4	0.84	1.03	0.97	0.58
5	0.80	0.94	0.90	1.07
6	0.38	0.44	0.42	1.49
7	0.49	0.57	0.55	0.70
8	0.23	0.26	0.25	1.11

Table 3.1: Stimulated emission cross sections determined from the fluorescence depletion curves in Fig. 3.5 using the simplified 2-level model function [Eq. (3.13)], the 3-level model function [Eq. (3.17)] and the numerical solution of the rate equations (3.14) using Gaussian pulses. For comparison, the respective estimated absorption cross sections are shown additionally.

but do affect the absorption cross section measurements (which are essentially intensity measurements). On the other hand, the cases of gross mismatch may also be explained in terms of multiple agglomerated fluorophores which were occasionally encountered in the samples and were sometimes identified by their stepwise bleaching behavior. Unfortunately, in many cases, the origin of mismatch cannot be assigned unambigously.

Chapter 4

Fluctuation Spectroscopy in Reduced Volumes

4.1 Introduction

The today's availability of optical microscopes with single-molecule sensitivity has paved the way for a whole new class of spectroscopic methods collectively referred to as *fluorescence fluctuation spectroscopy* (FFS). All of its variants are based on the registration of the fluorescence emitted by a single or, at most, a few molecules and by extracting information from the analysis of the intensity fluctuations which result from diffusion in and out of the detection volume, from photophysical processes and from chemical reactions. These kinds of analyses have remained unfeasible in the "pre-single-molecule era" because the fluctuations on which these methods are fundamentally based cancel out in any bulk measurement.

The earliest of the fluctuation methods and thereby the parent technique is fluorescence correlation spectroscopy (FCS) whose concept dates back to 1972 when *Elson* and *Madge* derived the theory [9, 103] and presented the first experimental implementation [104]. However, because of the low sensitivity of the detectors, the relatively large detection volumes (compared to todays standards) and the noisy laser sources, fluctuations were difficult to observe, and exceedingly long collection times of up to 24 hours were required. Needless to say that, initially, FCS did not find a dedicated following. The situation changed remarkably, though, when avalanche photodiodes (APD), confocal microscopes and digital hardware correlators became commercially available in the 1990s and, since then, FCS has become an easy-to-use and reliable technique [11, 12, 105]. Its attractiveness is based on the fact that multiple information are obtained in a single measurement while, at the same time, extremely low amounts of material are required. Because it is also well suited for automatization, FCS is not only used for photophysical studies in basic research but also in commercial applications such as drug discovery and

high-throughput screening (HTS) [17, 18]. It is therefore the fluctuation method most widely applied today.

The (auto)correlation approach employed in FCS characterizes the duration of fluorescence emission due to each fluorophore. This duration may be limited by the molecule's diffusion out of the detection volume, or by transitions to (transient or permanent) non-emissive dark states. Hence, FCS is capable to provide information on the kinetics of the system under consideration and, if the focal geometry is known, on the absolute concentration of the fluorescent solute. In particular, the diffusion times extracted from the correlation curves are commonly used to monitor association/ dissociation reactions (e.g. receptor-ligand binding) in biomedical applications. However, for the diffusion times to be discriminated with confidence, a $\sim$2fold increase in diffusion time upon binding is required [106] (corresponding to a change in molecular weight by a factor of $\sim$8) which severely limits the number of feasible FCS applications. Unlike many of its sibling techniques developed later, FCS is unable to differentiate between (static) populations which differ only in their specific brightness. These limitations have at least partly been alleviated, though, with the introduction of (multicolor) cross correlation techniques [107] and higher-order correlation analysis [108, 109, 110].

Alternatively, the fluorescence fluctuations can be analyzed in terms of the photon counting histogram which is built up from the number of counts detected in time intervals of equal width. This approach has been initially proposed by *Qian* and *Elson* [110] and has been made popular by two independent groups as *fluorescence intensity distribution analysis* (FIDA) [13] and as *photon counting histogram analysis* (PCH) [14]. Because these histogram-based techniques allow to differentiate molecular populations based on their specific brightness, i.e. on the number of emitted photons per molecule and unit time, they are complementary to FCS. In fact, with the computational hardware available nowadays, it is possible to store each photon count along with its macroscopic arrival time (with respect to the beginning of the measurement) and the microscopic arrival time (with respect to the following laser pulse). From these data, both the FCS curve and the FIDA histogram can be generated which can be simultaneously analyzed in a single global fit to provide all parameters accessible by both methods.

4.2 FCS in Reduced Volumes

It has already been mentioned that fluorescence fluctuation methods require that only few molecules be present in the detection volume at a time to ensure fluctuations considerably above the background level. More precisely, the zero-lag ($\tau \rightarrow 0$) amplitude of the intensity correlation function approaches $1/N$ where N denotes the number of molecules in the detection volume (see Sect. 4.3.1). While this relationship provides the basis for absolute concentration measurements, it also points out the concentration limitation of FCS.

Typically, at most ten molecules in the detection volume are tolerated which, at a detection volume of 0.2 fL (1 fL = 10^{-15} L) in a confocal setup, translates to a concentration not exceeding a few tens of nM. In many experiments, even lower concentrations are used to observe truely isolated molecules. While, in artificial environments, the concentration limit is not commonly a problem, this is different when weak interactions are to be studied as is the case in many biological systems. This may be illustrated as follows. Suppose a prototype association/ dissociation reaction of two species A and B that can form a weak complex:

$$\mathrm{AB} \rightleftharpoons \mathrm{A} + \mathrm{B}.$$

The dissociation constant of this reaction is given by $K_\mathrm{D} = [\mathrm{A}]\,[\mathrm{B}]/[\mathrm{AB}]$. Assume that A is fluorescently marked and that both A and AB are to be detected simultaneously. Assume further that A and B are present at a concentration of 10 nM and that $K_\mathrm{D} = 1\ \mu$M. Then, from the definition of the dissociation constant, it is easily calculated that $[\mathrm{AB}] = 0.1$ nM which is a factor of 100 less than $[\mathrm{A}]$. However, as has been shown both experimentally and by simulations [106], the fraction of AB should not fall below 0.5 if the two components are to be identified concurrently with statistical significance. Therefore, to achieve comparable concentrations for A and AB, the total concentration must be raised. To stick with the above example, if $[\mathrm{A}] = [\mathrm{B}] = 1\ \mu$M, the concentration of AB is 1 μM as well.

Yet another complication may arise if concurrent processes with similar characteristic times are to be discriminated by FCS which is possible only if the time constants differ by at least a factor of 1.5 [106]. Therefore, reactions with time constants close to the characteristic diffusion time can only be monitored if the diffusion time is changed artificially, e.g. by changing the size of the focal volume or the solvent's viscosity.

These problems have been recognized in the past few years and several suggestions have been made [111] to achieve reduced focal volumes in order i) to maintain the number of molecules in the detection volume small even at increased concentrations and ii) to reduce the diffusion times. The techniques proposed can be categorized into optical and mechanical approaches and combinations thereof, see Fig. 4.1. With the exception of the STED technique (Fig. 4.1c), these methods have in common that diffusion is constrained in at least one direction and that a surface is adjacent to the detection volume. Therefore, care has to be taken that adsorption/ desorption processes do not interfere with the process under investigation.

The first successful realization of a confined volume FCS experiment was reported by *Levene* and coworkers [112], who implemented an array of nanowells acting as zero-mode waveguides. Fluorescent solute molecules diffused into the wells from a drop of solution placed on top of the array. FCS curves acquired at 10 μM bulk concentration revealed an average of 0.1 molecules per waveguide, and the diffusion time could be re-

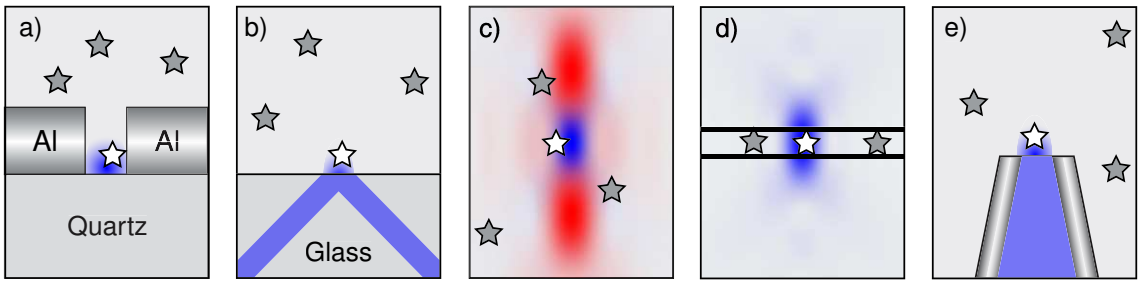

Fig. 4.1: Approaches to reduced detection volumes in FCS [111]. a) Micro-/nanowells with evanescent field excitation, b) total internal reflection (TIR) excitation, c) stimulated emission depletion (STED), d) microfluidic channels, e) near-field excitation through a tip.

duced by an order of magnitude. However, (uncorrelated) fluorescence background from the supernatant reduced the correlation amplitudes significantly. More recently, *Lieto* et al. published their implementation of a total internal reflection (TIR-)FCS setup [113] which they successfully used to study the receptor-ligand binding in a model membrane. The most recent advance was reported by *Foquet* et al. who managed to reduce the focal volume by a factor of ∼100 using submicrometer-sized fluidic channels [114].

4.3 FCS and FIDA Revisited

As was pointed out above, the theory that is underlying FCS has been developed long ago and has been reviewed in several monographs [34, 115] and extensive review articles on FCS [11, 12, 105]. Therefore, its derivation will only be outlined here as far as is necessary to motivate the combination of FCS with the STED technique. The same holds for the younger FIDA technique which is outlined only briefly to cover the aspects relevant to the studies presented in this thesis. More comprehensive derivations can be found in the literature [54, 116, 117].

The observable in any fluorescence fluctuation experiment is the detected fluorescence intensity $I(t)$ which gives a handle to the concentration of one or several fluorescent species. (The same formalism holds irrespective of whether the fluorescence signal is acquired as an analog photocurrent or as a digital photon count rate which is more common nowadays.) In the case of a single fluorescent solute, the total detected fluorescence is made up of the contributions from all volume elements within the detection volume V:

$$I(t) = \sigma_{\mathrm{abs}}\, q_{\mathrm{fl}}\, q_{\mathrm{det}} \int_V h_{\mathrm{exc}}(\boldsymbol{r})\, h_{\mathrm{det}}(\boldsymbol{r})\, C(\boldsymbol{r}, t)\, \mathrm{d}^3\boldsymbol{r}. \tag{4.1}$$

$C(\boldsymbol{r})$ is the local concentration at position $\boldsymbol{r} = (x, y, z)$, σ_{abs} denotes the absorption cross section of the fluorophore, q_{fl} is its fluorescence quantum yield and q_{det} is the detection

efficiency of the setup which is mainly determined by the solid angle the fluorescence is collected from, losses at the dichroic beamsplitters and bandpass filters and the detector quantum efficiency. For a typical confocal setup, q_{det} ranges from 2 to 5% (compare Sect. 2.1.1). Furthermore, $h_{\mathrm{exc}}(\boldsymbol{r})$ is the excitation point-spread function (PSF) and $h_{\mathrm{det}}(\boldsymbol{r})$ is the collection efficiency function, i.e. the (normalized) probability distribution function for detecting a photon that was emitted at location $\boldsymbol{r}$. Both distribution functions are usually combined into a single brightness function $p(\boldsymbol{r}) = h_{\mathrm{exc}}(\boldsymbol{r})\, h_{\mathrm{det}}(\boldsymbol{r})$ and, in FCS, are commonly approximated by a three-dimensional Gaussian function

$$p(\boldsymbol{r}) = p_0 \exp\left[-2(x^2+y^2)/{w_0}^2\right] \exp\left(-2z^2/{z_0}^2\right). \tag{4.2}$$

Here, w_0 and z_0 are the lateral and axial coordinates, respectively, where the intensity has dropped by a factor of e^{-2} compared to the peak value p_0.

4.3.1 Theory of Fluorescence Correlation Spectroscopy

As was mentioned in the introductory section, dynamical processes are analyzed in FCS in terms of the concentration fluctuations $\delta C(\boldsymbol{r},t) = C(\boldsymbol{r},t) - \langle C\rangle$ as these carry information on the dynamics of the system. Here, $\langle\,\rangle$ denotes an ensemble average and $C(\boldsymbol{r},t)$ is the local instantaneous concentration. The concentration fluctuations are reflected in fluctuations of the fluorescence intensity whose autocorrelation function is defined as

$$G(\tau) = \frac{\langle I(t)I(t+\tau)\rangle}{\langle I\rangle^2} = \frac{\langle \delta I(0)\delta I(\tau)\rangle}{\langle I\rangle^2} + 1 \tag{4.3}$$

where the definition $I(t) = \langle I(t)\rangle + \delta I(t)$ has been used. The last equality in Eq. (4.3) holds because the system is assumed to be stationary in time. Inserting Eq. (4.1) for $I(t)$, the intensity correlation function takes the following form:

$$\begin{aligned} G(\tau) &= \frac{\left\langle \int\int p(\boldsymbol{r})\, p(\boldsymbol{r'})\, \delta C(\boldsymbol{r},0)\, \delta C(\boldsymbol{r'},\tau)\, \mathrm{d}^3\boldsymbol{r}\, \mathrm{d}^3\boldsymbol{r'}\right\rangle}{\left\langle \int p(\boldsymbol{r})\, C(\boldsymbol{r},t)\, \mathrm{d}^3\boldsymbol{r}\right\rangle^2} + 1 \\ &= \frac{\int\int p(\boldsymbol{r})\, p(\boldsymbol{r'})\, g(\boldsymbol{r},\boldsymbol{r'},\tau)\, \mathrm{d}^3\boldsymbol{r}\, \mathrm{d}^3\boldsymbol{r'}}{\left(\langle C\rangle \int p(\boldsymbol{r})\, \mathrm{d}^3\boldsymbol{r}\right)^2} + 1 \end{aligned} \tag{4.4}$$

where $p(\boldsymbol{r}) = h_{\mathrm{exc}}(\boldsymbol{r})\, h_{\mathrm{det}}(\boldsymbol{r})$ has been used. In this expression,

$$g(\boldsymbol{r},\boldsymbol{r'},\tau) = \langle \delta C(\boldsymbol{r},t)\delta C(\boldsymbol{r'},t+\tau)\rangle = \langle \delta C(\boldsymbol{r},0)\delta C(\boldsymbol{r'},\tau)\rangle\,. \tag{4.5}$$

is the *concentration* autocorrelation function. The analysis presented here is restricted to the simplest case where only a single nonreactive fluorescent species freely diffuses in an open volume. The spatio-temporal evolution of the local concentration is therefore quantitatively described by the diffusion equation:

$$\frac{\partial \delta C(\boldsymbol{r},t)}{\partial t} = D\nabla^2 \delta C(\boldsymbol{r},t). \tag{4.6}$$

where D is the diffusion constant and ∇ is the Nabla operator. This equation is readily solved after Fourier transformation[1] into spatial frequency space to give:

$$\tilde{C}(\boldsymbol{q},t) = \tilde{C}(\boldsymbol{q},0)\ \mathrm{e}^{-D\,\boldsymbol{q}^2\,t} \tag{4.7}$$

where $\tilde{C}(\boldsymbol{q},t) = \mathcal{F}_{\boldsymbol{q}}\left[\delta C(\boldsymbol{r},t)\right]$ is the Fourier transformation of the concentration fluctuations with respect to the spatial coordinates $\boldsymbol{r}$. Using this result, the concentration correlation function Eq. (4.5) can now be further elaborated:

$$\begin{aligned} g(\boldsymbol{r},\boldsymbol{r'},\tau) &= \mathcal{F}^{-1}_{\boldsymbol{r'}}\left[\left\langle \delta C(\boldsymbol{r},0)\tilde{C}(\boldsymbol{q'},\tau)\right\rangle\right] \\ &= \mathcal{F}^{-1}_{\boldsymbol{r'}}\left[\left\langle \delta C(\boldsymbol{r},0)\tilde{C}(\boldsymbol{q'},0)\ \mathrm{e}^{-D\,\boldsymbol{q'}^2\,\tau}\right\rangle\right] \\ &= \mathcal{F}^{-1}_{\boldsymbol{r'}}\left\{\mathcal{F}_{\boldsymbol{q'}}\left[\langle \delta C(\boldsymbol{r},0)\delta C(\boldsymbol{r'},0)\rangle\right]\mathrm{e}^{-D\,\boldsymbol{q'}^2\,\tau}\right\} \end{aligned} \tag{4.8}$$

where the definitions of the Fourier transform $\mathcal{F}_{\boldsymbol{q'}}$ and its inverse $\mathcal{F}^{-1}_{\boldsymbol{r'}}$ have been applied. The interchange of Fourier transform and ensemble averaging is justified because both are linear independent operations. An expression for the time zero correlation amplitude $g(\boldsymbol{r},\boldsymbol{r'},0) = \langle \delta C(\boldsymbol{r},0)\delta C(\boldsymbol{r'},0)\rangle$ can be derived by considering that FCS is performed in highly dilute, that is, in ideal solutions. Thus,

1. solute molecules are noninteracting, i.e. correlations between molecules at different locations $\boldsymbol{r}$ and $\boldsymbol{r'}$ vanish, and

2. the concentration fluctuations are governed by Poissonian statistics for which the mean square deviation is equal to the mean.

Therefore,

$$g(\boldsymbol{r},\boldsymbol{r'},0) = \langle \delta C(\boldsymbol{r},0)\delta C(\boldsymbol{r'},\tau)\rangle = \langle C\rangle\,\delta(\boldsymbol{r}-\boldsymbol{r'}). \tag{4.9}$$

Plugging this expression into Eq. (4.8), the inner Fourier integral collapses and one arrives at:

$$\begin{aligned} g(\boldsymbol{r},\boldsymbol{r'},\tau) &= (2\pi)^{-3/2}\,\langle C\rangle\ \mathcal{F}^{-1}_{\boldsymbol{r'}}\left[\mathrm{e}^{i\boldsymbol{q'}\boldsymbol{r}}\,\mathrm{e}^{-D\,\boldsymbol{q'}^2\,\tau}\right] \\ &= (2\pi)^{-3}\,\langle C\rangle\int \mathrm{e}^{i\,\boldsymbol{q'}(\boldsymbol{r}-\boldsymbol{r'})}\mathrm{e}^{-D\,\boldsymbol{q'}^2\tau}\,\mathrm{d}^3\boldsymbol{q'} \end{aligned} \tag{4.10}$$

[1] In this derivation the symmetric definition of the Fourier transform is used: $\mathcal{F}_{\boldsymbol{q}}\left[C(\boldsymbol{r})\right] = (2\pi)^{-3/2}\int \exp(i\,\boldsymbol{q}\,\boldsymbol{r})\,C(\boldsymbol{r})\,\mathrm{d}^3\boldsymbol{r}$.

When this result is now substituted into the intensity correlation function [Eq. (4.4)] and the integrals over $\boldsymbol{r}$ and $\boldsymbol{r'}$ are executed, one arrives at:

$$\begin{aligned} G(\tau) &= \frac{(2\pi)^{-3}\,\langle C\rangle \int \left(\int p(\boldsymbol{r})\mathrm{e}^{i\,\boldsymbol{q'}\,\boldsymbol{r}}\mathrm{d}^3\boldsymbol{r}\right)\left(\int p(\boldsymbol{r'})\mathrm{e}^{-i\,\boldsymbol{q'}\,\boldsymbol{r'}}\mathrm{d}^3\boldsymbol{r'}\right)\mathrm{e}^{-D\,\boldsymbol{q'}^2\tau}\,\mathrm{d}^3\boldsymbol{q'}}{\left(\langle C\rangle \int p(\boldsymbol{r})\,\mathrm{d}^3\boldsymbol{r}\right)^2} + 1 \\ &= \frac{\int \tilde{p}(\boldsymbol{q'})\,\tilde{p}(-\boldsymbol{q'})\,\mathrm{e}^{-D\,\boldsymbol{q'}^2\tau}\,\mathrm{d}^3\boldsymbol{q'}}{\langle C\rangle\left(\int p(\boldsymbol{r})\,\mathrm{d}^3\boldsymbol{r}\right)^2} + 1 \\ &= \frac{\int \tilde{p}(\boldsymbol{q'})\,\tilde{p}(-\boldsymbol{q'})\,\mathrm{e}^{-D\,\boldsymbol{q'}^2\tau}\,\mathrm{d}^3\boldsymbol{q'}}{\langle C\rangle\,(2\pi)^3\tilde{p}^{\,2}(\boldsymbol{0})} + 1 \end{aligned} \tag{4.11}$$

where $\tilde{p}(\boldsymbol{q})$ is the Fourier transform of the effective excitation/ detection profile, that is, the optical transfer function (OTF). For the Gaussian effective point-spread function given by Eq. (4.2) the OTF is again Gaussian:

$$\tilde{p}(\boldsymbol{q}) = \frac{p_0\,{w_0}^2\,z_0}{8}\exp\left[-\frac{{w_0}^2}{8}\left({q_x}^2+{q_y}^2\right)\right]\exp\left(-\frac{{z_0}^2}{8}{q_z}^2\right) \tag{4.12}$$

which, when inserted into the expression (4.11), yields:

$$G(\tau) = \frac{1}{\langle C\rangle\;\pi^{3/2}\,{w_0}^2\,z_0}\left(1+\frac{4D\,\tau}{{w_0}^2}\right)^{-1}\left(1+\frac{4D\,\tau}{{z_0}^2}\right)^{-1/2}. \tag{4.13}$$

If one defines $V = \pi^{3/2}\,{w_0}^2\,z_0$ as the detection volume, then $N = V\,\langle C\rangle$ is the number of molecules in this volume. Applying Einstein's diffusion formula $\tau = w^2/4D$, one finally obtains:

$$G(\tau) = \frac{1}{N}\left(1+\frac{\tau}{\tau_{\mathrm{D},xy}}\right)^{-1}\left(1+\frac{\tau}{\tau_{\mathrm{D},z}}\right)^{-1/2} + 1 \tag{4.14a}$$

$$= \frac{1}{N}\left(1+\frac{\tau}{\tau_{\mathrm{D},xy}}\right)^{-1}\left(1+\frac{\tau}{K^2\,\tau_{\mathrm{D},xy}}\right)^{-1/2} + 1. \tag{4.14b}$$

Here, $\tau_{\mathrm{D},xy} = {w_0}^2/4D$ and $\tau_{\mathrm{D},z} = {z_0}^2/4D$ are the characteristic diffusion times in the lateral and axial directions, respectively, and $K = z_0/w_0$ is a structural parameter that is solely determined by the shape of the detection volume. Equations (4.14) are the model functions most widely used when purely diffusional FCS data have to be fitted. The latter form (4.14b) is advantageous if, in a series of FCS measurements, the excitation conditions remain constant. Then, K can be kept constant and only N and $\tau_{\mathrm{D},xy}$ have to be fitted. In the STED-FCS experiments described below, however, the shape of the focus changes in a series of measurements and the former expression (4.14a) is more appropriate for curve fitting.

The definition of the detection volume used above is somewhat arbitrary, because it is not constrained by any natural boundary. Especially for non-Gaussian shaped detection

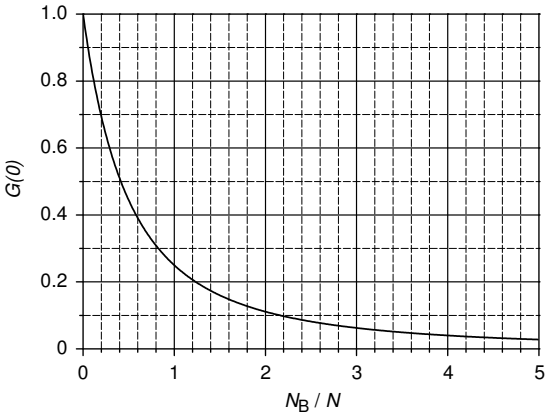

Fig. 4.2: Decrease of the zero-time FCS amplitude with increasing background. The amplitude $G(0)$ is plotted as a function of the relative background level given by N_{B}/N where N is the number of fluorescent particles in the detection volume and N_{B} is the background in equivalent numbers of molecules.

volumes, it is more convenient to define the number of in-focus molecules as $N \equiv 1/G(0)$ which is then related to the effective detection volume $p(\boldsymbol{r})$ by

$$N = \langle C \rangle \frac{\left(\int p(\boldsymbol{r})\,\mathrm{d}^3\boldsymbol{r}\right)^2}{\int p^2(\boldsymbol{r})\,\mathrm{d}^3\boldsymbol{r}}, \tag{4.15}$$

which is easily derived from Eqs. (4.4) and (4.9) by setting $\tau = 0$. This equation emphasizes that the number of molecules in the detection volume N does not depend on the laser intensity or on the specific brightness of the fluorophore. This important charactistic of FCS should be kept in mind.

Finally, it must be noted that the derivation thus far has been based on a purely fluorescent signal in the absence of any background contributions. In reality, however, several sources of background are ubiquitous, the most common of which are detector dark counts as well as Raman and Rayleigh scatttering. If the fluorescence signal is contaminated with significant amounts of such uncorrelated background, the zero-time amplitude $G(0)$ is no longer proportional to $1/N$ but is rather given by [118]

$$G(0) \propto \frac{N}{(N + N_{\mathrm{B}})^2} \tag{4.16}$$

where N_{B} is the equivalent number of molecules accounting for the background count rate. This relationship is plotted in Fig. 4.2 and emphasizes the necessity to optimize any FCS setup for as little background as possible.

4.3.2 Theory of Fluorescence Intensity Distribution Analysis

Apart from the correlation approach persued in FCS, the fluorescence fluctuations can alternatively be analyzed in terms of the photon counting histogram which is generated from the number of photocounts detected within consecutive, constant time intervals. While several other formalisms for the analysis have been proposed [14, 110], the approach

of fluorescence intensity distribution analysis (FIDA) introduced by *Kask* [13, 119] is adopted here and is briefly summarized in the following.

Unlike FCS, FIDA does not gather information from the intensity fluctuations resulting from dynamic processes but rather from the differences in brightness of different coexisting species or molecular populations. Thus, it characterizes the momentary state of a system instead of its temporal evolution (even though, of course, processes which are slower than the counting interval and which result in brightness changes of the involved species can be investigated.) As to the prerequisites of FIDA, an ideal solution is assumed, that is, the particle locations are uncorrelated and are Poisson distributed as is the number of photon counts per molecule and unit time. Further, the emission from a fluorophore located at position $\boldsymbol{r}$ is assumed as a product of the specific particle brightness $q = \sigma_{\mathrm{abs}}\, q_{\mathrm{fl}}\, q_{\mathrm{det}}$ and the effective PSF $p(\boldsymbol{r})$. In FIDA, this product is commonly termed the spatial brightness function. Consequently, because no temporal dependence of the emission intensity is included, effects like triplet formation and saturation are neglected. For the same reason, the photon counting interval must be kept short compared to diffusional transit time of the particles. (Commonly, with diffusion times on the order of $\sim$80 μs, counting intervals of 20–40 μs are used.) Based on these assumptions, the photon counting histogram can be derived theoretically.

To begin with, the exact shape of the brightness function $p(\boldsymbol{r})$ is disregarded, and the formalism is developed for discrete volume elements ΔV_i in which the focal intensity p_i is assumed to be constant. The probability of detecting n photocounts originating from one such volume element is given by the following sum:

$$P_i(n) = \sum_{m=0}^{\infty} P(m) P(n|m). \tag{4.17}$$

Here, $P(m)$ is the probability of finding m molecules in the volume element, and $P(n|m)$ is the conditional probability that n photons are detected during the dwell time Δt provided that m molecules are inside ΔV_i. The sum accounts for the fact that $0, 1, 2, \ldots \infty$ molecules may be present. Both the number of molecules m and the number of photocounts detected from m molecules are assumed to be Poisson distributed with the mean values given by $\langle m \rangle = c\,\Delta V_i$ and $\langle n|m \rangle = mqp_i\Delta t$, respectively, where c is the particle concentration. Hence,

$$P_i(n) = \sum_{m=0}^{\infty} \frac{(c\,\Delta V_i)^m}{m!}\, \mathrm{e}^{-c\,\Delta V_i}\, \frac{(mqp_i\Delta t)^n}{n!}\, \mathrm{e}^{-mqp_i\Delta t} \tag{4.18}$$

is a double Poisson distribution. Now, to account for the inhomogenously illuminated detection volume V, assume that V is composed of two subvolumes ΔV_1 and ΔV_2 at first. While the sum of detected photons in both volumes has to be constant, the counts may be

partitioned arbitrarily among the two subvolumes. Thus,

$$P(n) = \sum_{i_1} P_1(i_1)P_2(n - i_1) = P_1 \otimes P_2.$$

The subvolumes may again be split up and the probability distributions of the subvolumes be replaced with expressions as above. By recursively repeating this procedure, the general expression for an inifite number of volume elements is obtained which is the serial convolution of the individual probability distributions P_i:

$$P(n) = \sum_{\{i_j\}} \prod_j P_j(i_j)\delta\left(n - \sum_l i_l\right) = P_1 \otimes P_2 \otimes P_3 \otimes \ldots \tag{4.19}$$

After insertion of the individual P_i from Eq. (4.18), this equation yields the theoretical expression for the photon counting histogram. However, in this form it is unsuable for fitting purposes because the (infinite number of) convolutions cannot be carried out numerically. However, the equation can be transformed into a closed expression by using the mathematical tool of *generating functions*. In general, the generating function of $P_i(n)$ is simply defined as

$$G_i(\xi) = \sum_{n=0}^{\infty} P_i(n)\xi^n. \tag{4.20}$$

where ξ is a complex number. It should be noted that the generating functions are a purely mathematical construct which have no physical representation. However, if ξ is restricted to the complex unit circle, i.e. $\xi \rightarrow \exp(-i\phi)$, then the $G_i(\phi)$ is the Fourier series of the probability distribution, and $P(n)$ can be unambigously reconstructed from $G(\phi)$ by a simple Fourier transform:

$$P(n) = \frac{1}{2\pi} \int G(\phi)\mathrm{e}^{-in\phi}\mathrm{d}\phi. \tag{4.21}$$

The advantage of using generating functions to express the total probability distribution is that, according to the convolution theorem, it converts the serial convolutions of Eq. (4.19) into a product:

$$G(\xi) = \prod_0^{\infty} G_i(\xi). \tag{4.22}$$

The derivation of the explicit expression for $G(\xi)$ is straightforward and is carried out in two steps. First, the double Poisson distribution of Eq. (4.18) is inserted into the definition of the generating function, Eq. (4.20):

$$G_i(\xi) = \mathrm{e}^{-c\,\Delta V_i} \sum_{m=0}^{\infty} \frac{(c\,\Delta V_i)^m}{m!} \mathrm{e}^{-mqp_i\Delta t} \sum_{n=0}^{\infty} \frac{[m\xi qp_i\Delta t]^n}{n!} \tag{4.23}$$

$$= \exp\left[c\,\Delta V_i\left(\mathrm{e}^{(\xi-1)qp_i\Delta t} - 1\right)\right]. \tag{4.24}$$

Here, the substitution $\sum_n x^n/n! = \mathrm{e}^x$ has been applied twice. Second, the generating function for the whole volume is obtained by inserting the $G_i(\xi)$ into Eq. (4.22)

$$G(\xi) = \exp\left(c \sum_i \left[\mathrm{e}^{(\xi-1)q\Delta T p_i} - 1\right] \Delta V_i\right). \tag{4.25}$$

Because the background signal is also Poisson distributed, it is easily included into the formula by extending the product of Eq. (4.22) by a factor $G_{\mathrm{bg}}(\xi) = \exp\left[\mu_{\mathrm{bg}}\Delta t(\xi-1)\right]$ which is the generating function of the Poissonian background with the mean value μ_{bg}. Finally, taking the limit as $\Delta V \to \mathrm{d}V$ and replacing the summation by an integration, one arrives at:

$$G(\xi) = \exp\left((\xi-1)\mu_{\mathrm{bg}}\Delta t + c\int_V \left[\mathrm{e}^{(\xi-1)q\Delta t p(\boldsymbol{r})} - 1\right] \mathrm{d}V\right). \tag{4.26}$$

(An extension to multiple different species is easily incorporated into the expression by inserting a summation over all species.) This closed form of the generating function allows to calculate $P(n)$ by numerical integration over the volume V, followed by a fast Fourier transform. Least squares fitting or, if the signal intensities are low, the maximum-likelihood criterion may be used to find the optimal values for the parameters c and q to reproduce the experimental data. Thus, just as FCS, FIDA provides the particle concentration but, in addition, it also gives the specific brightness of each species.

Remains the question how to represent the brightness distribution $p(\boldsymbol{r})$. Besides being computationally expensive to evaluate, the integral over a three-dimensional Gaussian profile has been shown to yield poor fits to experimental photon counting histograms [120]. However, a much more flexible formalism can be derived by establishing a relationship between the volume V and the brightness profile $p(\boldsymbol{r})$. By setting $u \equiv -\ln p(\boldsymbol{r})$, one can show that, for a 3D Gaussian profile,

$$\frac{\mathrm{d}V}{\mathrm{d}u} \propto \sqrt{u}. \tag{4.27}$$

Thus, the three-dimensional spatial integration can be replaced by the one-dimensional integration over the surfaces of constant brightness which is much faster to perform. Furthermore, Eq. (4.27) can be easily modified to account for deviations from the Gaussian profile. It has been found empirically that the approach

$$\frac{\mathrm{d}V}{\mathrm{d}u} \propto (1 + A_0 u + A_1 u^2) u^{A_2} \tag{4.28}$$

is particularly suited to describe the brightness profile in a confocal setup. The free parameters A_0, A_1 and A_2 are chosen to optimally accommodate the experimental data. For $A_0 = A_1 = 0$ and $A_2 = 0.5$, the above expression is equivalent to Eq. (4.27), but it has

been found that parameter values of $A_0 \approx -0.4$, $A_1 \approx 0.1$ and $A_2 \approx 1$ usually yield the best fits [119]. Once again, it is emphasized that Eq. (4.28) is adopted solely for its good match between the experimental histogram and the fitted curve [120] and that it has no further physical motivation.

4.4 The STED-FCS Concept

As has been demonstrated in Sect. 2.5 and previous work on STED microscopy, stimulated emission depletion offers an attractive approach to reduce the focal spot size in one or more directions. Unlike the other volume reduction methods described in Sect. 4.2, it has the appealing advantage that the diffusion is not affected by any mechanical constraints. Its applicability to FCS is examined theoretically and experimentally in the subsequent sections.

In order to produce a reduced focal volume using the STED technique, it is crucial that the intensity distribution of the STED focus feature a zero-intensity minimum at the center (such that fluorescence is not quenched there) but high intensity in the focal periphery to achieve complete fluorescence depression. Several means to achieve such an intensity distribution are conceivable and have been introduced in Sect. 1.3 [79, 86]. In this chapter, the three phasefilters shown in Fig. 4.3 (top) are evaluated for their suitability in STED-FCS experiments. The planar wavefront incident on the phasefilters is retarded by π (or have a wavelength) in the gray shaded regions but is unaffected elsewhere. The focal intensity distributions which arise upon focusing these modulated wavefronts were calculated using Eq. (1.11). Lateral and axial sections through the resulting PSFs are shown in Fig. 4.3, middle and bottom, respectively. As required, all STED foci share a (near) zero-intensity minimum at the center and laterally and/ or axially displaced intensity maxima.

To derive the effective detection volumes which result from these STED intensity distributions, one has to consider that the STED efficiency depends nonlinearly on the applied intensity [72, 73]. As was shown in Sect. 3.2, to a good approximation this dependence can be modeled by a monoexponential function:

$$\eta(\boldsymbol{r}) = \frac{F_{\mathrm{STED}}(\boldsymbol{r})}{F_0(\boldsymbol{r})} = \mathrm{e}^{-\sigma_{\mathrm{STED}}\, h_{\mathrm{STED}}(\boldsymbol{r})\, \tau} \tag{4.29}$$

where $\eta(\boldsymbol{r})$ is the fluorescence depletion factor at position $\boldsymbol{r}$ and $F_0(\boldsymbol{r})$, $F_{\mathrm{STED}}(\boldsymbol{r})$ denote the fluorescence intensities originating at position $\boldsymbol{r}$ in the absence and presence of STED, respectively. σ_{STED} is the stimulated emission cross section and $h_{\mathrm{STED}}(\boldsymbol{r})$ is the STED PSF given in photons per unit area and time. In order to calculate the effective PSFs $h_{\mathrm{eff}}(\boldsymbol{r})$, the image formation Eq. (1.10) for the STED microscope is used:

$$h_{\mathrm{eff}}(\boldsymbol{r}) = \eta(\boldsymbol{r}) h_{\mathrm{exc}}(\boldsymbol{r}) \left[h_{\mathrm{det}}(\boldsymbol{r}) \otimes o(\boldsymbol{r})\right].$$

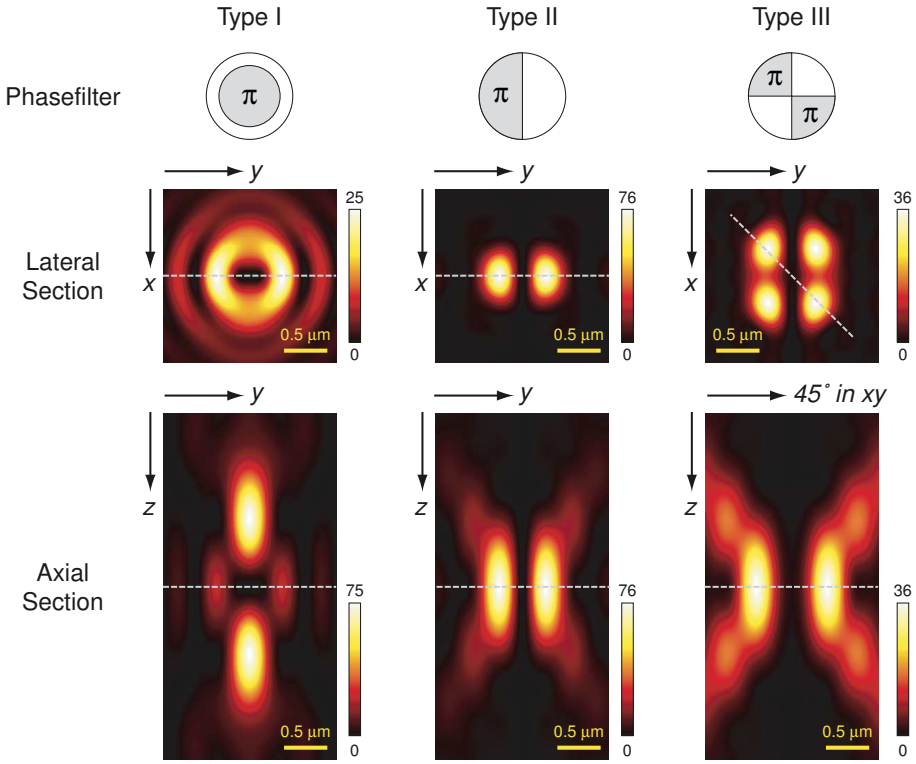

Fig. 4.3: Phasefilters and resulting STED foci (calculation). The top row shows the phasefilters investigated for STED-FCS. Gray regions indicate a phase shift of π, i.e. half a wavelength. The middle and the bottom rows show lateral and axial sections through the resulting PSFs, respectively; x, y and z polarization components have been added up. The gray dotted lines indicate the respective orthogonal section. All resulting STED-PSFs feature a (near) zero-intensity minimum at the origin but show axially (type I) and/ or laterally (type II & III) displaced intensity maxima. The simulation parameters were chosen to match the experimental conditions: $\lambda_{\mathrm{STED}} = 790\ \mathrm{nm}$, $\mathrm{NA} = 1.2$, $n = 1.33$, linearly (x-polarized) incident light.

where $h_{\mathrm{exc}}(\boldsymbol{r})$, $h_{\mathrm{det}}(\boldsymbol{r})$ are the excitation and detection PSFs and $o(\boldsymbol{r})$ is the pinhole function (see (1.8)). The process of image formation is illustrated in Fig. 4.4. To the left, the combined excitation and detection PSFs are shown which were calculated using Eq. (1.11) followed by convolution with the pinhole function. The fluorescence reduction maps $\eta(\boldsymbol{r})$ shown in the center were derived from the STED PSFs (Fig. 4.3) by substituting them for $h_{\mathrm{STED}}(\boldsymbol{r})$ into Eq. (4.29). The effective PSFs $h_{\mathrm{eff}}(\boldsymbol{r})$ are then obtained by simple multiplication (Fig. 4.4, right). In order to be able to compare the three phasefilters, all calculations were done using the same incident optical power which was equal to a peak intensity of 1 GW cm^{-2} of the regular STED focus without a phasefilter.

As can be expected from the STED intensity distributions, the type I phasefilter (Fig. 4.4, top) mainly reduces the PSF along the axial direction and only at high STED powers leads to a lateral volume reduction. As a result, a near-spherical effective sample vol-

ume is achieved. On the contrary, the type II phasefilter (middle) substantially constricts

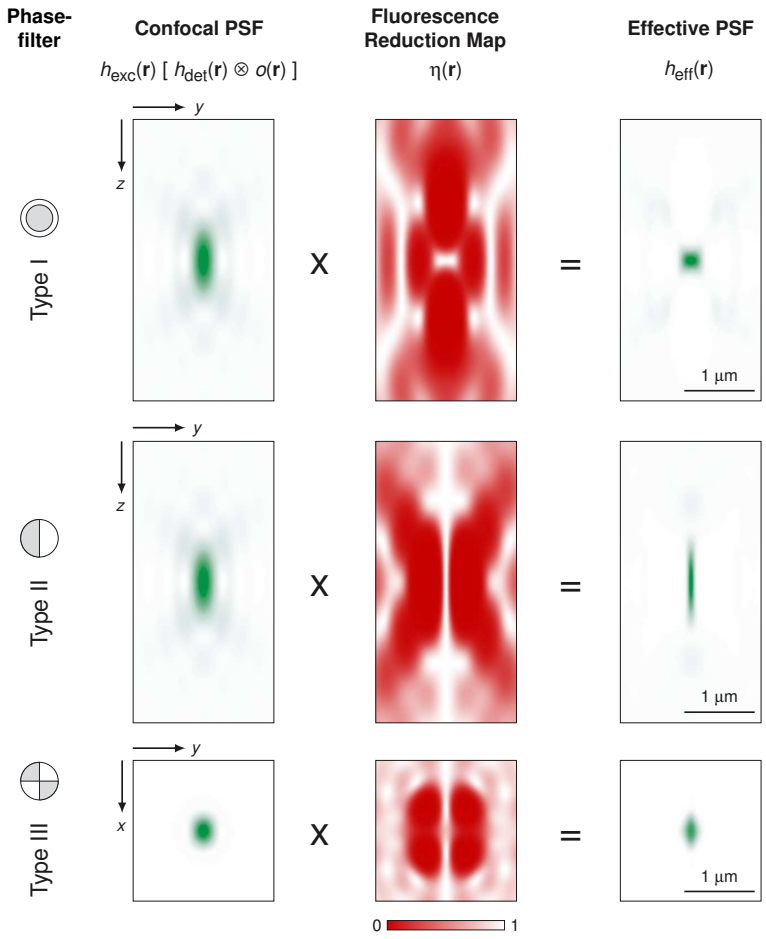

Fig. 4.4: Comparison of the effective detection volumes resulting from the use of phasefilters type I through type III. The excitation/ detection PSFs were calculated based on the following parameters: $\lambda_{\mathrm{exc}} = 585$ nm, $\lambda_{\mathrm{det}} = 680$ nm, pinhole diameter $d = 62.5$ μm, $\sigma_{\mathrm{STED}} = 0.5 \times 10^{-16}$ cm^2. The optical STED power was identical in all cases and corresponds to a peak intensity of 1 GW cm^{-2} of the regular STED focus (without a phasefilter). All other parameters were used as stated in the caption of Fig. 4.3.

one lateral dimension (the one perpendicular to the polarization of the STED laser) but leaves the other dimensions mostly unaffected. Just as type II, the type III phasefilter (bottom) induces a (mostly one-dimensional) lateral constriction but has no effect along the z axis. It also suffers from some residual (y polarized) STED intensity in the center which amounts to ∼4% of the peak maximum. While the symmetry of the intensity distribution in the type III case can be improved by using circularly polarized light, the residual intensity in the center remains the same.

To evaluate the different phasefilters for their suitability for STED-FCS, the volume

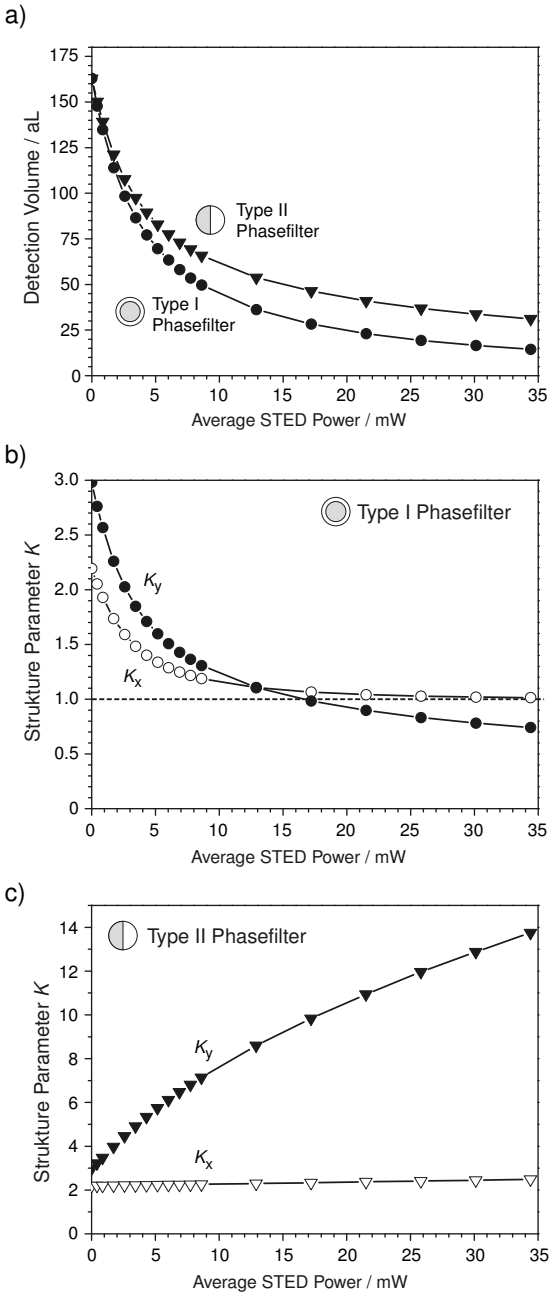

Fig. 4.5: a) Reduction of the effective detection volume as a function of average STED power for the circular (type I) and the semicircular (type II) phase retardation filters. While the volume effect only moderately deviates by a factor of approx. two, significant differences appear in the focal structure as indicated by the structure parameters $K_x = z_0/w_x$ and $K_y = z_0/w_y$ (b and c). For the type I phasefilter, both K_x and K_y converge to nearly unity (the differences are caused by the linear polarization of the incident laser light) and, thus, the focus approaches a sherical geometry. This is beneficial for the analysis of FCS curves because only a single diffusion time remains. On the contrary, for the type II phasefilter, the focal volume becomes increasingly anisotropic as is indicated by the increase in K_y.

reductions and structural changes of the effective detection volume as a function of STED power are now analyzed in a (semi)quantitative way. From the sections in Fig. 4.4, intensity profiles along the x, y and z axes were extracted and fitted with Gaussian functions which proved to be an appropriate model except for the x direction of type III (and, to a lesser extent, the y direction of type I). From the determined parameters w_x, w_y and w_z, the effective focal volumes V and structure parameters $K_{x,y}$ were calculated for phasefilters I and II according to $V = \pi^{3/2} w_x w_y w_z$ and $K_{x,y} = w_z/w_{x,y}$, see Fig. 4.5. From

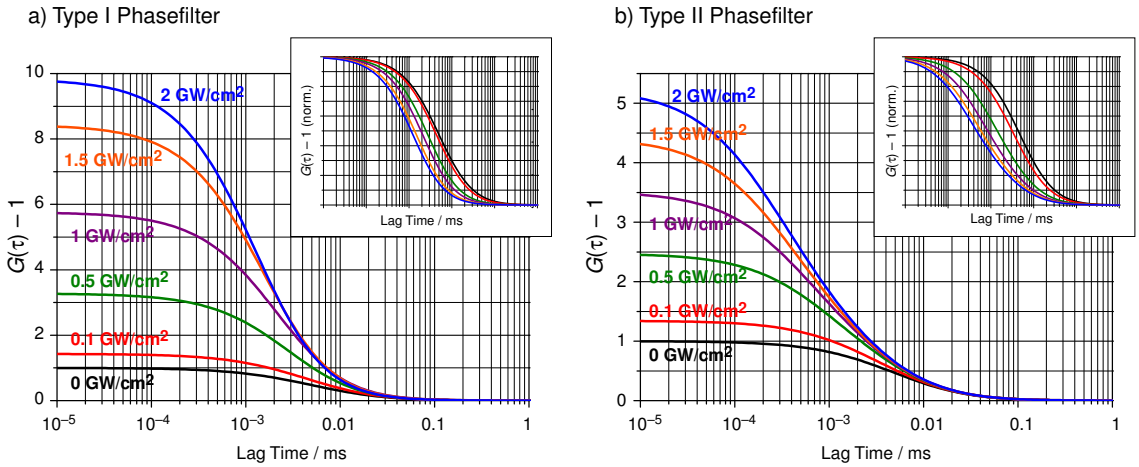

Fig. 4.6: STED-FCS curves calculated on the basis of the previously determined effective focal spot sizes and for a constant concentration. As the STED peak intensity increases from 0 to 2 GW cm^{-2}, the amplitudes increase and the diffusion times decrease. To better visualize the reduction of the diffusion times, the insets show the same set of FCS curves normalized to unity.

this plot, it can be seen that the type I phasefilter is superior to the other types. For a given STED power, it attains the most significant volume reduction, in this example up to 10fold. Under identical conditions, the type II phasefilter only achieves a 5fold volume decrease. However, the circular (type I) phasefilter has another significant advantage over the other types which is the focal shape as is illustrated by the evolution of the structure parameters at increasing STED powers. By comparing Fig. 4.5a) and b), one recognizes that the structure parameters of the circular phasefilter converge towards unity, that is, the focal volume approaches a spherical geometry. On the other hand, the structure parameter K_y of the type II phasefilter steadily increases while K_x remains constant, indicating a highly anisotropic focus. However, a spherical detection volume (where $w_x \approx w_y \approx z_0$) is highly desirable in FCS experiments because it reduces the number of diffusion times to be fitted to a single one. Even worse, by using phaseplate II, the approximate symmetry in the x and y directions is broken resulting in three disctinct diffusion times: $\tau_{\mathrm{D},x} = {w_x}^2/4D \approx 5$ μs, $\tau_{\mathrm{D},y} = {w_y}^2/4D \approx 0.2$ μs and $\tau_{\mathrm{D},z} = {z_0}^2/4D \approx 330$ μs (for $D = 2.5 \times 10^{-5}$ cm^2 s^{-1}). These diffusion times span more than three orders of magnitude which are not available to study photophysical processes like e.g. triplet formation.

Using the previously determined effective focal sizes (Fig. 4.5), FCS curves at a fixed concentration for the type I and type II phaseplates were calculated on the basis of Eq. (4.14a), see Fig. 4.6. As expected, the reduction in focal volume with increasing STED power is accompanied by a shortening of the diffusion times and by an increase in the curves' amplitudes which is due to that fact that the average number of molecules in

the focus becomes smaller. It is also seen that the FCS curves with the type II phaseplate are rather slanted than shifted towards shorter lag times as the STED intensity increases which hides processes occuring on the same timescale.

Both because of the most pronounced volume reduction effect, the increasingly isotropic effective volume and the true zero STED intensity in the center of the focus, the circular (type I) phaseplate appears to be the phaseplate of choice for FCS applications. However, it must be noted that, while the focal volume may be theoretically reduced arbitrarily by increasing the STED intensity, the minimal focal size is constrained intrinsically by the correlation method itself. In order to generate correlated fluorescence emission, at least two photons have to be detected from a single fluorophore within the molecule's residence time in the focal volume. Unless a solid sample with fixed molecules is used, this residence time is limited by diffusion. From the molecule's viewpoint, the ultimate limit for emitting two subsequent photons is set by the fluorescence lifetime (which, however, is rather of theoretical than experimental relevance). In practice, the repetition rate of the laser system and the excitation and detection efficiencies are the restricting parameters. Assume, for example, that the probability to detect a photon after an excitation pulse is 2% (based on a 40% excitation and a 5% detection probability). Then, at a repetition rate of 76 MHz, every 660 ns a photon is detected on average. Taking this number as the required residence time of a molecule in the detection volume, the minimal required dimensions can be estimated to be $\sqrt{4D\tau} \approx 80$ nm which is well above the attainable resolution in a STED microscope.

4.5 Experimentals

4.5.1 Setup Modifications

For the STED-FCS experiments, the setup was modified both to improve the signal-to-noise ratio and to simplify the aligning procedures. First, the grating-based pulse stretchers were removed from the setup and were replaced by a pulse stretching scheme exploiting the group velocity dispersion (GVD) in optical fibers. The pulses from the Ti:Sapphire laser were pre-stretched by guiding them through 19 cm of SF6 glass and were then focused into a polarization-preserving optical singlemode fiber (100 m, FS-LS-4616, Thorlabs GmbH, Karlsfeld, Germany) to give pulses of 85–140 ps length (depending on the applied power). Likewise, the OPO pulses were pre-stretched and were coupled into a polarization maintaining singlemode fiber (8 m, PointSource, Southampton, UK) to yield pulses of 6–8 ps length. By using optical fibers, not only the setup alignment was greatly simplified but also the overall light losses were significantly reduced because additional spatial filtration of the laser beams became unnecessary.

For the FCS experiments, the oxazine dye MR 121 was used because of its better water

compatibility compared to JA 26. Optimal STED condititions were found at wavelengths between 785 nm and 790 nm resulting in an excitation wavelength of approx. 565 nm provided by the OPO. Unfortunately, at this wavelength, the water Raman band between 3200 and 3500 cm^{-1} [121] arises between 695 nm and 710 nm which is within the fluorescence detection window. To overcome this complication, the nonlinear KTP crystal inside the OPO was exchanged for an RTP crystal which, at the same pump wavelength, provided pulses at 585 nm. In addition to moving the Raman band outside the detection range, this measure shifted the excitation wavelength towards the absorption maximum of MR 121 which is beneficial in terms of required excitation power and, presumably, photobleaching.

The correlation curves were directly obtained by connecting the APD to a digital hardware correlator (ALV 6000, ALV GmbH, Langen, Germany). Alternatively, raw photon counting traces were acquired by operating the TCSPC electronics in the FIFO mode which allowed to store the microscopic and macroscopic photon arrival times for later processing in software.

The detection efficiency was optimized by replacing all mirrors in the detection path with highly reflective dielectric broadband mirrors ($T > 99\%$ for s- and p-polarization, *MaxMirror*™, Semrock, Inc., Rochester, NY, USA). The oil-immersion objective lens used in the previous experiments was replaced with a water immersion lens (HCX PL APO 63×/1.20W CORR CS, Leica Microsystems, Wetzlar, Germany) to be used without a coverslip. The adoption of this lens guaranteed that no effects like adsorption/ desorption or diffusion constraints due to a surface close to the detection volume disturbed the FCS measurements, and it also removed the occurence of varying aberrations due to different coverslip thicknesses which may result in inferior STED PSFs.

The phase retardation filters for shaping the STED PSF were manufactured by evaporating cryolite (sodium hexafluoroaluminate, Na_3AlF_6, $n_{790} = 1.33$) onto flat glass substrates covered by an appropriately shaped aluminum mask. For the circular (type I) phasefilter, optimal PSFs were found using a diameter of 5.0 mm and a thickness of $\sim 1180\ \mathrm{nm}$. The phasefilter was placed into the expanded STED beam and was centered by scanning gold nanobeads in reflectance mode until a satisfactory PSF was obtained. The scanning of the PSF was initially challenged by a strong background due to the reflection of the laser at the water-glass interface. In order to minimize this reflection, the coverslips were coated with a transparent fluoropolymer (CYTOP®, $M_W \approx 100000$, 9% wt solution in perfluorobutylamine, #53,357-2, Sigma-Aldrich Chemie GmbH, München, Germany) prior to adhering the gold beads. Because this fluoropolymer has an exceptionally low refractive index ($n_{550} = 1.34$) which is close to that of water, virtually all background was eliminated.

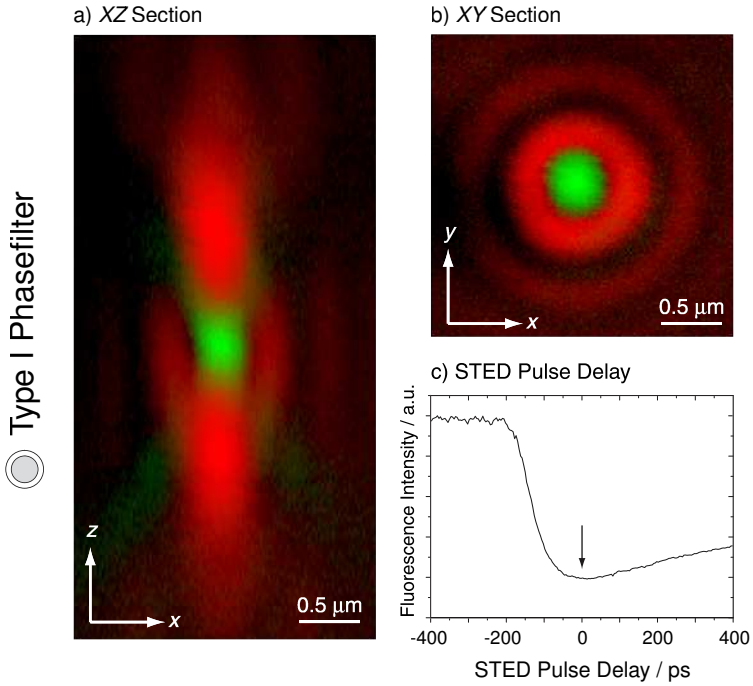

Fig. 4.7: Spatial and temporal PSF alignment using the circular (type I) phasefilter. a), b) The excitation laser is focused to a diffraction-limited spot (center) while the STED-PSF displays a central minimum and two axially offset main intensity maxima. To show more detail, the color tables are logarithmic. c) The delay of the STED pulse was adjusted to provide maximal STED efficiency (arrow, measured in a bulk solution of MR 121 in water).

4.5.2 STED-FCS Measurements

The excitation focus was aligned to coincide with the central minimum of the STED PSF which was verified by scanning a gold bead alternately with the excitation and STED lasers in reflectance mode (Fig. 4.7a, b). The temporal adjustment of the laser pulses was done by monitoring the fluorescence of a bulk solution of MR 121 in water while the optical delay of the STED pulses was scanned on a 800 ps range (Fig. 4.7c). The delay at the minimum of the fluorescence curve was adopted for the STED-FCS measurements.

Using this alignment, autocorrelation curves were acquired on a ∼50 nM solution of MR 121 in water. Initially, a reference FCS curve was acquired with the STED beam blocked (Fig. 4.8a). Excitation was performed at an average power of 85 μW. The measured curve was fitted with the three-dimensional diffusion model Eq. (4.14a) which reproduces the experimental data extremely well. In particular, no triplet buildup is observed which would cause a second decay component in the FCS curve on the microsecond timescale [54]. From the diffusion times determined by the fit, the structure parameter $K = z_0/w_0 = \sqrt{\tau_{\mathrm{D},z}/\tau_{\mathrm{D},xy}}$ is calculated to be 3.8 which is a typical value for a confocal detection volume. While keeping the dye concentration constant, the STED

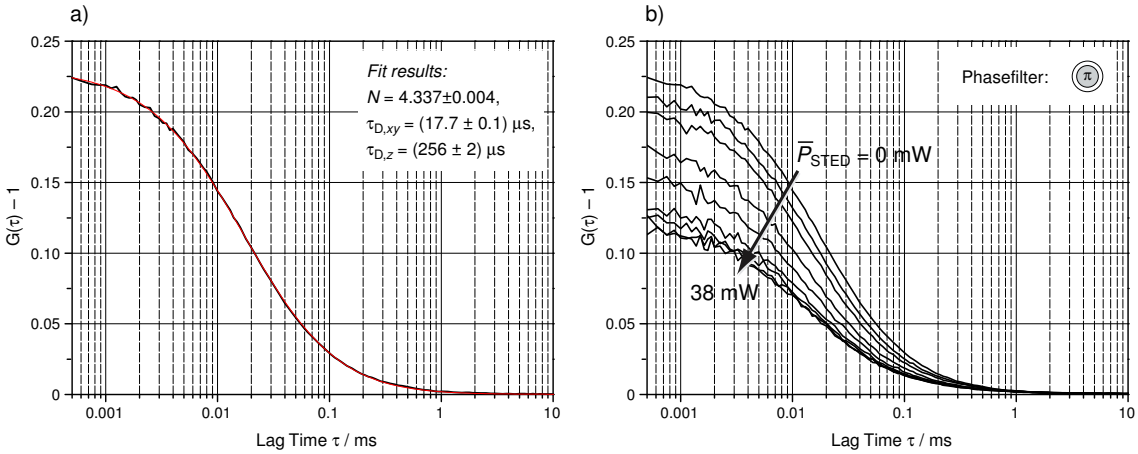

Fig. 4.8: (STED-)FCS curves measured in MR 121/ water (∼50 nM). a) Reference FCS curve (black) without STED and the fit (red) with the three-dimensional diffusion model. b) STED-FCS curves acquired at increasing STED laser powers (type I phasefilter).

laser was unblocked and FCS curves were acquired at increasing STED intensities, that is, at decreasing detection volumes (Fig. 4.8b). The highest average laser power applied was 38 mW. Without fitting the data, two important results can be found just by visual inspection of the set of curves. The most pronounced effect is the decrease in the correlation amplitude as the STED intensity is raised. This finding obviously violates the theoretical predictions according to which the amplitude is to increase upon a reduction of the detection volume and, accordingly, the particle number (see Fig. 4.6). On the contrary, the diffusional transit times through the focus become smaller with increasing STED intensity as is indicated by the shift of the autocorrelation curves towards lower lag times.

As for the reference FCS curve, the acquired STED-FCS curves were quantitatively analyzed by fitting them with the three-dimensional diffusion model Eq. (4.14a). Both the axial and, to a lesser extent and mainly at high intensities, the lateral dimensions of the effective detection volume are reduced when the STED power is increased, so both the lateral and the axial diffusion times should be optimized separately in each fit. However, because the count rates per molecule were relatively low from the beginning and even worsened as the STED intensity increased, the signal-to-noise ratio of the curves did not permit the indepedent determination of both parameters. Therefore, the lateral diffusion time $\tau_{\mathrm{D},xy}$ was taken from the reference measurement and was fixed in all other fits. The resulting axial diffusion times, the numbers of molecules in the focal volume, the total count rates and the count rates per molecule (as determined from the quotient of the latter two parameters) are shown in Fig. 4.9.

As was already discerned qualitatively, the axial diffusion time $\tau_{\mathrm{D},z}$ shows a decrease which is particularly pronounced at low STED powers but reaches a plateau level of 6 μs

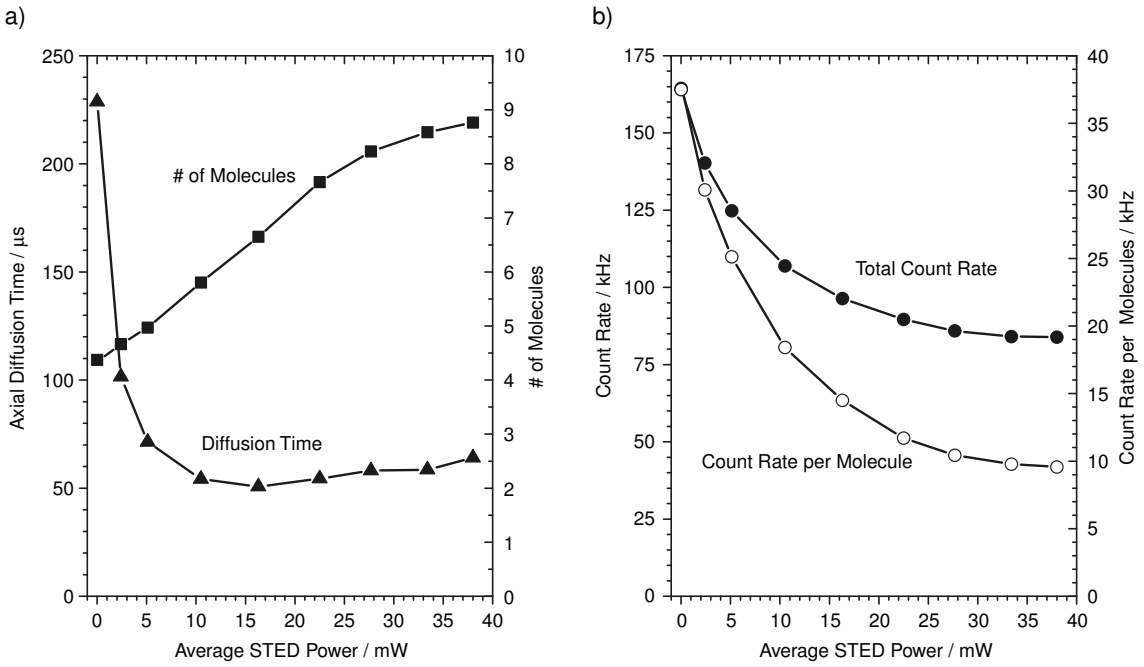

Fig. 4.9: STED-FCS fitting results. a) Axial diffusion time (▲) and number of molecules (■) in the detection volume, b) total count rate (●) and count rate per molecule (○).

at about 10 mW average power. The decrease by a factor of four points to an approximately twofold reduction of the axial extent of effective detection volume. In fact, above 10 mW STED power, a slight increase in the diffusion time may be identified possible origins of which are discussed below. Unlike the diffusion times which indicate a volume reduction, the (apparently) increasing number of molecules as determined from the $\tau = 0$ correlation amplitude suggests an unexpexted growth of the detection volume. The main question that needs to be addressed to resolve this conflict is whether the decrease in the correlation amplitude results from a real increase in the number of in-focus molecules or if it is caused by some kind of uncorrelated background signal which lowers the amplitude according to Eq. (4.16).

To explain a true increase in the particle number, two possible mechanisms are conceivable. First, besides stimulated emission, the STED pulse may also induce excitation of relaxed dye molecules either by two-photon or by single-photon anti-Stokes absorption resulting in an enlarged net excitation volume. However, this trivial cause was excluded by checking the emission of an MR 121 solution upon irradiation with the STED laser only. Even at the highest applied STED powers, the detected count rate was only slightly above the background level (< 400 Hz) which is negligible compared to the total count rate of 85–165 kHz. Yet another excitation mode would be two-photon, two-color excitation where one photon is provided by each laser pulse. While improbable due to the little spatial overlap of the two foci, it should also be noticeable as a peak around zero delay in

the STED pulse delay scan of Fig. 4.7c, which is not observed. Hence, a direct increase of the excitation volume due to spurious excitation effects can be excluded.

The second mechanism possibly responsible for an increase in the particle number is the optical tweezer effect which is a result of gradient forces that dielectric particles experience in a laser focus. While the trapping of micrometer-sized particles in a tightly focused near-infrared laser beam is a well-established technique [122, 123], the polarizability of a single molecule is generally considered to be insufficient to allow for its trapping. However, biased diffusion has been observed in correlation experiments [124, 125] in near-resonant one-photon excitation mode but not in two-photon absorption experiments, i.e. in the near-infrared region. Because the focal intensity used in the STED-FCS experiments is by a factor of 10–100 higher than commonly used for excitation, the possibility of dye accumulation in the focus due to constrained diffusion was nevertheless checked. The experiment was performed by removing the phase retardation filter from the expanded STED beam and by spatially superimposing both laser foci. Furthermore, the pulse order was reversed, that is, the STED pulsed arrived approx. 250 ps *before* the excitation pulse (see Fig. 4.10a). By adopting this scheme, hardly any stimulated emission depletion is afforded because, at the time when the STED pulse arrives, virtually all fluorescence has already been emitted. On the other hand, the reversed pulse order should not affect possible trapping effects because, in this regard, the laser's repetition rate of 76 MHz acts as a quasi-continuous source. Using this setting, a sequence of autocorrelation curves with increasing STED laser power was acquired. Curve fitting was conducted as outlined above and yielded the parameters plotted in Fig. 4.10b. As is demonstrated by these curves, no dye accumulation in the focal volume occurs. The diffusion time remains at a constant value of 20 μs throughout the whole range of STED powers. The discontinuity observed in the plot of the molecule number versus STED power is due to a temporal drift during the measurements which were started with a series ranging from 4 mW to 19 mW and were completed with the low-power measurements afterwards. The drift is attributed to a decrease of the bulk concentration as a result of dye adsorption on the objective lens' surface. Furthermore, the count rate per molecule remained remarkably constant, that is, to within 1% (data not shown). Given these unambiguous results, the hypothesis of a real increase in the number of molecules must be discarded.

To follow up on the decrease of the autocorrelation amplitude, a contribution of uncorrelated background signal must now be taken into account. This background may consist of scattered or stray light, but it may also originate from a second population of fluorescent molecules. These may have a different (and probably lower) specific brightness which does not suffice to contribute a clearly distinguishable component to the FCS curve. Rather, such a population would act as an uncorrelated background signal which lowers the correlation amplitude. As was pointed out in the theoretical considerations at the beginning of this chapter, FCS is not capable to differentiate between populations of

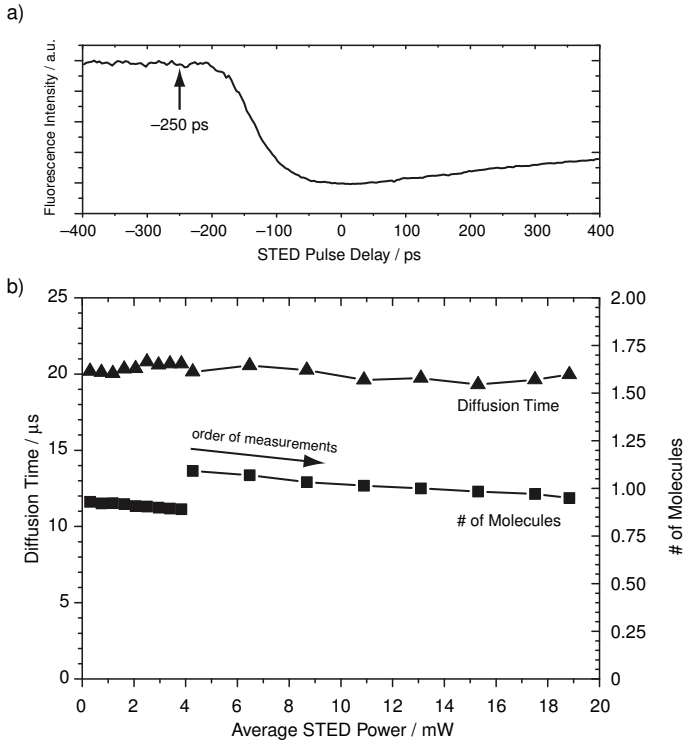

Fig. 4.10: STED-FCS using a reversed pulse order. a) The STED pulse delay was adjusted to −250 ps such that the STED pulse preceded the excitation pulse. b) The number of molecules in the detection volume (■) and the axial diffusion time (▲) plotted as a function of average STED power. While the diffusion time remains constant, the number of molecules shows a temporal drift which is attributed to a decrease in the bulk concentration due to adsoprtion of the dye on the surfaces.

different brightness, so the further analysis has to draw on different techniques.

4.5.3 Analysis of the TCSPC Histogram

As a first step towards the identification of the background contribution, the detected signal was analyzed in terms of the time-correlated single-photon counting histogram [47] which allows to discriminate scattered light from fluorescence on the basis of their respective emission timescales. While fluorescence is emitted in a few nanoseconds, both Raman and Rayleigh scattering occur quasi instantaneously. Thus, any scattering should disclose itself as narrow peak on top of the exponential fluorescence decay curve whose width is only determined by the system's impulse response function and the laser pulse lengths. Of course, two populations with identical lifetimes (i.e. two fluorescent populations which differ only in their specific brightness) cannot be separated by TCSPC.

The TCSPC histograms were acquired in a dilute solution of MR 121 for a series of

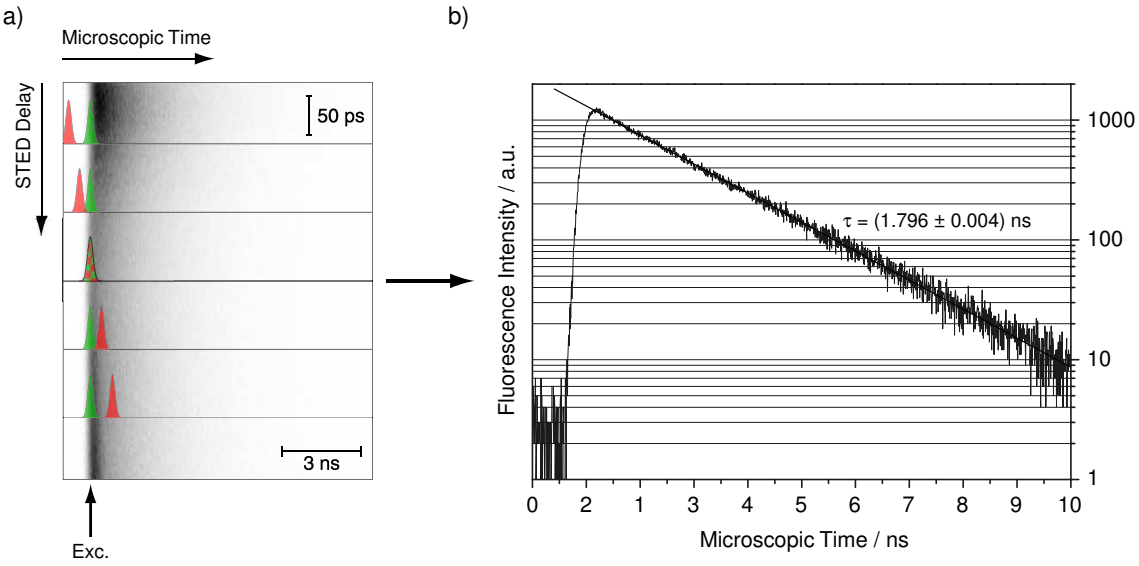

Fig. 4.11: a) Two-dimensional plot of the time-resolved fluorescence emission (horizontal axis) at increasing STED pulse delays (vertical axis). The pulses shown in the overlay indicate the timing of the fixed excitation pulse (green) and the moving STED pulse (red, timing not drawn to scale). b) At the maximum STED efficiency the TCSPC histogram shows only a single decay component.

STED pulse delays in the range from –250 ps to 500 ps which were set using the optical delay line. Here, negative numbers indicate that the STED pulse arrives before the excitation pulse. For this experiment, the APD was connected to the SPC-830 TCSPC electronics board. Figure 4.11a shows a two-dimensional plot of the time-resolved fluorescence emission (horizontal axis) at increasing STED pulse delays (vertical axis), that is, each horizontal line corresponds to a TCSPC histogram for one particular delay. From Fig. 4.11a, the optimal pulse timing was determined by summing up the intensity in the horizontal direction and finding the delay at which the integrated signal features a minimum. The histogram extracted at this delay (arbitrarily defined as zero) is plotted in Fig. 4.11b on a semilogarithmic scale which nicely demonstrates that only a single exponential component is present in the decay. By least-squares fitting the characteristic time constant was determined to be 1.8 ns which is the common value for the lifetime of MR 121 in water. Hence, scattering can be excluded as the source of background in the FCS curves.

4.5.4 Analysis of the FIDA Histogram

As the previous sections have shown, the background contribution responsible for the lowering of the amplitude of the autocorrelation curve cannot be differentiated from the wanted signal by its dynamic behavior only. On the one hand, it obviously does not con-

tribute sufficiently to the signal in order to appear as a separate decay component in the FCS curve and, on the other hand, it does not disclose itself with a characteristic lifetime in the TCSPC histogram. As has been discussed in the theoretical introduction of the various fluorescence fluctuation methods (Sect. 4.3), the analysis of the fluorescence intensity distribution (FIDA) allows to identify subpopulations on the basis of their different specific brightness. This approach is pursued next.

To analyze the photon counting histograms, the measurements described in Sect. 4.5.2 were essentially repeated with the main difference being the data processing. Unlike above, where the autocorrelation curve was calculated in hardware in real time, the APD detector was connected to the SPC-830 TCSPC board which was used in its FIFO mode. Thus, the photon counts were not processed immediately but were stored as raw data with their microscopic and macroscopic arrival times which refer to the start of the measurement and to the subsequent laser pulse, respectively. For each STED power setting in the range between 0 and 36 mW, a total of 256,000 photocounts were acquired within 20–50 s and were stored yielding data files of 100 MB each. From the raw data traces, FIDA histograms were generated by binning the counts into subsequent channels of 40 μs width and histogramming the counts per channel. Two exemplary FIDA histograms obtained from the runs without STED and at the highest STED power are shown in Fig. 4.12a. As is expected for a Poisson distributed random variable, the histogram for the run at high power is significantly narrower due to the lower average count rate. All acquired FIDA histograms were fitted using the 1D-FIDA++ method of the *FCS++ Analyze* software package (Version 1.2.5d, Evotec OAI AG, Hamburg, Germany). Best results were obtained when the background contribution bg, the concentration C_1 and the specific brightness Q_1 were optimized while the other parameters were kept fixed at $A_0 = -0.7$, $A_1 = 0.14$ and $A_2 = 1.5$. Strictly speaking, the bin width of 40 μs is too long to conform with the FIDA prerequisites, but the signal to noise level of the data did not allow to further narrow the bins. Therefore, the particle numbers determined by FIDA may be slightly underestimated. The parameters determined in the fitting procedure are plotted in Fig. 4.12b as a function of average STED power. As can be seen from these results, the FIDA analysis is in fact able to discriminate the background as a separate population. Unlike in the previous FCS analysis, the number of molecules in the focal volume is found to decrease by a factor of four with increasing STED power and reaches a plateau level at approx. 10 mW. At the same time, the background contribution rises about 5fold approaching saturation at the same power value.

Because the FIDA analysis directly provides the relative background contribution, it can be used to correct the particle numbers as determined from the zero-time autocorrelation amplitude. Using the expression for the FCS amplitude in the presence of background signal [Eq. (4.16)], one can set up the following equality to derive a correction factor for

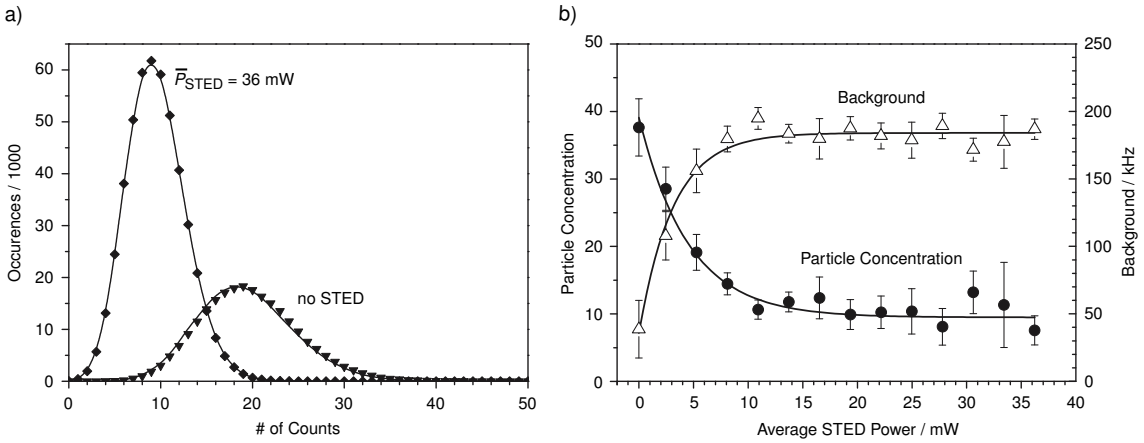

Fig. 4.12: FIDA Results. a) FIDA histograms without STED (▼) and at 36 mW average power (⧫). b) Particle concentration (●) and background (△) as a function of average STED power.

the particle number:

$$\frac{1}{N} = \frac{N_0}{(N_0 + N_\mathrm{B})^2}. \tag{4.30}$$

Here, N is the apparent number of molecules given by the inverse of the zero-time autocorrelation amplitude, N_0 is the true number of molecules in the detection volume and N_B is the background in equivalent numbers of molecules. Considering that the relative background B_rel is given by

$$B_\mathrm{rel} = \frac{I_\mathrm{bg}}{I_\mathrm{tot}} = \frac{N_\mathrm{B}}{N_0 + N_\mathrm{B}}, \tag{4.31}$$

Eq. (4.30) can be solved to give the following correction for the particle number:

$$N_0 = N\,(1 - B_\mathrm{rel})^2\,. \tag{4.32}$$

The effect of this correction is demonstrated in Fig. 4.13 which shows a series of STED-FCS measurements at increasing average STED powers. As has already been seen before, the axial diffusion time decreases (a) while, at the same time, the apparent number of particles goes up (b). However, if the correction (4.32) is applied with the relative background determined by a FIDA analysis, the increase is turned into a 7fold decrease in the particle number, just as is expected for a shrinking effective focus. It is instructive to compare the volume reduction as determined from the diffusion times with that obtained from the decrease in the particle numbers. For this comparison, the detection volumes have been inferred from the axial diffusion times according to $V \propto \sqrt{\tau_{\mathrm{D},z}}$ and have been normalized to the initial value without STED. Likewise, the corrected particle numbers have been referenced to the initial value. Both series are plotted in Fig. 4.13 and, unlike

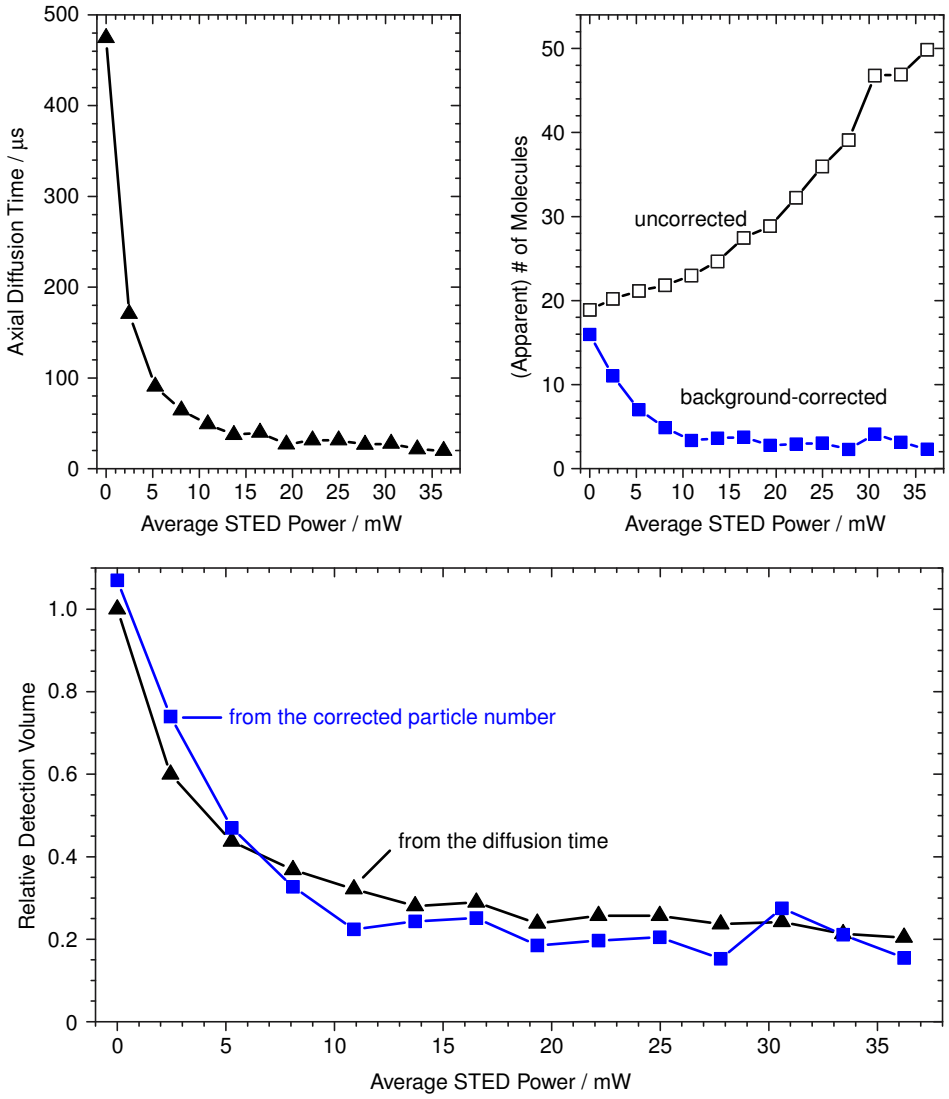

Fig. 4.13: FCS results before and after background correction. a) Axial diffusion time determined from the FCS curve. b) Number of molecules in the detection volume as obtained from the auto-correlation amplitude before (□) and after (■) background correction. c) Evolution of the relative detection volume as determined from the axial diffusion time $\tau_{D,z}$ (▲) and from the corrected particle numers (■).

before, now show a remarkable agreement in their evolution at increasing STED powers. While the FIDA analysis cannot shed light on the origin of the background signal present in the measurements, it has clearly confirmed its existence and has proven its suitability to correct the FCS results.

4.6 Discussion

The experiments presented in this chapter have shown that the implementation of a STED-based approach to reduced focal volumes in fluorescence fluctuation spectroscopy is challenged by a significant background contribution which has been identified in the FIDA analysis but seriously lowers the FCS amplitude. Unfortunately, the background counteracts the beneficial effect of the volume reduction.

Currently, two explanations seem plausible to explain the origin of the background contribution, one being optical and one spectroscopic by nature. To illustrate the presumed optical effect, it is once again referred to Fig. 4.4, top. In this map of the fluorescence depletion efficiency, two minima laterally offset of each main maximum can be identified where fluorescence is still appreciably excited but is not efficiently quenched. In the effective PSF, these regions appear as a weak additional cloverleaf-like structure on top of the central main maximum. Presumably, the fluorescence contributions from these regions are too weak to form a separate component in the FCS curve but may rather act as an uncorrelated background as was already suspected above. Alternatively, the attainable local STED efficiency may be limited to well below 100% for spectroscopic (and yet unidentified) reasons or because of imperfect experimental conditions. One conceivable mechanism that could explain a low STED efficiency is the rotation of the molecules in solution which, because of photoselection, may detract some fraction of the molecules from being depleted. However, to quantitatively assess the impact of rotational diffusion on the STED efficiency, very detailed dynamic simulations would have to be performed. Irrespective of the underlying mechanism, incomplete fluorescence depletion leaves some residual fluorescence which forms a flat but broad base which is underlying the sharply localized focus. As before, the comparatively delocalized fluorescence emission may act as an uncorrelated background signal. Unfortunately, it is virtually impossible to separate the two effects experimentally due to the inevitable averaging across the focal intensity distribution. In fact, both effects may occur concurrently.

While, currently, the background contribution cannot be experimentally excluded, a combination of several techniques of statistical analysis has been succesfully applied to unravel the reduction of the effective focal volume. Even if future developments in data analysis, in particular in multidimensional and global analysis techniques, will possibly allow to correct for background contributions on a routine basis, some experimental key parameters have to be futher optimized. This particularly holds for the count rate per

molecule which has been at the very limit of practicability. This parameter becomes increasingly important as the focal volume decreases because only photon emissions from the same molecule contribute to the FCS curve. Given the count rate of 100–150 kHz per molecule typically achieved in standard FCS experiments, some range is left for improvement.

Chapter 5

Conclusion and Outlook

In this thesis, the concept of stimulated emission depletion has been successfuly introduced into the field of single-molecule fluorescence spectroscopy. Probing and controlling the population of the excited state allows tangible information to be obtained that has been difficult or impossible to access so far in the ensemble and even on the single molecule level.

As a proof of concept, it has been shown that the fluorescence emission can be entirely suppressed by means of stimulated emission depletion. The STED-based on- and off-switching can be cycled many times without excessively affecting the fluorophore's photostability in a detrimental way. Given that the optical intensities applied for STED are approx. 1000fold higher compared to excitation, this finding is quite remarkable. It has been further demonstrated that, within the time resolution of the experiment, the fluorescence recovers instantly as soon as the STED laser beam is blocked.

As a first application, the optical cross sections of stimulated emission were measured on isolated JA 26 molecules embedded in a polymer matrix. The determined cross sections were found to span a wide range of values which was attributed to the random orientations of the molecules in the matrix. These entail an inhomogeneous STED efficiency due to the photoselection which STED is subject to just as is excitation. While it was impossible to determine the absolute cross sections of each molecule individually, a good estimate for the average value was inferred from the largest values measured. It would be desirable to measure the molecular orientations along with the cross-sectional values because this additional information would allow to asses the individual absolute cross sections and, consequently, the influence of the molecular nanoenvironment. While traditional methods to measure molecular orientations require a significant number of extra photons (which is incompatible with the cross section measurement), very recently *Hohlbein* and *Hübner* suggested a new scheme to detect molecular orientations [126] which is based on the idea that in a high NA configuration, the z polarized emission components will be found mainly in the peripheral annular ring of the collimated flu-

orescence beam. By separately detecting the peripheral and the central contributions of fluorescence, the molecular transition dipole's can be obtained on-the-fly, a concept which would well integrate into the presented setup. Combined with a fluorescence excitation measurement with known detection efficiency, the orientational information would in turn enable the calculation of individual fluorescence quantum yields and also non-radiative decay rates. Altogether, the presented method of measuring the absolute cross sections may well constitute a first step towards the global analysis of fluorescent compounds on a single molecule level.

The results presented in the chapter on fluorescence fluctuation spectroscopy have shown that the effective detection volume can indeed be reduced using the STED technique. However, a background contribution which has not yet been successfully suppressed annuls the benefit of a reduced focal volume on the autocorrelation amplitude. While the artifacts introduced by this background can be corrected for by using a complementary analysis of the photon counting histogram, the initial goal to perform FCS at micromolar concentrations has not yet been fully achieved. Future efforts on this topic will mainly have to concentrate on the background issue which may be addressed by developing advanced phase retardation filters which circumvent the shortcomings of the presently used circular filter, i.e. the mismatch between the excitation and the STED focal intensity distributions. The use of adaptive optical elements may help to find the optimal shape of the wavefront. Besides this primary challenge, further optimizations are required to render STED-FCS a turn-key technique. These particularly concern the currently low count rate per molecule which should be improvable by optimization of the experimental setup, in particular by replacing the optical filters with filters particularly optimized for the respective dye. Even the complete removal of any bandpass filters may be feasible as long as the detector can be protected from damaging amounts of scattered light. By recording the raw photon count traces, postprocessing techniques such as time gating [21, 127] or time-resolved FCS [128] may be applied to remove background contributions due to scattering. The recent development of a fast algorithm to compute the autocorrelation function [129] further facilitates such approaches. In addition, recent and future extensions of the photon counting histogram analysis techniques [119] [2D-FIDA, fluorescence intensity multiple distribution analysis (FIMDA), fluorescence intensity and lifetime distribution analysis (FILDA)] may eventually allow a single global analysis of the data.

The field of photonics has recently experienced remarkable advances after the introduction of nanostructured materials with extraordinary optical properties, referred to as the photonic crystals. In the form of photonic crystal fibers [130] they are already commercially available and allow e.g. the propagation of ultrashort laser pulses devoid of dispersion. A second application which is becoming increasingly important is the so-called supercontinuum generation [131, 132]. This technique exploits the wealth of non-

linear optical effects which occur upon focusing femtosecond near-infrared laser pulses into a suitable photonic crystal fiber. As a result, a quasi-homogenous spectrum of new wavelengths is generated which can span the entire visible range. These supercontinuum sources are starting to enter the field of microscopy [133] where they are used as universal light sources. Furthermore, they have set off to replace more complex, costly and bulky laser light sources (like e.g. OPOs) in spectroscopic applications as well. The field of STED imaging and fluorescence spectrosopy in the bulk and on single molecules is expected to benefit from these developments particularly because such supercontinuum light sources will render the experiments more flexible, instrumentally less complicated and, last but not least, less costly.

References

[1] M. J. Perrin. La Fluorescence. *Ann. de Phys.*, 9:133–159, 1918.

[2] T. Hirschfeld. Optical microscopic observation of single small molecules. *Appl. Opt.*, 15(12):2965–2966, 1976.

[3] W. E. Moerner and L. Kador. Optical Detection and Spectroscopy of Single Molecules in a Solid. *Phys. Rev. Lett.*, 62(21):2535–2538, 1989.

[4] E. B. Shera, N. K. Seitzinger, L. M. Davis, R. A. Keller, and S. A. Soper. Detection of single fluorescent molecules. *Chem. Phys. Lett.*, 174(6):553–557, 1990.

[5] M. Sauer, B. Angerer, W. Ankenbauer, Z. Földes-Papp, F. Göbel, K.-T. Han, R. Rigler, A. Schulz, J. Wolfrum, and C. Zander. Single molecule DNA sequencing in submicrometer channels: state of the art and future prospects. *J. Biotechnol.*, 86:181–201, 2001.

[6] J. H. Werner, H. Cai, J. H. Jett, L. Reha-Krantz, R. A. Keller, and P. M. Goodwin. Progress towards single-molecule DNA sequencing: a one color demonstration. *J. Biotechnol.*, 102:1–14, 2003.

[7] T. Funatsu, Y. Harada, M. Tokunaga, K. Saito, and T. Yanagida. Imaging of single fluorescent molecules and individual ATP turnovers by single myosin molecules in aqueous solution. *Nature*, 374:555–559, 1995.

[8] H. Noji, R. Yasuda, M. Yoshida, and K. Kinosita. Direct observation of the rotation of F1-ATPase. *Nature*, 386:299–302, 1997.

[9] E. L. Elson and D. Magde. Fluorescence Correlation Spectroscopy. I. Conceptual Basis and Theory. *Biopolymers*, 13:1–27, 1974.

[10] R. Rigler and J. Widengren. Ultrasensitive detection of single molecules by fluorescence correlation spectroscopy. *BioScience*, 40:180–183, 1990.

[11] N. L. Thompson. Fluorescence Correlation Spectroscopy. In J. R. Lakowicz, editor, *Topics in Fluorescence Spectroscopy*, volume 1, pages 337–378. Plenum Press, New York/ London, 1991.

[12] O. Krichevsky and G. Bonnet. Fluorescence correlation spectroscopy: the technique and its applications. *Rep. Prog. Phys.*, 65:251–297, 2002.

[13] P. Kask, K. Palo, D. Ullmann, and K. Gall. Fluorescence-intensity distribution analysis and its application in biomolecular detection technology. *Proc. Natl. Acad. Sci. USA*, 96(24):13756–13761, 1999.

[14] Y. Chen, J. D. Müller, P. T. C. So, and E. Gratton. The Photon Counting Histogram in Fluorescence Fluctuation Spectroscopy. *Biophys. J.*, 77:553–567, 1999.

[15] M. Eigen and R. Rigler. Sorting single molecules: Applications to diagnostics and evolutionary biotechnolgy. *Proc. Natl. Acad. Sci. USA*, 91:5740–5747, 1994.

[16] R. Rigler. Fluorescence correlations, single-molecule detection and large number screening. Applications in biotechnology. *J. Biotechnol.*, 41:177–186, 1995.

[17] M. Auer, K. J. Moore, F. J. Meyer-Almes, R. Guenther, A. J. Pope, and K. A. Stoeckli. Fluorescence correlation spectroscopy: lead discovery by miniaturized HTS. *Drug Discov. Today*, 3(10):457–465, 1998.

[18] C. Eggeling, L. Brand, D. Ullmann, and S. Jäger. Highly sensitive fluorescence detection technology currently available for HTS. *Drug Discov. Today*, 8(14):632–641, 2003.

[19] S. Jäger, L. Brand, and C. Eggeling. New Fluorescence Techniques for High-Throughput Drug Discovery. *Curr. Pharm. Biotechnol.*, 4(6):463–476, 2003.

[20] H. Bach, A. Renn, and U. P. Wild. Spectral imaging of single molecules. *Single Mol.*, 1(1):73–77, 2000.

[21] C. Eggeling, S. Berger, L. Brand, J. R. Fries, J. Schaffer, A. Volkmer, and C. A. M. Seidel. Data registration and selective single-molecule analysis using multi-parameter fluorescence detection. *J. Biotechnol.*, 86:163–180, 2001.

[22] M. Prummer, B. Sick, A. Renn, and U. P. Wild. Multiparameter Microscopy and Spectroscopy for Single-Molecule Analytics. *Anal. Chem.*, 76:1633–1640, 2004.

[23] A. M. van Oijen, M. Ketelaars, J. Köhler, T. J. Aartsma, and J. Schmidt. Spectroscopy of Single Light-Harvesting Complexes from Purple Photosynthetic Bacteria at 1.2K. *J. Phys. Chem. B*, 102(47):9363–9366, 1998.

[24] P. Tinnefeld, K. D. Weston, T. Vosch, M. Cotlet, T. Weil, J. Hofkens, K. Müllen, F. C. De Schryver, and M. Sauer. Antibunching in the Emission of a Single Tetrachromophoric Dendritic System. *J. Am. Chem. Soc.*, 124:14310–14311, 2002.

[25] G. J. Schütz, V. P. Pastushenko, H. J. Gruber, H.-G. Knaus, B. Pragl, and H. Schindler. 3D Imaging of Individual Ion Channels in Live Cells at 40 nm Resolution. *Single Mol.*, 1(1):25–31, 2000.

[26] J.-P. Knemeyer, D.-P. Herten, and M. Sauer. Detection and Identification of Single Molecules in Living Cells Using Spectrally Resolved Fluorescence Lifetime Imaging Microscopy. *Anal. Chem.*, 75:2147–2153, 2003.

[27] S. Nie and S. R. Emory. Probing Single Molecules and Single Nanoparticles by Surface-Enhanced Raman Scattering. *Science*, 275:1102–1106, 1997.

[28] C. Brunel, B. Lounis, P. Tamarat, and M. Orrit. Triggered Source of Single Photons based on Controlled Single Molecule Fluorescence. *Phys. Rev. Lett.*, 83(14):2722–2725, 1999.

[29] V. Westphal, L. Kastrup, and S. W. Hell. Lateral resolution of 28 nm (l/25) in far-field fluorescence microscopy. *Appl. Phys. B*, 77:377–380, 2003.

[30] M. Heilemann, D. P. Herten, R. Heintzmann, C. Cremer, C. Müller, P. Tinnefeld, K. D. Weston, J. Wolfrum, and M. Sauer. High-Resolution Colocalization of Single Dye Molecules by Fluorescence Lifetime Imaging Microscopy. *Anal. Chem.*, 74:3511–3517, 2002.

[31] J. Köhler, J. A. J. M. Disselhorst, M. C. J. M. Donckers, E. J. J. Groenen, J. Schmidt, and W. E. Moerner. Magnetic resonance of a single molecular spin. *Nature*, 363:242–243, 1993.

[32] J. Wrachtrup, C. von Borczyskowski, J. Bernard, M. Orrit, and R. Brown. Optical detection of magnetic resonance in a single molecule. *Nature*, 363:244–245, 1993.

[33] T. Basché, W. E. Moerner, M. Orrit, and U. P. e. Wild. *Single-Molecule Optical Detection, Imaging and Spectroscopy*. Wiley-VCH, Weinheim, 1997.

[34] C. Zander, J. Enderlein, and R. A. Keller (eds.). *Single-Molecule Detection in Solution*. Wiley-VCH, Berlin, Germany, 1st edition, 2002.

[35] B. Valeur. *Molecular Fluorescence. Principles and Applications*. Wiley-VCH, Weinheim, 1st edition, 2001.

[36] B. Valeur and J.-C. Brochon (eds.). *New Trends in Fluorescence Spectroscopy. Applications to Chemical and Life Sciences*, volume 1 of *Springer Series on Fluorescence. Methods and Applications*. Springer -Verlag, Berlin, Heidelberg, New York, Barcelona, Hong Kong, London, Milan, Paris, Tokyo, 2001.

[37] M. Orrit. Single-molecule spectroscopy: The road ahead. *J. Chem. Phys.*, 117(24):10938–10946, 2002.

[38] S. Nie and R. N. Zare. Optical Detection of Single Molecules. *Annu. Rev. Biomol. Struct.*, 26:567–596, 1997.

[39] W. P. Ambrose, P. M. Goodwin, J. H. Jett, A. van Orden, J. H. Werner, and R. A. Keller. Single Molecule Fluorescence Spectroscopy at Ambient Temperature. *Chem. Rev.*, 99:2929–2956, 1999.

[40] S. Weiss. Fluorescence Spectroscopy of Single Biomolecules. *Science*, 283:1676–1683, 1999.

[41] P. Tamarat, A. Maali, B. Lounis, and M. Orrit. Ten Years of Single-Molecule Spectroscopy. *J. Phys. Chem. A*, 104(1):1–16, 2000.

[42] A. Einstein. Zur Quantentheorie der Strahlung. *Physik. Zeitschr.*, 18:121–128, 1917.

[43] H. Haken and H. C. Wolf. *Atom- und Quantenphysik*. Springer-Lehrbuch. Springer-Verlag, Berlin, Heidelberg, 7th edition, 2003.

[44] J. B. Birks. *Photophysics of Aromatic Molecules*. Wiley Monographs in Chemical Physics. Wiley-Interscience, London New York Sydney Toronto, 1970.

[45] T. Elsaesser and W. Kaiser. Vibrational and Vibronic Relaxation of Large Polyatomic Molecules in Liquids. *Annu. Rev. Phys. Chem.*, 42:83–107, 1991.

[46] J.-Y. Liu, W.-H. Fan, K.-L. Han, W.-Q. Deng, D.-L. Xu, and N.-Q. Lou. Ultrafast Vibrational and Thermal Relaxation of Dye Molecules in Solution. *J. Phys. Chem. A*, 107:10857–10861, 2003.

[47] J. R. Lakowicz. *Principles of Fluorescence Spectroscopy*. Kluwer Academic Publishers, 2 edition, 1999.

[48] M. Kasha. Characterization of electronic transitions in complex molecules. *Disc. Faraday Soc.*, 9:14–19, 1950.

[49] R. Marsh, D. Armoogum, and A. Bain. Stimulated emission depletion of two-photon excited states. *Chem. Phys. Lett.*, 366:398–405, 2002.

[50] T. Basché, S. Kummer, and C. Bräuchle. Direct spectroscopic observation of quantum jumps of a single molecule. *Nature*, 373:132–134, 1995.

[51] W. E. Moerner. Those Blinking Molecules. *Science*, 277(5329):1059–1060, 1997.

[52] T. Basché. Fluorescence intensity fluctuations of single atoms, molecules and nanoparticles. *J. Lumin.*, 76-77:263–269, 1998.

[53] R. M. Dickson, A. B. Cubitt, R. Y. Tsien, and W. E. Moerner. On/off blinking and switching behavior of single molecules of green fluorescent protein. *Nature*, 388:355–358, 1997.

[54] J. Widengren, Ü. Mets, and R. Rigler. Fluorescence Correlation Spectroscopy of Triplet States in Solution: A Theoretical and Experimental Study. *J. Phys. Chem.*, 99:13368–13379, 1995.

[55] J. Bernard, L. Fleury, H. Talon, and M. Orrit. Photon bunching in the fluorescence from single molecules: A probe for intersystem crossing. *J. Chem. Phys.*, 98(2):850–859, 1993.

[56] D. S. English, E. J. Harbron, and P. F. Barbara. Probing Photoinduced Intersystem Crossing by Two-Color, Double Resonance Single Molecule Spectroscopy. *J. Phys. Chem. A*, 104(40):9057–9061, 2000.

[57] R. Zondervan, F. Kulzer, S. B. Orlinskii, and M. Orrit. Photoblinking of Rhodamine 6G in Poly(vinyl alcohol): Radical Dark State Formed through the Triplet. *J. Phys. Chem. A*, 107:6770–6776, 2003.

[58] J. Widengren and P. Schwille. Characterization of Photoinduced Isomerization and Back-Isomerization of the Cyanine Dye Cy5 by Fluorescence Correlation Spectroscopy. *J. Phys. Chem. A*, 104:6416–6428, 2000.

[59] T. Christ, F. Kulzer, P. Bordat, and T. Basché. Watching the Photo-Oxidation of a Single Aromatic Hydrocarbon Molecule. *Angew. Chem. Int. Ed.*, 40(22):4192–4195, 2001.

[60] A. J. Meixner and M. A. Weber. Single molecule spectral dynamics at room temperature. *J. Lumin.*, 86:181–187, 2000.

[61] A.-M. Boiron, P. Tamarat, B. Lounis, R. Brown, and M. Orrit. Are the spectral trails of single molecules consistent with the standard two-level system model of glasses at low temperatures? *Chem. Phys.*, 247:119–132, 1999.

[62] M. Orrit. Photon Statistics in Single-Molecule Experiments. *Single Mol.*, 3(5-6):255–265, 2002.

[63] P. Kask, P. Piksarv, and Ü. Mets. Fluorescence correlation spectroscopy in the nanosecond time range: Photon antibunching in dye fluorescence. *Eur. Biophys. J.*, 12:163–166, 1985.

[64] T. Basché, W. E. Moerner, M. Orrit, and H. Talon. Photon Antibunching in the Fluorescence of a Single Molecule Trapped in a Solid. *Phys. Rev. Lett.*, 69(10):1516–1519, 1992.

[65] L. Fleury, J.-M. Segura, G. Zumofen, B. Hecht, and U. P. Wild. Nonclassical Photon Statistics in Single-Molecule Fluorescence at Room Temperature. *Phys. Rev. Lett.*, 84(6):1148–1151, 2000.

[66] C. Eggeling, J. Widengren, R. Rigler, and C. A. M. Seidel. Photostability of Fluorescent Dyes for Single-Molecule Spectroscopy: Mechanisms and Experimental Methods for Estimating Photobleaching in Aqueous Solution. In W. Rettig, B. Strehmel, S. Schrader, and H. Seifert, editors, *Applied Fluorescence in Chemistry, Biology and Medicine*, pages 193–240. Springer-Verlag, Berlin, Heidelberg, New York, 1999.

[67] R. Zondervan, F. Kulzer, M. A. Kol'chenko, and M. Orrit. Photobleaching of Rhodamine 6G in Poly(vinyl alcohol) at the Ensemble and Single-Molecule Levels. *J. Phys. Chem. A*, 108:1657–1665, 2004.

[68] C. Kittrell, E. Abramson, J. L. Kinsey, S. A. McDonald, D. E. Reisner, R. W. Field, and D. H. Katayama. Selective vibrational excitation by stimulated emission pumping. *J. Chem. Phys.*, 75(5):2056–2059, 1981.

[69] M. Schrader, F. Meinecke, K. Bahlmann, M. Kroug, C. Cremer, E. Soini, and S. W. Hell. Monitoring the excited state of a fluorophore in a microscope by stimulated emission. *Bioimaging*, 3:147–153, 1995.

[70] S. W. Hell, M. Schrader, K. Bahlmann, F. Meinecke, J. R. Lakowicz, and I. Gryczynski. Stimulated Emission on a Microscopic Scale: Light Quenching of Pyridinium 2 using a Ti:Sapphire laser. *J. Microsc.*, 180:RP1–RP2, 1995.

[71] Q. Zhong, Z. Wang, Y. Sun, Q. Zhu, and F. Kong. Vibrational relaxation of dye molecules in solution studied by femtosecond time-resolved stimulated emission pumping fluorescence depletion. *Chem. Phys. Lett.*, 248:277–282, 1996.

[72] S. W. Hell and J. Wichmann. Breaking the diffraction resolution limit by stimulated emission: stimulated emission-depletion fluorescence microscopy. *Opt. Lett.*, 19(11):780–782, 1994.

[73] S. W. Hell. Increasing the resolution of far-field fluorescence light microscopy by point-spread-function engineering. In J. Lakowicz, editor, *Topics in Fluorescence Spectroscopy*, volume 5, pages 361–422. Plenum Press, New York, 1997.

[74] T. A. Klar. *Progress in Stimulated Emission Depletion Microscopy*. PhD thesis, Rupertus Carola University of Heidelberg, 2001.

[75] J.-Y. Liu, W.-H. Fan, K.-L. Han, D.-L. Xu, and N.-Q. Lou. Ultrafast Dynamics of Dye Molecules in Solution as a Function of Temperature. *J. Phys. Chem. A*, 107:1914–1917, 2003.

[76] M. Dyba and S. W. Hell. Focal Spots of Size l/23 Open Up Far-Field Fluorescence Microscopy at 33 nm Axial Resolution. *Phys. Rev. Lett.*, 16(88):163901, 2002.

[77] T. Wilson (ed.). *Confocal Microscopy*. Academic Press Ltd., London, 1990.

[78] J. B. Pawley (ed.). *Handbook of Biological Confocal Microscopy*. Plenum Press, New York, London, 2nd edition, 1989.

[79] T. A. Klar, S. Jakobs, M. Dyba, A. Egner, and S. W. Hell. Fluorescence microscopy with diffraction resolution barrier broken by stimulated emission. *Proc. Natl. Acad. Sci. USA*, 97:8206–8210, 2000.

[80] E. Abbe. Beiträge zur Theorie des Mikroskops und der mikroskopischen Wahrnehmung. *Arch. f. Mikroskop. Anat.*, 9:413–420, 1873.

[81] M. Born and E. Wolf. *Principles of Optics*. Cambridge University Press, Cambridge, New York, Melbourne, Madrid, Cape Town, 7th edition, 2002.

[82] M. Gu. *Advanced Optical Imaging Theory*, volume 75 of *Springer Series in Optical Sciences*. Springer-Verlag, Berlin, Heidelberg, 1999.

[83] B. Richards and E. Wolf. Electromagnetic diffraction in optical systems II. Structure of the image in an aplanatic system. *Proc. R. Soc. Lond. A*, 253:358–379, 1959.

[84] U. Brackmann. *Lambdachrome Laser Dyes*. Lambda Physik AG, Göttingen, 3rd edition edition, 2000.

[85] P. Tinnefeld, C. Müller, and M. Sauer. Time-varying photon probability distribution of individual molecules at room temperature. *Chem. Phys. Lett.*, 345:252–258, 2001.

[86] T. A. Klar, E. Engel, and S. W. Hell. Breaking Abbe's diffraction resolution limit in fluorescence microscopy with stimulated emission depletion beams of various shapes. *Phys. Rev. E*, 64:066613, 1–9, 2001.

[87] V. Westphal, C. M. Blanca, L. Kastrup, and S. W. Hell. Laser-diode stimulated emission depletion microscopy. *Appl. Phys. Lett.*, 82(18):3125–3127, 2003.

[88] M. Dierksen and S. Grimme. Density functional calculations of the vibronic structure of electronic absorption spectra. *J. Chem. Phys.*, 120(8):3544–3554, 2004.

[89] D. McCumber. Einstein Relations Connecting Broadband Emission and Absorption Spectra. *Phys. Rev.*, 136(4A):A954–A957, 1964.

[90] S. J. Strickler and R. A. Berg. Relationship between Absorption Intensity and Fluorescence Lifetime of Molecules. *J. Chem. Phys.*, 37(4):814–822, 1962.

[91] O. Peterson, J. Webb, and W. McColgin. Organic Dye Laser Threshold. *J. Appl. Phys.*, 42(5):1917–1928, 1971.

[92] W. Holzer, H. Gratz, T. Schmitt, A. Penzkofer, A. Costela, I. García-Moreno, R. Sastre, and F. J. Duarte. Photo-physical characterization of rhodamine 6G in a 2-hydroxyethyl-methacrylate methyl-methacrylate copolymer. *Chem. Phys.*, 256:125–136, 2000.

[93] B. F. Aull and H. P. Jensson. Vibronic Interactions in Nd:YAG Resulting in Nonreciprocity of Absorption and Stimulated Emission Cross Sections. *IEEE J. Quant. Electron.*, QE-18(5):925–930, 1982.

[94] S. A. Payne, L. L. Chase, H. W. Newkirk, L. K. Smith, and W. F. Krupke. LiCaAlF6:Cr3+: A Promising New Solid-State Laser Material. *IEEE J. Quant. Electron.*, 24(11):2243–2252, 1988.

[95] E. P. Maldonado and N. D. Vieira Junior. A simple method to determine the effective emission cross-section of laser media. *Opt. Commun.*, 117:102–106, 1995.

[96] S. A. Payne, J. A. Caird, L. L. Chase, L. K. Smith, N. D. Nielsen, and W. F. Krupke. Spectroscopy and gain measurements of Nd3+ in SrF2 and other fluorite-structure hosts. *J. Opt. Soc. Am. B*, 8(4):726–740, 1991.

[97] A. Penzkofer, W. Holzer, and S.-H. Gong. Effective stimulated emission cross-sections determined by transient fluorescence amplification in a Fabry-Pérot resonator. *Opt. Quant. Electron.*, 29:611–626, 1997.

[98] A. Sennaroglu. Determination of the stimulated-emission cross section in an end-pumped solid state laser from laser-induced pump saturation data. *Opt. Lett.*, 26(8):500–502, 2001.

[99] W. H. Press, B. P. Flannery, S. A. Teukolsky, and W. T. Vetterling. *Numerical Recipes in C*. Cambridge University Press, Cambridge, 2nd ed. edition, 1993.

[100] B. Sick, B. Hecht, and L. Novotny. Orientational Imaging of Single Molecules by Annular Illumination. *Phys. Rev. Lett.*, 85(21):4482–4485, 2000.

[101] M. Böhmer and J. Enderlein. Orientation imaging of single molecules by wide-field epifluorescence microscopy. *J. Opt. Soc. Am. B*, 20(3):554–559, 2003.

[102] J. T. Fourkas. Rapid determination of the three-dimensional orientation of single molecules. *Opt. Lett.*, 26(4):211–213, 2001.

[103] D. Madge, E. L. Elson, and W. W. Webb. Thermodynamic Fluctuations in a Reacting System - Measurement by Fluorescence Correlation Spectroscopy. *Phys. Rev. Lett.*, 29(11):705–708, 1972.

[104] D. Magde and E. L. Elson. Fluorescence Correlation Spectroscopy. II. An Experimental Realization. *Biopolymers*, 13:29–61, 1974.

[105] J. Widengren and R. Rigler. Review - Fluorescence Correlation Spectroscopy as a Tool to Investigate Chemical Reactions in Solutions and on Cell Surfaces. *Cell. Mol. Biol.*, 44(5):857–879, 1998.

[106] U. Meseth, T. Wohland, R. Rigler, and H. Vogel. Resolution of Fluorescence Correlation Measurements. *Biophys. J.*, 76:1619–1631, 1999.

[107] P. Schwille, F. J. Meyer-Almes, and R. Rigler. Dual-color fluorescence cross-correlation spectroscopy for multicomponent diffusional analysis in solution. *Biophys. J.*, 72(4):1878–1886, 1997.

[108] A. G. Palmer and N. L. Thompson. Molecular aggregation characterized by high order autocorrelation in fluorescence correlation spectroscopy. *Biophys. J.*, 52(2):257–270, 1987.

[109] A. G. Palmer and N. L. Thompson. High-order fluorescence fluctuation analysis of model protein clusters. *Proc. Natl. Acad. Sci. USA*, 86:6148–6152, 1989.

[110] H. Qian and E. L. Elson. On the analysis of high order moments of fluorescence fluctuations. *Biophys. J.*, 57:375–380, 1990.

[111] T. A. Laurence and S. Weiss. How to Detect Weak Pairs. *Science*, 299:667–668, 2003.

[112] M. J. Levene, J. Korlach, S. W. Turner, M. Foquet, H. G. Craighead, and W. W. Webb. Zero-Mode Waveguides for Single-Molecule Analysis at High Concentrations. *Science*, 299:682–686, 2003.

[113] A. M. Lieto, R. C. Cush, and N. L. Thompson. Ligand-Receptor Kinetics Measured by Total Internal Reflection with Fluorescence Correlation Spectroscopy. *Biophys. J.*, 85:3294–3302, 2003.

[114] M. Foquet, J. Korlach, W. R. Zipfel, W. W. Webb, and H. G. Craighead. Focal Volume Confinement by Submicrometer-Sized Fluidic Channels. *Anal. Chem.*, 76:1618–1626, 2004.

[115] R. Rigler and E. S. Elson. *Fluorescence Correlation Spectroscopy. Theory and Applications*, volume 65 of *Springer Series in Chemical Physics*. Springer-Verlag, Berlin, Heidelberg, 2001.

[116] M. Ehrenberg and R. Rigler. Rotational Brownian Motion and Fluorescence Intensity Fluctuations. *Chem. Phys.*, 4:390–401, 1974.

[117] S. Aragón and R. Pecora. Fluorescence correlation spectroscopy as a probe of molecular dynamics. *J. Chem. Phys.*, 64(4):1791–1803, 1976.

[118] D. E. Koppel. Statistical accuracy in fluorescence correlation spectroscopy. *Phys. Rev. A*, 10(6):1938–1945, 1974.

[119] P. Kask, C. Eggeling, K. Palo, Ü. Mets, M. Cole, and K. Gall. Fluorescence Intensity Distribution Analysis (FIDA) and related fluorescence fluctuation techniques: theory and practice. In R. Kraayenhof, A. J. W. G. Visser, and H. C. Gerritsen, editors, *Fluorescence Spectroscopy, Imaging and Probes: New Tools in Chemical, Physical and Life Sciences*, volume Vol. 2 of *Springer Series on Fluorescence*, pages 154–181. Springer-Verlag, Berlin, Heidelberg, New York, 2002.

[120] P. Kask and K. Palo. Introduction to the Theory of Fluorescence Intensity Distribution Analysis. In R. Rigler and E. S. Elson, editors, *Fluorescence Correlation Spectroscopy: Theory and Applications*, volume Vol. 65 of *Springer Series in Chemical Physics*, pages 396–409. Springer-Verlag, Berlin, Heidelberg, New York, 2001.

[121] D. N. Whiteman, G. E. Walrafen, W.-H. Yang, and S. H. Melfi. Measurement of an isosbestic point in the Raman spectrum of liquid water by use of a backscattering geometry. *Appl. Opt.*, 38(12):2614–2615, 1999.

[122] A. Ashkin. Acceleration and Trapping of Particles by Radiation Pressure. *Phys. Rev. Lett.*, 24(4):156–159, 1970.

[123] A. Ashkin and J. M. Dziedzic. Optical trapping and manipulation of viruses and bacteria. *Science*, 235:1517, 1987.

[124] M. A. Osborne, S. Balasubramanian, W. S. Furey, and D. Klenerman. Optically Biased Diffusion of Single Molecules Studied by Confocal Fluorescence. *J. Phys. Chem. B*, 102:3160–3167, 1998.

[125] G. Chirico, C. Fumagalli, and G. Baldini. Trapped Brownian Motion in Single- and Two-Photon Excitation Fluorescence Correlation Experiments. *J. Phys. Chem. B*, 106:2508–2519, 2002.

[126] J. Hohlbein and C. G. Hübner. A Simple Scheme for Efficient 3D Orientation Determination of the Emission Dipoles of Single Molecules. *Personal Communication*, 2004.

[127] D. C. Lamb, A. Schenk, C. Röcker, C. Scalfi-Happ, and G. U. Nienhaus. Sensitivity Enhancement in Fluorescence Correlation Spectroscopy of Multiple Species Using Time-Gated Detection. *Biophys. J.*, 79:1129–1138, 2000.

[128] M. Böhmer, M. Wahl, H.-J. Rahn, R. Erdmann, and J. Enderlein. Time-resolved fluorescence correlation spectroscopy. *Chem. Phys. Lett.*, 353:439–445, 2002.

[129] M. Wahl, I. Gregor, M. Patting, and J. Enderlein. Fast calculation of fluorescence correlation data with asynchronous time-correlated single-photon counting. *Opt. Expr.*, 26(26):3583–3591, 2003.

[130] J. K. Ranka, R. S. Windeler, and A. J. Stentz. Visible continuum generation in air-silica microstructure optical fibers with anomalous dispersion at 800 nm. *Opt. Lett.*, 25(1):25–27, 2000.

[131] M. Bellini and T. W. Hänsch. Phase-locked white-light continuum pulses: toward a universal optical frequency-comb synthesizer. *Opt. Lett.*, 25(14):1049–1051, 2000.

[132] T. A. Birks, W. J. Wadsworth, and P. S. J. Russell. Supercontinuum generation in tapered fibers. *Opt. Lett.*, 25(19):1415–1417, 2000.

[133] G. McConnell. Confocal laser scanning fluorescence microscopy with a visible continuum source. *Opt. Expr.*, 12(13):2844–2850, 2004.

Acknowledgments

I would like to express my grateful appreciation and thanks to the many people who have contributed to the success of this dissertation.

Prof. Dr. Stefan W. Hell not only proposed the fascinating as well as challenging project of single-molecule STED spectroscopy but also provided a uniquely equipped workplace and an outstanding scientific environment. He has always been a helpful partner for stimulating discussions and has provided many fruitful ideas.

I would like to thank Prof. Dr. Jürgen Wolfrum at the Institute for Physical Chemistry at the University of Heidelberg for his interest in my work and for being a referee of my thesis.

The following present and former members of the NanoBiophotonics department and the whole Max Planck Institute of Biophysical Chemistry I would like to thank individually:

- Dr. Marcus Dyba and Dr. Thomas Klar for introducing me into the secrets of STED microscopy and for many valuable discussions,
- Dr. Andreas Schönle for providing the superb IMSPECTOR software environment which was heavily used for data acquisition and analysis,
- Dr. Volker Westphal for being a competent and enjoyable partner in the single-molecule resolution enhancement project,
- Dr. Hans Blom and Dr. Christian Eggeling for sharing their knowledge on FCS und FIDA and for their dedication in the STED-FCS project,
- Dieter-Jürgen Czudnochowski and his collegues in the mechanical workshop for their numerous contributions to my experimental setup,
- Wolfgang Sauermann and Wolfgang Kluge for manufacturing many(!) optical phase retardation masks,
- Jan Keller for supplying the PSF calculation software,

- Harald Meyer and Udo Gemm for help in numerous electronics issues,
- Dr. Marcus Dyba and Dr. Christian Eggeling for proof-reading the manuscript of this thesis and
- all my collegues who made the NanoBiophotonics department an enjoyable place to work at.

Prof. Dr. Karl-Heinz Drexhage and Dr. Jutta Arden-Jacob (University Siegen, Germany) kindly provided the dyes JA 26 and MR 121.

I would like to thank my parents for supporting me in any conceivable way. Without their outstanding and continuous support I would not have been able to enjoy the fabulous education I received.

My girlfriend Gwendolyn Werner has morally supported me throughout the past years. Without her, life besides science would have been much less exciting.

Last but not least, I want to thank the Volkswagen Foundation for financial support of this work.

Göttingen
August 2004 Lars Kastrup

Index